ALMA MATER STUDIORUM
UNIVERSITÀ DI BOLOGNA

DOTTORATO DI RICERCA IN

BIOLOGIA CELLULARE E MOLECOLARE

Ciclo 38

**Settore Concorsuale:** 05/I1 - GENETICA

**Settore Scientifico Disciplinare:** BIO/18 - GENETICA

# A CRISPR KNOCKOUT SCREEN HIGHLIGHTING DEPENDENCIES ON ACETATE METABOLISM FOR FATTY ACID BIOSYNTHESIS REVEALS A ROLE FOR SLC16A13 IN ACETATE IMPORT INTO CANCER CELLS

**Presentata da:** Fabrizio Bertolazzi

**Coordinatore Dottorato**

Anna Maria Porcelli

**Supervisore**

Giovanni Perini

**Co-supervisore**

Zachary Schug

Esame finale anno 2026

# ACKNOWLEDGEMENTS

They say it takes a village to raise a child, and indeed this thesis is the effort of many people, of whom I can only thank a fraction in the limited space that I have.

I firstly want to thank my friends and family back in Italy, who all still feel just around the corner despite us being separated by more than 4,000 miles. Thank you also to some Italians geographically closer to me as I am writing this, i.e. the members of our 2022 Bologna-Wistar cohort, and especially my roommate Kelvin, who always engaged me in thought provoking conversations just as I was trying not to fall asleep after leaving the lab in the dead of night.

Next, I want to thank all members past and present of the Schug Lab, alongside whom I have grown as a person and a scientist. If there is a person without which not only would this thesis not exist, but without whose guidance I could hardly ever expect to become a decent scientist, that person is Dr. Dzmitry Mukha. My gratitude also goes to Dr. Zachary T. Schug, for taking a chance on an unknown entity from Italy and for allowing me to pursue research directions with an uncommon degree of freedom.

Lastly, I need to thank the one person that really matters in this American adventure of mine, and that is my girlfriend Annabelle, who is the best achievement I have to show for these three years, this thesis included. Shout-out also to her princess of a cat Soup, whose frequent walks on the keyboard have substantially contributed to this document.

## ABSTRACT

The connection between cancer progression and deregulated cell metabolism is well established, as metabolites act as biomass sources and signaling modulators. Acetate is a major alternative nutrient source of acetyl-CoA and consequently influences oxidative respiration, lipid metabolism, and epigenetic regulation. While the role of acetate-metabolizing enzymes in cancer is an area of active study, a mechanistic and quantitative understanding of how acetate crosses the plasma membrane to contribute to compartmentalized cell metabolism is currently under-investigated and focused mostly on the activity the monocarboxylate transporters SLC16A1 and SLC16A3. To address this, we developed and applied an LC-MS metabolomics platform to quantitatively assess net metabolic consumption fluxes through the plasma membrane on a large panel of established cancer cell line models. We report on the relative contribution of each downstream functional pathway to acetate consumption, describing the larger quantitative role that fueling of the TCA cycle takes in comparison to biosynthesis and acetylation. By analyzing the landscape of transporter gene expression in cancer, we associate the poorly studied transporter SLC16A13 to acetate metabolism. Moreover, by designing and validating a CRISPR KO screen methodology that identifies genetic dependencies on acetate metabolism to sustain cell proliferation we directly link SLC16A13 to acetate import inside the cell. These findings open the opportunity of investigating the mechanism of acetate transport in multiple cancer types using the same methodology, while shedding light on a previously poorly characterized solute carrier transporter. A quantitative and mechanistic description of acetate transport is in general critical for increasing our understanding of cancer metabolism and human physiology, but targeting acetate transport in particular has translational potential for treating cancer in tissue-specific contexts, taking into account the role of acetate metabolism for immune responses. Elucidating the contribution of different transporters to acetate import in various tissue types is thus a major priority that we sought to address with this thesis.

TABLE OF CONTENTS

LIST OF TABLES

LIST OF FIGURES

# CHAPTER 1: INTRODUCTION

## *1.1 Cancer metabolism*

The field of cancer metabolism can be defined as the study of the reprogrammed cellular metabolic networks that support the key features distinguishing cancer cells from normal cells: aberrant proliferation, survival, migration, and deregulated cell fate control (1,2). It can be argued that cancer metabolism became a distinct area of research from physiological metabolism in 1923, when Otto Warburg first described how isolated slices of tumor tissue readily engage in the conversion of glucose into lactate, a process of aerobic glycolysis that has come to be associated with cancer cell metabolism and is referred to as the Warburg effect (3–5). This differs from the metabolic regulation of normal tissues, where availability of oxygen favors glucose oxidation and suppresses fermentation, a mechanism termed the Pasteur effect (6). While Warburg originally hypothesized that preferential aerobic glycolysis could be due to mitochondrial deficiencies in highly proliferative and thus hypermetabolic cancer cells (7), it has since become apparent that explaining the Warburg effects requires a nuanced description of cancer cell metabolism (8). Indeed, cancer cells have been shown to possess functionally active mitochondria (9,10), while at the same time some cancer types have been described as less metabolically active than once thought due to the downregulation of cell functions not related to proliferation (11). To date, several interpretations of the Warburg effect have been proposed: as an indirect way to maintain pentose phosphate pathway intermediate pools for biosynthetic needs (8), as a consequence of overflow metabolism creating a redox imbalance between cytosolic and mitochondrial compartments which requires $NAD^+$ regeneration through the reduction of pyruvate (12,13), as a regulated response for survival in heterogeneously hypoxic microenvironments (the Crabtree effect) (14–16), as a survival mechanism to circumvent apoptotic signaling (17–19), and as a strategy to evade immune responses by acidifying the tumor microenvironment (TME) (20). This research focus has uncovered a wealth of information on cell metabolism that finds application for cancer diagnostics, like in the use of $^{18}$F-fluorodeoxyglucose (FDG) positron emission tomography (PET) to identify solid tumors *in vivo* (21), but importantly also outside of the field of cancer itself, such as in understanding

the way lymphocyte T cells rewire their metabolism to proliferate and activate their effector functions in the course of an immune response (22–24).

### *The metabolic signatures of cancer metabolism: major nutrients and pathways*

Besides dysregulation of the glycolytic pathway, tumors show a variety of altered metabolic pathways. Cancer cells proliferating *in vitro* are found to consume glutamine far in excess of any other amino acid, to the point of depending on extracellular glutamine for survival (25–27). This has been rationalized by noting that, beyond being a nitrogen donor for amino acid and nucleotide synthesis (28), glutamine catabolism also contributes carbon units to the synthesis of aspartate and glutamate, and can replenish depleted TCA cycle intermediates by anaplerosis (29–31).

Another amino acid that cancer cells are metabolically dependent on is serine. Increased *de novo* biosynthesis of serine and increased expression of the serine synthesis enzyme phosphoglycerate dehydrogenase (PHGDH) have been observed in cancer (32–37). While the multiple roles of increased serine dependency are still a matter of investigation, it is known that serine supports proliferation by acting as the primary carbon donor to the tetrahydrofolate (THF) cycle involved in nucleotide biosynthesis, and that is involved in the production of NADPH to support anabolic reactions (38–41).

As a striking indication of their dysregulated metabolism, cancer cells are able to engage in *de novo* fatty acid synthesis even if they do not originate from hepatocytes (42,43). Fatty acid synthesis is a multistep process that primarily occurs in the cytosol of cells. Firstly, acetyl-CoA groups are converted to malonyl-CoA via the enzyme acetyl-CoA carboxylase (ACC) after which the multidomain enzyme fatty acid synthase (FASN) assembles the sixteen-carbon fatty acid chain palmitate from malonyl-CoA. Although fatty acid synthesis occurs in the cytosol, cytosolic acetyl-CoA is primarily produced from glucose-derived citrate, which is exported from mitochondria and cleaved by the cytosolic enzyme ATP-citrate lyase (ACLY) to release acetyl-CoA and oxaloacetate (44). Cancer cells are also able to generate cytosolic acetyl-CoA from acetate in the same compartment, and some cancers are dependent on the expression of acetyl-CoA synthetase 2 (ACSS2), the cytosolic enzyme that allows this

reaction to occur, making it a potential therapeutic target (45–49). The topic of acetate metabolism will be expanded upon in a subsequent sub-chapter.

### *Therapeutic strategies to target cancer metabolism*

Beyond providing a purely descriptive way of understanding cancer metabolism as a collection of chemical pathways, two main goals have directed research efforts in the field: 1) to understand how metabolism impacts tumorigenesis and cancer progression, and 2) to target metabolism to therapeutically affect cancer outcomes. Both of these goals interface with the debate over whether cancer should be considered a genetic or metabolic disease (50). Indeed, while the concept of genes acting as drivers or suppressors of carcinogenesis is well established (51–53), advances in and widespread adoption of metabolomics analysis platforms in the last two decades (54) have allowed the characterization of "oncometabolites", which are defined as endogenous metabolites whose accumulation can initiate or sustain tumor growth and metastasis, often in a tissue-specific fashion (50,55). The first oncometabolite to be identified was 2-hydroxyglutarate (2-HG), which is accumulated in cancer cells as a consequence of the neomorphic activity caused by mutations in the isocitrate dehydrogenases IDH1 and IDH2, such that isocitrate in the TCA cycle is redirected from conversion into α-ketoglutarate (α-KG) to conversion into 2-HG (56,57). In turn, high cellular concentrations of 2-HG, which is structurally similar to α-KG, lead to DNA and histone hypermethylation due to 2-HG's function as a competitive inhibitor of histone demethylases. Eventually, widespread epigenetic reprogramming promotes malignant transformation (58–68). Following 2-HG, many other metabolites involved in glycolysis or the TCA cycle have been reclassified as oncometabolites (50,55), most notably fumarate and succinate as a result ofmutations found in fumarate hydratase (FH) and succinate dehydrogenase (SDH) respectively (69–72).

In the search for therapeutic ways to leverage the increasing knowledge of cancer metabolism, very effective early successes have been found difficult to replicate in recent decades (73). Historically, the most effective class of cancer therapies directed at metabolism have been the so-called antimetabolites, which are small molecules that

interfere with processes required for sustained cell proliferation by structurally mimicking metabolic substrates (44). The first class of antimetabolites to be introduced were antifolates, with aminopterin described in 1948 by Sydney Farber, eventually followed by the currently employed drugs methotrexate and pemetrexed. By acting as folate analogs in one-carbon metabolism, antifolates inhibit *de novo* nucleotide synthesis (74,75). Other therapeutically successful antimetabolites include 6-mercaptopurine (6-MP) and 6-thioguanine (6-TG) which inhibit the first enzyme in *de novo* purine biosynthesis (76), the pyrimidine analogue 5-fluorouracil (5-FU) which limits the availability of thymidine nucleotides for DNA synthesis (77,78), and the nucleoside analogs gemcitabine and cytarabine which are incorporated into DNA and inhibit polymerase activity (79). What all these antimetabolites have in common is that they affect proliferation by targeting nucleotide metabolism. This complicates their use since many non-malignant cells proliferate more rapidly than cancer cells, shrinking the effective therapeutic window (80). Cancer cells present many other altered metabolic dependencies for proliferation that differ from those of normal cells (81–83), but therapeutically targeting them has proved difficult. For example, inhibiting aerobic glycolysis directly with the antimetabolite 2-deoxyglucose (2-DG), which like glucose is phosphorylated by hexokinase but unlike it cannot be metabolized further, is not a therapeutically viable strategy due to toxicity associated with hypoglycemia at the dose required to affect disease progression (84–88). In recent years, targeting the mutated forms of IDH1 and IDH2 with specific inhibitors (enasidenib and ivosidenib) has been met with more clinical success, but the effectiveness of these drugs is limited to certain cancer types, like leukemia, and not to other IDH-mutant types like gliomas (89–94). The dependence of cancer cells to glutamine has also been targeted, but inhibition of glutaminolysis with glutamine analogs has shown complete absence of therapeutic window, likely due to the non-specific nature of the treatment (95,96). Moreover, recent efforts to target the glutaminase enzymes have revealed that cancer cells can enact mechanisms of metabolic compensation to withstand such a treatment, requiring combination therapies to overcome this (97,98). Lastly, dietary intervention aimed at starving cancer cells of essential metabolites like amino acids has also been experimented

on, alone or in combination with more traditional chemical interventions, showing promise in the case of low asparagine and low glycine regimens (99–102). While this is not intended as an exhaustive list of all metabolic interventions that have been attempted in the field of cancer therapy, it shows how the need to find metabolically associated targets that are both effective in cancer and not systemically toxic remains a priority. Metabolite transporters have been suggested as a possible avenue for this (103).

### *1.2 Acetate metabolism in health and disease*

Acetate is a short chain fatty acid (SCFA) that is physiologically present at various concentrations in the human body, ranging from ~100 μM in plasma to over 100 mM in the lumen of the intestine (104,105). High concentrations of acetate in the digestive system are not a specific feature of humans, as measurements in both the intestine of mice and the rumen of ruminants have revealed concentrations comparable to that of the human intestine (106,107).

#### *Physiological sources of acetate*

Sources of acetate can be broadly categorized as 1) direct dietary supplementation, 2) general intracellular reactions, 3) specific liver metabolism, or 4) microbial intestinal metabolism. Dietary sources from which acetate can be directly acquired include dairy products, processed meats, bread, and ethanol (108). Acetate can be generated inside most cells by deacetylation of histones and other proteins or by the hydrolysis of acetylated metabolites, including acetyl-CoA. Liver metabolism can also generate acetate by deacetylation reactions and then release it into the circulation to be catabolized in other parts of the body (109–111). It has been reported that acetate can also be generated from glucose-derived pyruvate through either the activity of reactive oxygen species (ROS) or ketoacid dehydrogenases, though this process has so far been described as happening in a cell-type and treatment-specific fashion (112,113). The liver is additionally responsible for the release of circulating acetate after ethanol consumption, during which hepatocytes can come in contact with concentrations of acetate many times those in the blood (107). The majority of acetate in the body is generated through the breakdown of dietary fibers by the

intestinal microbiota, through either saccharolytic fermentation of pyruvate via acetyl-CoA or acetogenesis via the reductive Wood-Ljungdahl pathway (114–116). While some microbiota-associated bacterial species produce acetate (*Bacteroides spp.*, *Prevotella*, *Bifidobacterium*, *Escherichia coli*, *Akkermansia muciniphila*, *Lactobacillus brevis*), other consume it to sustain their proliferative needs (*Faecalibacterium duncaniae*, *Bacteroides fragilis*, *Firmicutes*, *Coprococcus*, *Lachnoclostridium*). As a consequence of this, dietary factors related to acetate can influence the composition of the intestinal microbiota, which has implications for inflammation response during pathogenic invasion (105,117,118) and obesity (119).

## Acetate catabolism in health and disease

As a cancer-associated metabolite, acetate was first studied by Sidney Weinhouse during the 1950s in the context of lipid metabolism and substrate availability in cancer (120–122). At the time, acetate was shown to be a substrate for respiration whose consumption is independent of increased availability of glucose.

Inside cells, acetate catabolism consists in the ATP-dependent ligation of one molecule of acetate and one of coenzyme A (CoA) to produce acetyl-CoA. This reaction is catalyzed independently by two acetyl-CoA synthetase (ACSS) enzymes, ACSS1 and ACSS2. Genetically, the two enzymes are both located on the same arm of chromosome 20, although they occupy different loci (123). At the protein level, ACSS1 and ACSS2 differ by their cellular localization, as ACSS1 is present in the mitochondrial matrix, while ACSS2 is found in the nucleus and cytosol (124). The acetyl-CoA resulting from acetate catabolism is a central metabolic intermediate involved in energy production by fueling carbon units to the TCA cycle, in biosynthetic pathways for *de novo* lipogenesis and the mevalonate pathway for the production of sterols, and in acetylation of metabolites (e.g. UDP N-acetylglucosamine) and proteins (125). There is ample evidence that characterizes acetate as an alternative nutrient source in many cancer types: breast cancer, hepatocellular carcinoma, melanoma, glioblastoma, renal cell carcinoma, non-small cell lung cancer, cervical squamous cell carcinoma, pancreatic cancer, ovarian cancer, and myeloma (45,49,108,124,126–135).

Additionally, acetate is recognized as playing a multifaceted role in the regulation of immune responses, where it can act, depending on the stage of the response, as an alternative nutrient and signaling molecule promoting T cell effector function (136,137), or later on as a regulator of glutaminolysis, cellular respiration and survival in memory T cells (138). Recently, it has also been shown that acetate is involved in metabolic symbiosis between hepatocellular carcinoma cells and tumor-associated macrophages, whereby cancer cells release lactate which then activates macrophages to produce and secrete acetate in the TME (139).

ACSS2, whose higher expression is associated with poorer prognosis in cancer, is regulated by sterol regulatory element-binding proteins (SREBP) and as such responds to environmental stressors like hypoxia and low nutrient availability, which are commonly found in solid tumors (49,140). ACSS2 has additional signaling roles due to its position upstream of nucleocytosolic acetylation, as it has been shown to stabilize interferon regulatory factor 4 (IRF4) in myeloma (135), and to likely be involved in the stabilization of Hypoxia-Inducible Factor 2α (HIF-2 α) in clear cell renal carcinoma (141). Outside of cancer, ACSS2 expression loss can impair long-term spatial memory in mice by changes in histone acetylation levels in the hippocampus (142), while its expression promotes systemic fat storage in mice (143) and is downregulated in exhausted T cells (144). Besides acetate, lactate and β-hydroxybutyrate have also recently been described as possible substrates of the reaction catalyzed by ACSS2, and in particular the resulting lactylation of histones has been found to play a role in promoting an immunosuppressive TME (145–148).

While previous research efforts have focused more on ACSS2, ACSS1 has also been a subject of investigation forits role as an acetyl-CoA-generating enzyme in the mitochondria. ACSS1 is known to be highly expressed in heart, spleen, lung, kidney, and testis (149). It shares around 50% sequence identity with ACSS2, with the main differences being located in motifs associated with cellular localization (123). In terms of disease, ACSS1 expression has been positively correlated with obesity (135), with increased incidence and poorer prognosis in hepatocellular carcinoma (150), and has been characterized as a viable therapeutic target for the treatment of acute myeloid leukemia (151). Additionally, deletion

of ACSS1 in murine astrocytes has been shown to be protective against loss of cognitive performance during sleep disruption cycles by keeping acetate levels higher, which then regulate glycolysis and the TCA cycle through binding with pyruvate carboxylase (152)

### *1.3 Solute Carrier Transporters*

#### *Types of transporter proteins: SLCs and other families*

The regulation of influx and efflux of solutes across biological membranes is essential to maintain cellular and organismal homeostasis, as it allows cells to control nutrient levels, direct chemical reactions, remove waste and regulate cell volume (153–155). The topic has been a subject of study at a molecular level for more than one hundred years, since Wilhelm Pfeffer provided the first evidence that osmosis does not explain all molecular movements across membranes and Ernest Overton systematically examined the permeability of hundreds of compounds and linked this to their chemical properties (156).

Transporter proteins are currently classified into four groups: 1) ATP-binding cassette (ABC) transporters, 2) ATPases, 3) ion channels, and 4) solute carrier proteins (SLC) (155,157,158). According to the Human Genome Organization (HUGO) Nomenclature Committee (HGNC), as of October 2025 there are 51 genes in 7 families belonging to ABC transporters, 149 genes in 4 families belonging to ATPases, 327 genes belonging to ion channels, and 474 genes in 77 families belonging to SLCs. ABC transporters and ATPases use the energy from ATP hydrolysis to export substrates from eukaryotic cells. The former are implicated in drug resistance to chemotherapy (159,160), while the latter can synthesize ATP using ion gradients (F-type ATPases), build an electrochemical gradient by consuming ATP (V-type ATPases), transport ions and lipids (P-type ATPases), and perform a variety of other cellular activities (AAA+ ATPases) (161–163). Ion channels allow ions to cross lipid membranes down their concentration gradient, in effect performing facilitated passive transport. As they don't undergo extensive conformational changes, they usually effect rapid transport of ions in order to maintain membrane potential and render signaling and excitation by electrochemical means possible (164,165).

SLCs are defined by being solute transporters that do not belong to the other three groups. By number of members, SLCs are the second-largest family of membrane proteins in the human genome after G protein-coupled receptors (GPCRs) (166). In terms of transport mechanism, SLCs do not use ATP directly, but can act either as passive facilitative transporters or secondary active transporters (167). Passive facilitative transport means that SLCs act as gatekeepers for compounds to move down their thermodynamically favorable gradient (157). On the other hand, secondary active transport means that the passage of two or more substrates is coupled, such that as one moves down its electrochemical gradient, it provides the free energy to transport the other (155). Such secondary active transporters can either be symporters, which transport their substrates in the same direction, or antiporters, in which the substrates cross the membrane in opposite directions (157). Most secondary active transporters are believed to use the 'alternating access' transport mechanism, whereby protein domains are arranged to have a ligand binding site available on only one side of the membrane at a time, changing conformations to transport their substrates by shifting to the other side of the membrane (168). Around 60% of SLCs are currently known to localize on the plasma membrane, with the remaining thought to function as transporters between different cellular organelles (155).

While other classification systems exist (such as the Transporter Classification Database or TCDB, and the Protein family or Pfam system (169)), the families into which SLCs are divided to obtain their name are defined by the HGNC and have been traditionally organized so that each protein within a family shares a minimum of ~25% sequence identity with at least another member of the same family (170,171). The naming system is used for both human genes and their orthologs in other species (169). The classification is constantly evolving, with new genes being added and old ones being reclassified into different families due to recent advances in the phylogenetic and structural analysis of the superfamily. Recent efforts suggest that the superfamily has a long evolutionary history and is thus highly heterogeneous (166,172), with approximately 180 independent evolutionary origins and a total of 24 structurally distinct transmembrane folds, the most common ones being the Major Facilitator Superfamily (MFS), the Leucine Transporter (LeuT), and the mitochondrial

carrier (MitC) folds. The MFS and LeuT folds include 138 and 72 SLCs respectively and are characterized by 12 transmembrane (TM) segments, while the MitC fold includes 53 SLCs all belonging to the SLC25 family and characterized by 6 TM segments (166,167). If instead of focusing on structure, SLCs are organized by phylogenesis, 4 main clusters (α, β, γ, and δ) emerge, though a number of SLC families don't fit into any of the four. The main clusters α and β, which at the time of the analysis in 2011 contained 13 and 9 SLC families respectively, are present in all species-specific lineages that were considered for phylogenetic analysis and are hypothesized to have been present in an early eukaryotic ancestor (166).

In a similar way to their phylogenetic and structural heterogeneity, SLCs transport a wide range of molecules, including sugars, amino acids, vitamins, nucleotides, metals, inorganic ions, organic anions, oligopeptides, and drugs. Substrate class specificity tends to be consistent within most families (171), although it should be noted that substrate promiscuousness is not uncommon (153). In terms of substrates, as of 2020 around 30% of SLCs were termed "orphan", i.e. with no known substrate (155). Indeed, a meta-analysis of SLCs literature from 2015 has found that the average number of publications per family member is half of what is observed for all gene families. Additionally, SLCs show the greatest publication asymmetry of all gene families, meaning that a few SLCs have been highly studied while for most very little is known (175). This has been ascribed to the existence of available research tools only for those SLCs that are already well-characterized, including expression cloning reagents and genetically modified cell lines. For this reason, calls to action aimed at increasing research interest in SLCs have recently resulted in the creation of the RESOLUTE Consortium, a public-private partnership that aims at creating tools for SLC research, de-orphanize transporter-substrate pairs and employ the resulting knowledge for therapeutic applications (176).

### *SLCs in health and disease*

SLCs have been found to be tissue-specific in function (155) and in some cases to act as both transporters and signaling receptors, as is the case for amino acid transporters (177). Due to their extensive roles in physiology, it is thus not surprising that about 190 SLCs have

been found mutated in inherited human diseases and that through genome-wide association studies (GWAS) SLC polymorphisms have been linked to complex diseases (178,179). For example, associations with type 2 diabetes have been made for SLC16A11 (180,181) and SLC16A13 (182). SLCs are also relevant for drug pharmacokinetics, often being the means by which small molecule therapeutics can enter cells (183). These include antimetabolites such as 5-FU and methotrexate (184).

SLCs are directly involved in cancer metabolism. For example, the SLC2 and SLC5 families of glucose-associated transporters are known to be upregulated in many cancer types (155). SLC7A11 and SLC3A2, which together form the xCT glutamate-cystine exchanger, have been shown to be critical for cancer survival through their role in redox balance maintenance and ferroptosis (185–187). Small molecular inhibitors of SLC1A5 (ASCT2), which transports glutamine and serine inside cancer cells, have been found to have antitumor efficacy both *in vitro* and *in vivo* (188–190)

A group of transporters of high relevance for central carbon metabolism in cancer is the SLC16 family. The family contains 14 members that are also known as monocarboxylate transporters (MCTs) (191). The SLC16 members are symporters of protons and substrates (192,193) and are known to belong to the MFS superfamily and the α cluster (172,174). SLC16A1, SLC16A8 and SLC16A3 (MCT1, MCT3, and MCT4 respectively) interact with the chaperone protein basigin (CD147) for proper translocation to the plasma membrane (194,195), while SLC16A7 (MCT2) interacts with a different chaperone, embigin (gp70), for the same purpose (196). This transporter-chaperone interaction has been structurally described for SLC16A1 as being reliant on a conserved motif located on the flexible N-terminus of the protein, and this is likely to be case for other transporters of the family as well (197). Transport substrates are known for SLC16A1 (lactate, pyruvate, ketone bodies), SLC16A2 (hormones T2, rT3, T3, T4), SLC16A3 (lactate, ketone bodies), SLC16A7 (lactate, pyruvate, ketone bodies), and SLC16A8 and 10 (aromatic amino acids, hormones T3 and T4), while the other members of the family are currently orphans (155,174). Of relevance for cancer survival and progression is the transport of lactate mediated by SLC16A1 and SLC16A3. Their expression in cancer is modulated via basigin expression, which itself is

often upregulated in cancer (198). Interestingly, overexpression of SLC16A1 and SLC16A3 is not concomitant in the same cell in the context of the tumor mass (155). This is because when considering the entirety of the TME, SLC16A1 and SLC16A4 act as lactate importer and exporter respectively (199). Well-perfused cells of the tumor have higher expression of SLC16A1, to import lactate and rapidly fuel oxidative phosphorylation. On the other hand, reprogrammed cancer-associated fibroblasts and poorly perfused cells in hypoxic environments rely on glycolysis to generate energy and thus express SLC16A3 to export lactate (200,201). This metabolic connection between tumor cells has been variably described as lactate shuttling, cancer symbiosis, or reverse Warburg effect (202). The mechanistic understanding of lactate transport by MCTs has made lactate transport an appealing target for therapeutic intervention, and indeed inhibitors for both lactate transporters are available (203,204), with clinical trials currently ongoing (205). Lastly, the recent discovery that MCT1 can be localized in both the plasma and mitochondrial membranes adds an additional layer of complexity to the transport of lactate (206) and to the mechanism of action of MCTs in general.

### *Recent discoveries in the field of SLCs*

Annotating transporter-substrate pairs for SLCs presents some challenges that render functional studies nontrivial. These include transporter substrate promiscuity, redundancy of multiple transporters for the same substrate, and dual subcellular localization of transporters (153). These challenges can be addressed with a variety of tools, which come with their advantages and drawbacks. Broad systems like genetic screens and GWAS allow the interrogation of many transporter-substrate pairs, while requiring rigorous and optimized experimental and analytical practices to maintain precision and physiological relevance. Biochemical assay with cell-free systems for the detection of substrate movement and the structural analysis of transporters offer high precision at the cost of potentially limited physiological relevance. Cell-based assays are a compromise between relevance and precision, but often require prior knowledge in order to focus on specific transporter-substrate pairs (153).

Nevertheless, the last few years have seen a marked acceleration in the investigation of previously uncharacterized transport mechanisms. Starting from the description of sideroflexins (SFXNs) in 2018 as mitochondrial serine transporters (207), genetic screens, cell assays and *in vivo* experiments have been successfully applied to identify CLCC1 as an hepatic facilitator of neutral lipid flux (208), SLC7A6 and SLC7A7 as importers of cationic amino acids (209), SLC38A3 as a high-affinity histidine transporter (209), SLC43A1 as a net exporter of large neutral amino acids (209), SLC45A4 as a polyamine transporter (210,211), SLC25A39 as a mitochondrial glutathione transporter (212), FLVCR1 and FLVCR2 as choline and ethanolamine transporters (213), SLC25A48 as a mitochondrial choline importer (214,215), SLC16A1 as a succinate exporter in the retina (216), SLC25A51 as a mitochondrial $NAD^+$ transporter (217), SLC33A1 as an exporter of oxidized glutathione in the endoplasmic reticulum (218), SLC6A6 as a mitochondrial taurine importer (219), and SLC25A45 as a mitochondrial importer of methylated amino acids (220,221). Such a list of recently de-orphanized transporters highlights the growing interest in SLC research as well as the many therapeutic opportunities that this increased focus brings.

### *Current literature on acetate transport*

Acetate transport has received comparatively less attention than other monocarboxylates like lactate and pyruvate, especially in cancer models (108,222). In terms of the broad mechanism of transport, passive diffusion does not play a quantitatively large role in the uptake of acetate inside cells (223). This is due to the fact that the plasma membrane is permeable to the non-ionic form of acetic acid, but not to the acetate anion. Given that both the pH in the lumen of the large intestine and in the extracellular matrix is higher than the pKa of acetate, which is 4.75, the acetate anion is the most prevalent form that cells come in contact with (224). Active acetate transport has been shown to be influenced by gradients across the plasma membrane of protons as well as sodium, bicarbonate and chloride ions (223,225). To date, no transporter proteins have been confidently associated with the antiport of bicarbonate and acetate, which is thought to functionally buffer the pH of the colonic lumen (224,226,227). Ectopic expression systems in *Xenopus laevis* oocytes have shown acetate to be a relevant saturable substrate with similar affinity for the active proton-

coupled monocarboxylate transporters MCT1 and MCT2, and with lower affinity for the sodium-coupled SMCT1, but non-saturable for MCT4 (228–233). It is important to note that SMCT1 is classified as a tumor suppressor gene, and accordingly is downregulated in most cancers, including many that consume acetate (234). Evidence in cancer cell lines has shown that exposure to acetate can specifically upregulate the expression of MCT1 in small panels of non-small cell lung cancer (NSCLC), clear cell renal carcinoma (ccRCC), and colorectal (CRC) cell lines, and in the case of the latter group to influence MCT4 expression as well (131,225,235). Likewise, inhibition of MCT1 has been shown to partially reduce acetate uptake in rat hepatocytes, a small subset of hepatocellular carcinoma (HCC) cell lines, and astrocytes (236–238). Additionally, it has been found that MCT4 expression is upregulated in hypoxia, a condition in which acetate utilization is also upregulated (239). On the other hand, experiments on the apical mucosa of the ruminal epithelium of sheep and on cultured human colonic epithelial cells have not shown MCT1 to be involved in acetate uptake in those models (223,240). To account for the fraction of acetate uptake independent of monocarboxylate transporters, the activity of anion exchangers and channels such as aquaporins and the Cystic Fibrosis Transmembrane Conductance Regulator (CFTR) has been implicated, in the latter case due to a small, but significant, level of acetate conductance for the channel in Calu-3 cells (223,225,241). Additionally, short chain fatty acids (SCFA) like acetate have been shown to act as competing substrates with glycine and proline for uptake by the proton-dependent amino acid transporters PAT1 and PAT2 in oocyte models only (242).

### *1.4 Gap in knowledge and aim of the project*

To date, no extensive investigation of acetate transport in cancer cells has been attempted. While cell-free or oocyte-based systems have indicated a role for the monocarboxylate transporter MCT1, reports are conflicting over the extent to which other transporters such as MCT2 and MCT4 are involved in acetate transport specifically, as many studies focus instead on propionate or butyrate and only infer conclusions on acetate as well. While a few cell models have been investigated for their ability to transport acetate, no systematic study has considered the potential for differential transporter gene expression due to differences in the

transporter makeup of the respective tissues of origin. This is likely the explanation as to why reports disagree on the extent to which the same transporters can influence acetate import in different cancer models. While in recent years research on metabolite transporters has been accelerated by the availability of CRISPR-based genomic screening platform, no study to date has combined metabolomics and genomics for the identification of acetate transporter proteins. This is mainly due to the fact that acetate is not present in standard culture medium formulations used for most genomic screens, and it is also not strictly required for the survival of cancer cells in standard culture conditions, where abundant availability of oxygen and metabolites is provided.

This project aims to improve our understanding of acetate transport in cancer cells in both a quantitative and qualitative manner. We employ an LC-MS metabolomics-based system to quantify acetate consumption in a panel of several cancer cell line models of different origin, and we break down the contribution that each metabolic pathway downstream of import plays to determine the extent of acetate consumption by cells. We then analyze the distribution of transporter gene expression in cancer cell lines and proceed to perform a CRISPR knockout screen based on acetate essentiality for proliferation, reporting that for both analyses the gene SLC16A13 encoding for the MCT13 transporter emerges as a likely previously uncharacterized acetate transporter protein.

# CHAPTER 2: MATERIALS AND METHODS

*Key resources*

| REAGENT or RESOURCE | SOURCE | IDENTIFIER |
|---|---|---|
| **Chemicals** | | |
| Methanol, Optima™ LC/MS grade | Fisher Scientific | A456 |
| Acetonitrile, Optima™ LC/MS grade | Fisher Scientific | A955 |
| Water, Optima™ LC/MS grade | Fisher Scientific | W6 |
| Isopropanol, Optima™ LC/MS Grade | Fisher Scientific | A461 |
| n-hexane, Optima™ for HPLC and GC/MS | Fisher Scientific | H306 |
| Ammonium hydroxide | Honeywell | 44273 |
| Ammonium formate | MilliporeSigma | 70221 |
| Ammonium bicarbonate | MilliporeSigma | 40867 |
| Phosphate buffered saline | MilliporeSigma | P3813 |
| Sodium chloride (ACS) | Fisher Scientific | S271-3 |
| Potassium chloride (ACS) | MilliporeSigma | 746436 |
| Sodium phosphate dibasic (ACS) | MilliporeSigma | 795410 |
| Potassium phosphate (ACS) | Fisher Scientific | P285 |
| Corning® RPMI 1640 | Corning | 10-040-CM |
| HyClone™ RPMI 1640 | Cytiva | SH30027.LS |
| RPMI 1640, no glutamine, no glucose | MP Biomedicals | 091646854 |
| Gibco™ RPMI 1640, no glucose | Fisher Scientific | 11879020 |
| Corning™ DMEM with L-glutamine, 4.5g/L glucose and sodium pyruvate | Corning | 10-013-CM |
| HyClone™ DMEM with L-glutamine, 4.5g/L glucose and sodium pyruvate | Cytiva | SH30243.LS |
| Corning™ DMEM with L-glutamine, 4.5g/L glucose, without sodium pyruvate | Corning | 10-017-CM |
| HyClone™ DMEM with L-glutamine, 4.5g/L glucose, without sodium pyruvate | Cytiva | SH30022.LS |

| | | |
|---|---|---|
| Corning™ DMEM/F12 50/50, 15 mM HEPES | Corning | 10-092-CM |
| HyClone™ DMEM/F12 50/50, 15 mM HEPES | Cytiva | SH30023.02 |
| Corning® 0.25% Trypsin, 0.1% EDTA | Corning | 25-053-CI |
| Corning® Penicillin-Streptomycin solution, 100X | Corning | 30-002-CI |
| HyClone™ Penicillin-Streptomycin solution, 100X | Cytiva | SV30010 |
| D-glucose | MilliporeSigma | G7021 |
| Sodium acetate | MilliporeSigma | S2889 |
| Sodium-L-lactate | MilliporeSigma | L7022 |
| L-glutamine | MilliporeSigma | G3126 |
| D-galactose | MilliporeSigma | G5388 |
| Triacetin | MilliporeSigma | 525073 |
| Sodium pyruvate | Fisher Scientific | BP356 |
| Sodium formate | Fisher Scientific | 446951000 |
| Sodium propionate | MilliporeSigma | P5436 |
| Sodium butyrate | MilliporeSigma | B5887 |
| Palmitic acid | MilliporeSigma | P0500 |
| Stearic acid | TCI Chemicals | S0163 |
| Oleic acid | TCI Chemicals | O0180 |
| Phytanic acid | A2B Chem LLC | AF00416 |
| Pristanic acid | LGC Standards | TRC-P118000 |
| Octanoic acid | MilliporeSigma | C2875 |
| Cholesterol | MilliporeSigma | C8667 |
| Ethyl acetate | MilliporeSigma | 1.03649 |
| Lipid Mixture 1 (LM1) | MilliporeSigma | L0288 |
| [$^{13}C_6$] D-glucose | Cambridge Isotope Laboratories | CLM-1396 |
| [$^{13}C_5$] D-glucose | Cambridge Isotope Laboratories | CLM-1822-H |
| [$^{13}C_2$] sodium acetate | Cambridge Isotope Laboratories | CLM-440 |
| Hydrogen peroxide | MilliporeSigma | 1.08600 |
| Copper(II) sulfate pentahydrate (ACS) | MilliporeSigma | 209198 |
| EquiSPLASH™ LIPIDOMIX™ Quantitative Mass Spec Internal Standard | Avanti Research | 330731 |

| | | |
|---|---|---|
| (2-hydroxypropyl)-β-cyclodextrin | MilliporeSigma | C0926 |
| Dimethyl sulfoxide | Fisher Scientific | J66650AD |
| Poly-L-lysine | MilliporeSigma | P2636 |
| Potassium hydroxide (ACS) | MilliporeSigma | 221473 |
| PMSF | Roche | 10837091001 |
| Ponceau S solution | MilliporeSigma | P7170 |
| Tris base | Fisher Scientific | BP152-1 |
| Glycine | MilliporeSigma | G8898 |
| Methanol (peroxide-free) | Fisher Scientific | BP1105 |
| Ethanol 200 proof | Fisher Scientific | 8003C |
| Sodium dodecyl sulfate | MilliporeSigma | L3771 |
| Hydrochloric acid | Fisher Scientific | 72033 |
| TWEEN® 20 | MilliporeSigma | P1379 |
| EDTA disodium salt | MilliporeSigma | E5134 |
| TERGITOL™ solution Type NP-40 | MilliporeSigma | NP40S |
| Sodium deoxycholate | MilliporeSigma | 30970 |
| Agarose | Fisher Scientific | BP164500 |
| Glacial acetic acid | Fisher Scientific | A38 |
| β-mercaptoethanol | Fisher Scientific | AAJ6674230 |
| GelRed nucleic acid gel stain, 10,000X | Biotium | 41003 |
| Precision plus protein dual color standards | Bio-Rad | 1610374 |
| Immobilon western chemiluminescent HRP substrate | MilliporeSigma | WBKLS0100 |
| 1 kb DNA ladder | New England Biolabs | N055S |
| Glycerol | MilliporeSigma | G5516 |
| LB broth (Lennox) | MilliporeSigma | L3022 |
| Ampicillin sodium salt | MilliporeSigma | A9518 |
| Polyethylenimine (PEI) | MilliporeSigma | 408727 |
| Polybrene | MilliporeSigma | 107689 |
| Synperonic F108 | MilliporeSigma | 07579 |
| Puromycin dihydrochloride | Fisher Scientific | BP2956100 |
| Hygromycin B | Roche | 50-100-3311 |
| Blasticidin S hydrochloride | MilliporeSigma | 203350 |
| G418 sulfate | Gemini Bio | 400-111P |
| Resazurin sodium salt | Acros Organics | AC18990 |
| Trypan blue stain | Fisher Scientific | T10282 |
| Chloroform | Fisher Scientific | 43685 |

| | | |
|---|---|---|
| Di-isopropyl ether | MilliporeSigma | 296856 |
| 1-butanol, Thermo Scientific Chemicals | Fisher Scientific | 41867 |
| 1-butanol, SigmaAldrich | MilliporeSigma | 34867 |
| Fasnall | Enamine | EN300-45430166 |
| GSK2194069 | Tocris | 5303 |
| NDI-091143 | Ambeed | A1194991 |
| BMS-303141 | MilliporeSigma | SML0784 |
| AZD3965 | A2B Chem LLC | AA72701 |
| AZD0095 | A2B Chem LLC | BL14859 |
| VY-3-135 | Medinoah Company | 90-2156 |
| VY-7-137 | Medinoah Company | Custom |
| **Biological samples** | | |
| Catalase from bovine liver | Fisher Scientific | AAJ12885ME |
| Foundation™ fetal bovine serum (FBS) | Gemini Bio | 900-108 |
| Fetal bovine serum, dialyzed, 0.1 µm sterile-filtered (dFBS) | Gemini Bio | 100-108 |
| HyClone™ fetal bovine serum, charcoal/dextran treated (HyClone LD-FBS) | Cytiva | SH3006803 |
| PurMa premium fetal bovine serum (PurMa-FBS) | PurMa Biologics, LLC | P3F010301 |
| PurMa lipid-depleted fetal bovine serum (PurMa-LD-FBS) | PurMa Biologics, LLC | P3F312304 |
| Cocalico lipid-depleted fetal bovine serum (Cocalico LD-FBS) | Cocalico Biologicals | 55-0116 |
| **Antibodies** | | |
| B-actin monoclonal antibody [2D4H5) | ProteinTech | 66009-1-Ig |
| ACSS1 polyclonal antibody | ProteinTech | 17138-1-AP |
| AceCS1 (ACSS2) rabbit monoclonal antibody [D19C6] | Cell Signaling Technology | 3658S |
| IRDye 680RD donkey anti-rabbit IgG | LI-COR Biosciences | 926–68073 |
| IRDye 800 CW goat anti-mouse IgG | LI-COR Biosciences | 926–32210 |
| Anti-rabbit IgG, HRP-linked antibody | Cell Signaling Technology | 7074S |

| | | |
|---|---|---|
| Anti-mouse IgG, HRP-linked antibody | Cell Signaling Technology | 7076S |
| **Experimental models: cell lines** | | |
| HCC1569 | ATCC | CRL-2330 |
| HCC1419 | ATCC | CRL-2326 |
| BT-474 | ATCC | HTB-20 |
| HT-55 | MilliporeSigma | 85061105 |
| WM793 | Dr. Meenhard Herlyn, The Wistar institute | |
| T47D | ATCC | HTB-133 |
| U-937 | Dr. Alessandro Gardini, The Wistar Institute | |
| LN229 | ATCC | CRL-2611 |
| COLO800 | MilliporeSigma | 93051123 |
| MP65 | ATCC | CRL-3299 |
| Jurkat | Dr. Daniel Claiborne, The Wistar Institute | |
| MOLM-13 | Dr. Martin Carroll, University of Pennsylvania | |
| MOLM-14 | Dr. Martin Carroll, University of Pennsylvania | |
| HS578T | ATCC | HTB-126 |
| NCI-H2066 | ATCC | CRL-5917 |
| HL-60 | Dr. Alessandro Gardini, The Wistar Institute | |
| MCF7 | ATCC | HTB-22 |
| HepG2 | ATCC | HB-8065 |
| SK-BR-3 | ATCC | HTB-30 |
| THP-1 | Dr. Alessandro Gardini, The Wistar Institute | |
| A549 | ATCC | CCL-185 |
| CAL120 | DSMZ | ACC 459 |
| BT-549 | ATCC | HTB-122 |
| HEK-293 | ATCC | CRL-1573 |
| HEK-293T | ATCC | CRL-3216 |
| L-428 | DSMZ | ACC 197 |
| LOX-IMVI | MilliporeSigma | SCC201 |
| HCT116 | ATCC | CCL-247 |
| MDA-MB-231 | ATCC | CRM-HTB-26 |
| D42 parental (*Acly f/f*) | Dr. Kathryn E. Wellen, University of Pennsylvania | |
| D42 m*Acly* KO | Dr. Kathryn E. Wellen, University of Pennsylvania | |

| | | |
|---|---|---|
| D42 m*Acly* KO, hACLY WT | Dr. Kathryn E. Wellen, University of Pennsylvania | |
| D42 m*Fasn* KO | Dr. Kathryn E. Wellen, University of Pennsylvania | |
| D42 m*Fasn* KO, hFASN WT | Dr. Kathryn E. Wellen, University of Pennsylvania | |
| B6Tag2.03 | Dr. Michael Coleman, University of North Carolina, Chapel Hill | |
| **Bacterial and virus strains** | | |
| One shot Stbl3 competent *E. coli* | Fisher Scientific | C737303 |
| Lentivirus pFUGW-Bsd-EFS>hCas9 | Addgene | 52962-LV |
| Lentivirus mouse whole genome pooled dual gRNA library | VectorBuilder | Lib190505-1050kpm |
| Lentivirus human whole genome dual gRNA library | VectorBuilder | Lib190505-1046fgb |
| **Oligonucleotides** | | |
| MISSION® pLKO.1-puro non-mammalian shRNA control plasmid DNA | MilliporeSigma | SHC002 |
| MISSION® pLKO.1-puro human ACSS1 shRNA | MilliporeSigma | TRCN0000045380 |
| MISSION® pLKO.1-puro human SLC16A13 shRNA #1 | MilliporeSigma | TRCN0000038624 |
| MISSION® pLKO.1-puro human SLC16A13 shRNA #2 | MilliporeSigma | TRCN0000038625 |
| MISSION® pLKO.1-puro human SLC16A13 shRNA #3 | MilliporeSigma | TRCN0000038627 |
| **Recombinant DNA** | | |
| psPAX2 | Addgene | 12260 |
| pVSV-G | Addgene | 138479 |
| pLKO.1 H2B-GFP | Dr. Yaron Fuchs, Technion Israel Institute of Technology | 25999 (Addgene) |
| pLV-Bsd-humanACSS1-HA | VectorBuilder | VB210630-1169uut |
| pLV-Hygro-humanACSS2-FLAG | VectorBuilder | VB210630-1159sad |

| | | |
|---|---|---|
| pKLV2-U6gRNA5(gGFP)-PGKBFP2AGFP-W (Cas9 BFP-gGFP reporter) | Addgene | 67980 |
| **Software and algorithms** | | |
| R | The R Project for Statistical Computing | 4.3.1 |
| RStudio | Posit Software, PBC | 2023.12.1 |
| ProteoWizard | ProteoWizard Software Foundation | 3.0.20365 |
| MAVEN | Rabinowitz Lab, Princeton University | 6.82 |
| Analyst | AB SCIEX LLC | 1.7.3 HotFix 1 |
| MultiQuant | AB SCIEX LLC | 3.0 HotFix 4 |
| LipidSearch | ThermoScientific | 4.2 |
| Biorender | https://www.biorender.com | |
| Adobe Illustrator | Adobe, Inc. | 28.2 |
| Prism | GraphPad | 10.4.1 |
| Excel | Microsoft Corporation | Version 2507 |
| Image Studio | LICORBio | 3.0 |
| Empiria Studio Software | LICORBio | 3.1 |
| FlowJo | Becton, Dickinson and Company (BD) | 10.10.0 |
| ImageAnalyzer | Tecan | 1.2 |

**Table 2.1: Key resources.**

### *Cell culture*

A549, BT-474, HCT116, HEK-293, HEK-293T, HepG2, HT-55, LN229 and MP65 cells were maintained in culture using DMEM medium (with pyruvate) supplemented with 10% fetal bovine serum (FBS) and 1X penicillin-streptomycin (complete DMEM). All other cell lines were maintained in culture using DMEM/F12 medium supplemented with 10% FBS and 1X penicillin-streptomycin (complete DMEM/F12). Cells were kept in a humidified incubator (HERAcell vios 160i, Thermo Fisher Scientific) at 37 °C and 5% $CO_2$ and passaged when surface confluency reached 80%. Cell lines were regularly checked for *Mycoplasma spp.* contamination with the abm™ Mycoplasma PCR Detection Kit (cat. no. G238). No cell line was maintained beyond passage 25 after thawing. All cell lines used do not appear in the

Register of Misidentified Cell line maintained by the International Cell Line Authentication Committee (v13, April 2024).

### *Medium metabolite consumption assay*

To assess the secretion or consumption of metabolites in culture medium, one day before the start of the experiment $5{\cdot}10^5$ cells were seeded with 3 mL of RPMI 1640 supplemented with 10% FBS. A set of three 6-cm dishes was used for each time point measured. On the day of the experiment, the medium was replaced with 2 mL of RPMI 1640 supplemented with 10% dialyzed fetal bovine serum (dFBS), unless a different serum is specified, and additional metabolites or drugs mentioned in the figure description for each result. For experiments where glucose was replaced with galactose, medium formulated without glucose was supplemented with galactose at a final concentration of 11.1 mM, followed by the addition of 10% dFBS. For experiments where the medium pH was modified, 6 M hydrochloric acid was added to the medium solution to achieve the specified pH value. Fasnall, GSK2194069, AZD3965, AZD0095, VY-3-135 and VY-7-137 were provided to the cells at the final concentration specified in each experiment starting from a stock solution dissolved in dimethyl sulfoxide (DMSO). The control condition (vehicle) was supplemented with a volume of DMSO equal to that of the treated conditions, which never exceeded 1% v/v. At the start of the experiment ($t_0$), and at each time point measured, 0.1 mL of medium solution was collected, and cells were counted with the Countess™ II FL Automated Cell Counter (Thermo Fisher Scientific, cat. no. AMQAF1000). In brief, cells were detached by treating with 0.5 ml of trypsin and, after 5 minutes of incubation, 0.5 ml of complete medium was added to quench trypsin. Cells were resuspended by pipetting and transferred to Eppendorf tubes. After vortexing, 50 µl of cell suspension was mixed with 50 µl of trypan blue solution. Three replicates (separate dishes) were used per time point, with one Countess chip (two chambers) per dish. Only the number and average cell diameter of live cells were reported. Dead cell fraction did not exceed 5% of total cells throughout all conditions and cell lines. To extract polar metabolites, 0.4 mL of 100% methanol (80% final) was added to medium samples. After vortexing, samples were stored at -80 °C before further processing. Samples were then centrifuged at 18,000 *x* g and 4 °C for 20 minutes. The supernatant was transferred

to new Eppendorf tubes and centrifuged again with the same parameters. After centrifugation, the extracts were transferred to glass LC-MS vials and analyzed on a SCIEX QTRAP5500 mass spectrometer. Custom external standard solutions at known concentrations for acetate, glucose, and lactate, in addition to samples of RPMI 1640, DMEM and DMEM/F12 media, were used to create calibration curves associating signal intensity and metabolite concentration. The metabolite-associated signal intensity from samples was interpolated to its specific curve to determine the concentration. The absolute value of net flux for consumption or secretion of each quantitated metabolite was calculated in the following manner:

$$Net\ flux\ \left[\frac{mM}{h}\right] = \left|\frac{n_{t_0} - n_{t_1}[nmol]}{PCV_{int}[\mu L \cdot h]}\right| \quad (1)$$

$n_{t_0} - n_{t_1}$ indicates the difference of a metabolite's quantity between the start and the end of the experiment. $PCV_{int}$ indicates the integrated packed cell volume throughout the duration of the experiment, which was calculated by assuming cell shape to be spherical and applying the formula for the volume of a sphere. In order to account for the integrated number of cells during the entire duration of the experiment, $PCV_{int}$ was derived in the following manner (setting $t_0 = 0$):

$$N(t) = N(t_0) \cdot e^{rt} \quad (2)$$

$$\int N(t)dt = \int N(t_0) \cdot e^{rt} dt = N(t_0) \cdot \frac{e^{rt}}{r} + c \quad (3)$$

$$\int_{t_0}^{t_1} N(t)dt = N(t_0) \cdot \frac{e^{rt_1}}{r} - N(t_0) \cdot \frac{e^{rt_0}}{r} = \frac{N(t_0)}{r} \cdot \left(e^{rt_1} - e^{rt_0}\right) \quad (4)$$

$$\int_{t_0}^{t_1} N(t)dt = \frac{N(t_0)}{r} \cdot \left(e^{rt_1} - 1\right) \quad (5)$$

$$PCV_{int} = \frac{4}{3}\pi R^3 \cdot \left[\frac{N(t_0)}{r} \cdot \left(e^{rt_1} - 1\right)\right] \quad (6)$$

$R$ indicates the average cell radius measured. $N(t)$ indicates the number of cells at the time t. $r$ indicates the proliferation rate specific for each cell line, which was calculated as:

$$r = \frac{ln\left(\frac{N(t_1)}{N(t_0)}\right)}{t_1} \quad (7)$$

To calculate glutamine availability throughout the period of culture as described in **Fig. 5.4**, the area-under-the-curve of medium glutamine concentration between $t_0$ and 72 hours was calculated in Prism 10.4.1

### *Stable isotope tracing*

For isotope tracing experiments, $5{\cdot}10^5$ BT-474 cells were seeded with 3 mL of complete RPMI 1640 in 6-cm dishes the day before the experiment. At the beginning of the experiment, for each condition in triplicate the medium was replaced with 3 mL of RPMI 1640 (without glucose and glutamine) supplemented with 10% dFBS, one of the isotope tracers, and either unlabeled glucose or glutamine depending on which tracer was added. The tracer concentrations matched the medium concentration for the corresponding unlabeled nutrient in the case of $^{13}C_6$-glucose and $^{13}C_5$-glutamine, while $^{13}C_2$-acetate was provided at a final concentration of 1 mM. For each tracer condition, VY-3-135 was provided to the cells at a final concentration of 1 µM from stock solution dissolved in DMSO, while only for the $^{13}C_2$-acetate condition VY-3-135 was also given at 10 µM concentration. The relative control condition (vehicle) for each tracer and drug concentration was supplemented with 0.1% v/v DMSO. For intracellular metabolite extraction, the medium was aspirated and cells were washed with 3 mL of PBS. Cells were then scraped in 500 µl of ice-cold 80% methanol and all the content was transferred to Eppendorf tubes. Samples were processed in the same way as described above for medium samples and analyzed on a Thermo Q Exactive HF-X mass spectrometer.

### *Intracellular metabolite content assay*

To measure the relative and absolute concentration of metabolites inside cultured cells, one day before the start of the experiment $5{\cdot}10^5$ cells were seeded with 3 mL of RPMI 1640

supplemented with 10% FBS. On the day of the experiment, the medium was replaced with 3 mL of RPMI 1640 supplemented with 10% dialyzed fetal bovine serum (dFBS) and additional metabolites or drugs specified in the description for each figure. A set of three 6-cm dishes was used for each condition tested. Fasnall, GSK2194069, VY-7-137, and BMS-303141 were provided to the cells at the final concentration specified in each experiment starting from a stock solution dissolved in DMSO. The control condition (vehicle) was supplemented with a volume of DMSO equal to that of the treated conditions, which never exceeded 1% v/v. NDI-091143 was provided to the cells from a stock solution dissolved in 10% v/v DMSO and 20% v/v (2-hydroxypropyl)-β-cyclodextrin. After 24 hours of incubation, intracellular metabolite extraction and processing were performed as described above for the stable isotope tracing experiment. Samples were analyzed on a SCIEX QTRAP 5500 mass spectrometer. Relative quantitation between experimental conditions or absolute concentrations were reported. To derive intracellular concentrations, initial concentrations calculated by interpolation of a standard curve were multiplied by a coefficient accounting for sample dilution in the following manner:

$$k_{\frac{cells}{std}} = \frac{V_{actual\ of\ std}}{V_{actual\ of\ cells}} \tag{8}$$

$V_{actual\ of\ std}$ indicates the actual volume of the standard solution before extraction that is injected, calculated by multiplying the volume injected for LC-MS analysis by the dilution ratio used during methanol extraction. $V_{actual\ of\ cells}$ indicates the actual cell volume before extraction that was injected, calculated by multiplying measured PCV by the volume injected for LC-MS analysis and dividing by the volume of methanol used for extraction.

### *LC-MS metabolomics on SCIEX QTRAP 5500*

Analytes were separated on a SeQuant® ZIC®-pHILIC 150 x 2.1 mm column with 5 µm particles (MilliporeSigma cat. no. 1504600001 and 1504380001). Liquid chromatography parameters were as follows. Solvent A was water with 0.01% ammonium hydroxide and 20 mM ammonium bicarbonate and solvent B was acetonitrile. A linear solvent gradient of a total duration of 22.5 min was started with 0.2 ml/min flow rate of 80% solvent B, 12.5 min –

30%, 15 min – 30%, 15.2 min – 80%, 20 min – 80%, 21 min – flow rate 0.3 ml/min, 22 min – flow rate 0.3 ml/min, 22.1 min – flow rate 0.2 ml/min. The autosampler temperature was maintained at 4 °C and the column was heated to 40 °C. The injection volume was 1 µl for medium samples, 2 µl for standard solutions and 5 µl for cell extracts. ESI source parameters were as follows: curtain gas 35, collision gas "Medium", ion spray voltage 4500 V for both polarity modes, probe temperature 500 °C, ion source gas 1 and 2 at 70. Data were recorded in the polarity switching mode with scheduled advanced multiple-reaction monitoring (MRM) with most peaks acquired in 120 s windows. Pause between mass ranges 2 ms, minimum dwell time 2 ms, maximum 250 ms. MRM parameters were optimized by the direct injection of pure chemical standards. Details of the MRM tables are available upon request and will be included when the mass spectrometry data is deposited in Metabolomics Workbench. Data were analyzed in MultiQuant 3.0 and peak integration for metabolites of interest was manually corrected when necessary. Limit of detection (LOD) for each analyte was defined as the analyte concentration required to produce a signal greater than three times the standard deviation of the noise signal from blank samples.

### *LC-MS metabolomics on Thermo Q Exactive HF-X*

The metabolomics analysis for isotope tracing in BT-474 cells was performed at The Wistar Institute Proteomics and Metabolomics Shared Resource. The chromatography method on the Thermo Fisher Scientific Q Exactive HF-X mass spectrometer was identical to the one described above for the SCIEX LC-MS system. The HESI ion source voltage was set to the following parameters: 3,600 V in both polarity modes, sheath gas 30, auxiliary gas 5, spare gas 0, probe heater 200 °C, capillary temperature 325 °C, S-Lens RF level 65. The mass spectrometer was set to acquire data in the polarity-switching mode averaging two microscans with 60,000 resolution, automatic gain control (AGC) target $5 \cdot 10^6$, scan range 72-1080 m/z, and maximum orbitrap injection time (IT) 200 ms. Data were converted into the mzXML format by ProteoWizard and analyzed in MAVEN. All $^{13}C$ isotopologue abundances were corrected by considering the natural abundance of $^{13}C$.

*Lipid removal from serum*

The procedure for the removal of lipids from dialyzed fetal bovine serum was modified from a previously published protocol (243). In short, dFBS of the same production lot (A62H02L) used for all experiments was mixed 1:1 with a solution of organic solvents composed of 0.2 vol. n-butanol and 0.8 vol. di-isopropyl ether. After stirring for 30 minutes at 300 rpm and 37 °C, the mix was centrifuged at 4,000 x *g* and 37 °C for 15 minutes to separate the upper organic phase containing lipids and the lower aqueous phase containing serum proteins. The lower phase was recovered while the upper phase was discarded. The production of lipid-depleted serum was performed twice producing two separate products (LD-dFBS batch #1 and batch #2) and only in batch #2 the aqueous phase was mixed a second time with n-butanol and di-isopropyl ether and separated in the same manner to increase the fraction of lipids removed. After collecting the aqueous phase, each product batch was mixed with a volume of di-isopropyl ether equal to the starting volume of serum. After stirring for 30 minutes at 300 rpm and 37 °C, the mix was centrifuged at 4,000 x *g* and 37 °C for 15 minutes and the lower phase was recovered while the upper phase was discarded. To remove organic solvent contaminants, 500 mL of lipid-depleted serum was dialyzed inside 10K MWCO Slide-A-Lyzer™ dialysis flasks (Fisher Scientific, PI87762) against 4 L of saline solution (9 g/L sodium chloride, 0.34% w/v 2-hydroxypropyl-β-cyclodextrin). Dialysis was repeated six times with fresh saline solution every 12 hours. Protein content in the lipid-depleted serum was measured by Pierce™ BCA protein assay kit (Fisher Scientific, 23227) and compared to control dFBS to ensure equal concentrations. The final product batches of LD-dFBS were sterilized by filtration through 0.2 µm Nalgene™ Rapid-Flow™ Sterile Disposable Filter Units with PES membranes (Fisher Scientific, 567-0020) and stored at -20 °C.

*Serum sample preparation for LC-MS lipidomics analysis*

To assess the lipid content of the different sera, the EquiSPLASH™ LIPIDOMIX solution containing stable deuterium-labeled isotopologues representing 13 lipid classes was diluted 1:20 into each sample to act as an internal standard for normalization, and lipids were extracted from triplicate samples by the Folch method (244). Briefly, 50 µL of sample

was mixed inside 13 x 100 mm Pyrex glass tubes with 1 mL of methanol and 2 mL chloroform. After vortexing, 0.6 mL of PBS was added to initiate phase separation and samples were centrifuged at 3000 x *g* for 1 minute at room temperature. The lower phase was collected, and a slow stream of nitrogen gas was allowed to blow over the surface until the complete evaporation of the samples. The dried lipids were redissolved in 0.3 mL of a 1:1 mix of methanol:isopropanol and stored in glass LC-MS vials at -20 °C prior to analysis on a Thermo Scientific Q Exactive HF-X mass spectrometer.

### *Serum sample preparation for LC-MS free fatty acid analysis*

To assess the global free fatty acid content of the different sera, 1 mL of each sample in triplicate was freeze-dried overnight at 48 °C on a Harvest Right Pro Freeze Dryer (model no. HRFDMBKP). Lipids were extracted by the Folch method in the same way as described above for the lipidomics analysis until the step of evaporation by nitrogen gas blowing. To perform saponification, the dried lipids were redissolved in 1 mL of a 0.3 M KOH solution in 1:1 methanol:isopropanol and incubated at 95 °C for one hour. Afterwards, 100 µL of formic acid was added, followed by 2 mL of hexane for fatty acid extraction. After vortexing, samples were centrifuged at 3,000 x *g* for 1 minute at room temperature and the upper hexane phase was collected into new glass tubes. The extraction step was repeated and the two hexane phases for each sample were added together and dried under a nitrogen gas stream. Samples were redissolved in 1 mL of 1:1 methanol:isopropanol and stored in glass LC-MS vials at -20 °C prior to analysis on a SCIEX QTRAP5500 mass spectrometer. Custom external standard solutions at known concentrations for palmitic acid, stearic acid, oleic acid, phytanic acid and pristanic acid were used to create calibration curves associating signal intensity and concentration.

### *LC-MS lipidomics analysis on Thermo Q Exactive HF-X*

The lipidomics analysis was performed at The Wistar Institute Proteomics and Metabolomics Shared Resource. Ultra-high performance liquid chromatography (UHPLC)-electrospray-tandem mass spectrometry was performed independently for positive and negative ion modes on a Thermo Fisher Scientific Q Exactive HF-X mass spectrometer and

in-line Vanquish Horizon UHPLC System. Gradient LC separation used an Accucore C30 Column (2.1 mm x 150 mm, 2.6 µm particle size, ThermoScientific, cat. no. 27826-152130) with 50:50 acetonitrile/water and 88:10:2 isopropanol/acetonitrile/water mobile phase solvents, both containing 5 mM ammonium formate and 0.1% formic acid. MS1 scans were acquired at 120k resolution, and data-dependent MS2 scans were acquired for the top 20 ions at 15k resolution with 0.4 m/z isolation width and stepped NCE 20/30/40. Lipid species were identified based on MS/MS fragmentation compared to an in-silico database of >1.7 million species based on known fragmentation of lipids and quantified by peak area using LipidSearch 4.2. Data were corrected by EquiSPLASH™ internal standard for represented lipid classes (Cer, ChE, DG, LPC, LPE, MG, PC, PE, PG, PI, PS, SM, and TG). For all datasets, identified lipid species were filtered by expected adduct and annotation grade based on lipid class.

*LC-MS free fatty acid analysis on SCIEX QTRAP5500*

Analyte separation was achieved with a Phenomenex Kinetex XB-C18 column (cat. no. 00F-4496-Y0; 150 x 3 mm, 2.6 µM particle size) on a liquid chromatograph Shimadzu Prominence LC-20. The column compartment of HPLC is maintained at 65 °C, autosampler – at 20 °C. The mobile phase is composed of the two solvent mixtures: A – 60:40 acetonitrile:water with 10 mM ammonium formate, B – 90:8:2 isopropanol: acetonitrile:water with 10 mM ammonium formate. For solvent B, it was important to dissolve ammonium formate in water first and then mix it with the organic solvents. The buffer loop in the autosampler is filled with a mix of 50:50 isopropanol:methanol (95% of the final volume) and 5 % water. The injection volume was 1 µl. Solvent flow was maintained at 0.333 ml/min. Mobile phase composition was changing according to the following program (with respect to solvent B): 0 min – 15%; 4.5 min – 60%; 12 min – 82%; 12.75 min – 95%; 16.5 min – 100%, 22.5 min – 100%; 22.6 min – 15%, maintained until 25 min. The mass spectrometry analysis was performed on SCIEX QTRAP5500. Chromatographic eluent was ionized in an electrospray ion source operating in the negative mode with the following parameters: collision gas pressure at “Medium”, Ion Source Gas 1 and 2 at 70 AU, Curtain Gas at 35 AU, source temperature 650 °C, source voltage -4,500 V, entrance potential (EP) -10 V. For all analytes, multiple reaction monitoring

(MRM) with optimized declustering potentials (DP), collision energies (CE), and collision cell exit potentials (CEX) were used according to **Table 2.2**. All fatty acids were monitored as parent ions passing through the collision cell. Applying the above-minimal collision energy increased the mass spectrometer sensitivity. Three attenuated channels with suboptimal sensitivity (increased CE) were introduced for the most abundant fatty acids to extend the dynamic range of the method and avoid oversaturation of the detector. Their parent ion mass was changed to distinguish from the original, optimized MRMs (red font). All MRMs used the UNIT resolution (±0.5 Da), 2 ms pause between masses, 2 ms minimal dwell time, 250 ms maximal dwell time. The method was built using the sMRM mode, when each MRM was invoked in a 240 s window centered on the corresponding retention time (RT).

| Desat | N(C) | Q1 | Q3 | RT (min) | ID | DP | CE | CXP |
|---|---|---|---|---|---|---|---|---|
| 0 | 10 | 171.103 | 171.103 | 2.50 | FA_10:0 | -60 | -10 | -20 |
| 0 | 11 | 185.118 | 185.118 | 2.50 | FA_11:0 | -60 | -10 | -20 |
| 0 | 12 | 199.134 | 199.134 | 4.57 | FA_12:0 | -60 | -15 | -20 |
| 0 | 13 | 213.15 | 213.15 | 4.93 | FA_13:0 | -90 | -15 | -20 |
| 0 | 14 | 227.165 | 227.165 | 5.53 | FA_14:0 | -140 | -15 | -20 |
| 0 | 15 | 241.181 | 241.181 | 6.08 | FA_15:0 | -140 | -15 | -15 |
| 2 | 16 | 251.165 | 251.165 | 5.3 | FA_16:2 | -110 | -10 | -15 |
| 1 | 16 | 253.181 | 253.181 | 5.78 | FA_16:1 | -140 | -15 | -25 |
| 0 | 16 | 255.197 | 255.197 | 6.6 | FA_16:0 | -140 | -15 | -20 |
| 0 | 16 | 255.198 | 255.197 | 6.6 | FA_16:0 ATTN | -140 | -36 | -20 |
| 1 | 17 | 267.197 | 267.197 | 6.3 | FA_17:1 | -140 | -15 | -25 |
| 0 | 17 | 269.176 | 269.176 | 7 | FA_17:0 | -120 | -20 | -15 |
| 0 | 16 | 271.228 | 271.228 | 4.2 | FA_16:0-OH | -170 | -20 | -20 |
| 4 | 18 | 275.176 | 275.176 | 4.77 | FA_18:4 | -100 | -10 | -30 |
| 3 | 18 | 277.166 | 277.166 | 5.63 | FA_18:3 | -110 | -15 | -30 |
| 2 | 18 | 279.197 | 279.197 | 6.07 | FA_18:2 | -140 | -15 | -30 |
| 1 | 18 | 281.212 | 281.212 | 6.74 | FA_18:1 | -130 | -20 | -25 |
| 1 | 18 | 281.213 | 281.212 | 6.74 | FA_18:1 ATTN | -130 | -39 | -25 |
| 0 | 18 | 283.191 | 283.191 | 7.47 | FA_18:0 | -170 | -15 | -15 |
| 0 | 18 | 283.192 | 283.191 | 7.47 | FA_18:0 ATTN | -170 | -38 | -15 |
| 3 | 19 | 291.181 | 291.181 | 6.1 | FA_19:3 | -150 | -10 | -15 |
| 2 | 19 | 293.212 | 293.212 | 6.55 | FA_19:2 | -80 | -10 | -25 |
| 1 | 19 | 295.191 | 295.191 | 7.13 | FA_19:1 | -300 | -15 | -25 |
| 0 | 19 | 297.207 | 297.207 | 8.21 | FA_19:0 | -300 | -15 | -20 |
| 0 | 18 | 299.259 | 299.259 | 4.9 | FA_18:0-OH | -170 | -15 | -30 |
| 5 | 20 | 301.217 | 301.217 | 4.6 | FA_20:5 | -120 | -15 | -30 |

| | | | | | | | | |
|---|---|---|---|---|---|---|---|---|
| 4 | 20 | 303.207 | 303.207 | 5.84 | FA_20:4 | -140 | -10 | -30 |
| 3 | 20 | 305.197 | 305.197 | 6.51 | FA_20:3 | -150 | -15 | -30 |
| 2 | 20 | 307.228 | 307.228 | 7 | FA_20:2 | -150 | -15 | -30 |
| 1 | 20 | 309.207 | 309.207 | 7.55 | FA_20:1 | -280 | -20 | -30 |
| 0 | 20 | 311.223 | 311.223 | 8.34 | FA_20:0 | -300 | -15 | -35 |
| 5 | 21 | 315.233 | 315.233 | 5.79 | FA_21:5 | -120 | -15 | -25 |
| 4 | 21 | 317.223 | 317.223 | 6.75 | FA_21:4 | -140 | -10 | -25 |
| 3 | 21 | 319.213 | 319.213 | 6.93 | FA_21:3 | -120 | -10 | -20 |
| 2 | 21 | 321.243 | 321.243 | 7.49 | FA_21:2 | -140 | -15 | -35 |
| 1 | 21 | 323.223 | 323.223 | 8.23 | FA_21:1 | -300 | -20 | -30 |
| 0 | 21 | 325.238 | 325.238 | 9.25 | FA_21:0 | -300 | -15 | -30 |
| 0 | 20 | 325.275 | 325.275 | 5.9 | FA_20:1-OH | -140 | -10 | -30 |
| 0 | 20 | 327.29 | 327.29 | 5.62 | FA_20:0-OH | -140 | -10 | -30 |
| 5 | 22 | 329.249 | 329.249 | 6.2 | FA_22:5 | -130 | -10 | -30 |
| 4 | 22 | 331.238 | 331.238 | 6.64 | FA_22:4 | -170 | -15 | -30 |
| 3 | 22 | 333.228 | 333.228 | 7.2 | FA_22:3 | -280 | -20 | -35 |
| 2 | 22 | 335.259 | 335.259 | 7.72 | FA_22:2 | -300 | -15 | -25 |
| 1 | 22 | 337.238 | 337.238 | 8.4 | FA_22:1 | -300 | -20 | -30 |
| 0 | 22 | 339.254 | 339.254 | 9.3 | FA_22:0 | -300 | -20 | -30 |
| 0 | 21 | 341.306 | 341.306 | 7 | FA_21:0-OH | -120 | -10 | -35 |
| 1 | 23 | 351.254 | 351.254 | 9.37 | FA_23:1 | -300 | -20 | -30 |
| 0 | 23 | 353.27 | 353.27 | 9.7 | FA_23:0 | -300 | -20 | -30 |
| 0 | 22 | 355.322 | 355.322 | 6.56 | FA_22:0-OH | -160 | -10 | -35 |
| 5 | 24 | 357.28 | 357.28 | 6.85 | FA_24:5 | -170 | -15 | -30 |
| 4 | 24 | 359.27 | 359.27 | 7.33 | FA_24:4 | -210 | -15 | -35 |
| 3 | 24 | 361.26 | 361.26 | 7.9 | FA_24:3 | -300 | -15 | -35 |
| 2 | 24 | 363.29 | 363.29 | 8.5 | FA_24:2 | -300 | -20 | -30 |
| 1 | 24 | 365.27 | 365.27 | 9.27 | FA_24:1 | -300 | -20 | -30 |
| 0 | 24 | 367.285 | 367.285 | 10.18 | FA_24:0 | -300 | -20 | -40 |
| 1 | 25 | 379.285 | 379.285 | 10.33 | FA_25:1 | -300 | -20 | -30 |
| 0 | 25 | 381.301 | 381.301 | 10.67 | FA_25:0 | -300 | -20 | -40 |
| 5 | 26 | 385.311 | 385.311 | 7.6 | FA_26:5 | -170 | -15 | -30 |
| 4 | 26 | 387.301 | 387.301 | 8.49 | FA_26:4 | -210 | -15 | -35 |
| 3 | 26 | 389.291 | 389.291 | 9.13 | FA_26:3 | -300 | -15 | -35 |
| 2 | 26 | 391.322 | 391.322 | 9.35 | FA_26:2 | -300 | -20 | -40 |
| 1 | 26 | 393.301 | 393.301 | 10.87 | FA_26:1 | -300 | -20 | -40 |
| 0 | 26 | 395.317 | 395.317 | 11.12 | FA_26:0 | -300 | -25 | -40 |
| 1 | 27 | 407.317 | 407.317 | 11.38 | FA_27:1 | -300 | -20 | -30 |
| 0 | 27 | 409.332 | 409.332 | 12.5 | FA_27:0 | -300 | -20 | -40 |
| 4 | 28 | 415.332 | 415.332 | 9.3 | FA_28:4 | -210 | -15 | -35 |
| 3 | 28 | 417.322 | 417.322 | 10.08 | FA_28:3 | -300 | -15 | -35 |
| 2 | 28 | 419.353 | 419.353 | 10.88 | FA_28:2 | -300 | -20 | -30 |

| | | | | | | | | |
|---|---|---|---|---|---|---|---|---|
| 1 | 28 | 421.332 | 421.332 | 11.08 | FA_28:1 | -300 | -30 | -50 |
| 0 | 28 | 423.348 | 423.348 | 12.2 | FA_28:0 | -300 | -20 | -50 |
| 0 | 30 | 451.379 | 451.379 | 12.87 | FA_30:0 | -300 | -20 | -50 |
| 0 | 32 | 479.484 | 479.484 | 13.65 | FA_32:0 | -300 | -20 | -50 |
| 0 | 34 | 507.514 | 507.514 | 14.3 | FA_34:0 | -300 | -20 | -50 |
| 0 | 36 | 535.545 | 535.545 | 15.3 | FA_36:0 | -300 | -20 | -50 |
| 0 | 38 | 563.577 | 563.577 | 16 | FA_38:0 | -300 | -20 | -50 |

**Table 2.2: MRM method for free fatty acid analysis.**

*Resazurin reduction assay*

Resazurin reduction was used to assess the short-term effects of medium composition on the assay in **Fig. 5.2** and as a proxy for cell count in all other experiments where it was employed. Sterile 0.15 mg/mL resazurin stock was prepared in PBS. Unless otherwise specified, 100 µL of a suspension of $1{\cdot}10^4$ cells in complete RPMI 1640 was seeded per well in 96-well plates previously coated for 1 hour with a solution of 200 µg/mL poly-l-lysine in PBS buffer. After 6 hours to allow surface attachment, the medium was replaced with 100 µL of RPMI 1640 supplemented with serum, metabolites, and/or drugs as specified in the description for each result figure. For the experiments described in **Fig. 5.1** and **5.2**, the medium was immediately mixed with resazurin stock 1:6, while in all other experiments cells were incubated for 24 or 48 hours as specified for each experiment before the medium was replaced with fresh RPMI 1640 with 10% dFBS mixed with resazurin stock 1:6. After adding resazurin, cells were incubated for 90 minutes, and resorufin fluorescence was measured (560 nm excitation, 590 nm emission wavelengths) on a BMG Labtech CLARIOstar Plus or a Tecan Spark Cyto plate reader.

*Cell proliferation assay*

Cell proliferation was assessed by counting with the Countess™ II FL Automated Cell Counter, in the same way as described above for the medium metabolite consumption assay, in experiments reported in **Fig. 5.2b**, **5.3b** and **5.3c**. For the experiments reported in **Fig. 5.8c**, cell count was obtained by imaging 96-well plates inside a Tecan Spark Cyto plate reader. For the experiments reported in **Fig. 5.12d**, cell count was obtained by imaging 96-well plates incubated at 37 °C and 5% $CO_2$ every hour for 24 hours inside a Tecan Spark Cyto

plate reader. Tecan Spark Cyto images were analyzed with ImageAnalyzer 1.2 to determine cell object count. In all other experiments where cell number is reported, it was done by using the resazurin reduction assay as described above.

### *Cell death assay*

Propidium iodide (PI) cell staining at a concentration of 4 µg/mL was used to assess the percentage of cell death. Control cells were treated with 70% ethanol prior to PI staining to measure the signal for 100% cell death. PI fluorescence signal was measured on an Odyssey M Imager (LICORBio, cat. no. 3350-00). Images were analyzed in Empiria Studio 3.1.

### *Plasmid purification*

Stbl3 competent *E. coli* already transformed with the shRNA constructs were obtained from the MISSION® shRNA repository at The Wistar Institute. Stbl3 competent *E. coli* already transformed with the expression constructs for hACSS1-HA, hACSS2-FLAG, and the Cas9 BFP-gGFP reporter were obtained from VectorBuilder. Stbl3 competent *E. coli* already transformed with the expression constructs for H2B-GFP were obtained as a gift from the laboratory of Dr. Yaron Fuchs. Bacterial cells were incubated for 16-20 hours in 250 mL of LB medium with 100 µg/ml ampicillin at 37 °C under constant 220 rpm shaking. Afterwards, the cell suspension was centrifuged at 6500 x *g* and 4 °C for 15 minutes. Plasmid purification from the cell pellet was performed using the NucleoBond Xtra midi-prep kit (Macherey-Nagel, cat. no. 740410) according to the procedure for low copy plasmids outlined in the kit's manual. The purified DNA was reconstituted in 200 µL of 10 mM Tris buffer (pH 8.0) and the concentration was measured using a DeNovix DS-11 spectrophotometer.

### *Lentiviral vector production*

HEK-293T cells were used to produce the lentiviral vectors employed for packaging shRNA knockdown or expression constructs. Briefly, $15{\cdot}10^6$ were seeded in 15-cm dishes that had been previously coated for 1 hour with a solution of 200 µg/mL poly-l-lysine in PBS buffer. The next day, complexation between 18 µg of psPAX2, 9 µg of pVSV-G and 25 µg of the target plasmids with 100 µg PEI in 1.2 mL of DMEM without FBS was allowed to proceed for 10 minutes at room temperature. Cells were washed with PBS, then 14 mL of DMEM without

FBS and the PEI/DNA suspension were added to the dishes to allow transfection. After one day of incubation, the medium was replaced with 15 mL of complete DMEM. Culture medium containing lentiviral particles was collected and replaced by fresh medium for the following two days. To remove floating HEK-293T cells and avoid inter-cell line contamination, the collected medium was centrifuged at 500 x *g* for 10 minutes and then filtered through a 0.45 µm PES unit (Fisher Scientific, cat. no. FB12566501). Lentivirus-containing medium was stored at -80 °C.

### *Lentiviral transduction*

Stable isogenic cell lines were generated using lentiviral transduction. Lentiviral vectors for all knockdown and expression constructs were produced as described above, except for the hCas9 (pFUGW-Bsd-EFS>hCas9) expression vector which was obtained from Addgene. Target cells were transduced in the presence of 10 µg/mL of polybrene or 1 mg/mL synperonic F108 (the latter only for Jurkat cells as described in **Fig. 5.18**) and either 0.1% viral medium for the hCas9 vector or 20% viral medium for all other lentiviral vectors. Stable cell pools were selected using 1 – 10 µg/mL puromycin (all shRNA vectors), 1 – 10 µg/mL blasticidin S (hACSS1-HA, hCas9), 250 – 1000 µg/mL hygromycin B (hACSS2) or 250 – 1000 µg/mL G418 (hSLC16A13).

### *Flow cytometry*

For propidium iodide (PI) staining, control or GSK2194069-treated HEK-293 cells, previously cultured with either 10% dFBS or 10% LD-dFBS, were stained for 30 minutes with 4 µg/mL PI, then trypsinized, resuspended in FACS buffer (PBS, 2% FBS, 1 mM EDTA), and passed through a 40 µm nylon mesh strainer. PI fluorescence was measured on a BD FACSymphony A5 SE Cell Analyzer and analyzed in FlowJo 10.10.0.

To determine lentiviral transduction efficiency, $1 \cdot 10^5$ cells were seeded in 12-well plates and infected with either lentiviral medium for H2B-GFP (Jurkat, MOLM-13), the human (HEK-293 ACSS2-OE Cas9 clone 73) or mouse (D42 m*Acly* KO Cas9 clone 6, B6Tag2.03 Cas9 clone 15) whole genome gRNA CRISPR library viral medium at volume percentages specified in the figure description for each experiment. After 3 days in incubation, cells were trypsinized,

resuspended in FACS buffer, and passed through a 40 µm nylon mesh strainer. GFP fluorescence was measured on a BD FACSymphony A5 SE Cell Analyzer and analyzed in FlowJo 10.10.0.

The percentage of the target cell line containing active Cas9 expression was determined by transduction with lentiviral vectors for the Cas9 BFP-gGFP construct as described above. Three days after infection, cells were trypsinized, resuspended in FACS buffer, and passed through a 40 µm nylon mesh strainer. GFP and BFP fluorescence was measured on a BD FACSymphony A5 SE Cell Analyzer and analyzed in FlowJo 10.10.0. A clonal cell line population was considered as having homogeneous Cas9 activity if the percentage of the infected subpopulation having lost GFP fluorescence was between 98 to 99%.

### *Long-term culture trial of CRISPR screen conditions*

To determine the viability of CRISPR screen culture conditions, $5{\cdot}10^5$ HEK-293 ACSS2-OE were seeded in 6-cm dishes, previously coated for 1 hour with a solution of 200 µg/mL poly-l-lysine, with 4 mL of RPMI 1640 supplemented either 10% dFBS or 10% LD-dFBS, 50 µm NDI-091143 and 5 mM acetate as described in **Fig. 5.17**. Phase-contrast micrographs were taken with an EVOS M5000 microscope (ThermoScientific, cat. no. AMF5000SV) and cells were trypsinized and re-plated at the days and ratios specified in the figure.

### *Single cell clones*

Single cell clones were obtained for HEK-293 ACSS2-OE Cas9, D42 m*Acly* KO Cas9, and B6Tag2.03 Cas9 lines by flow cytometry assisted cell sorting (FACS) of single cells into three 96-well plates per cell line using a Cytek Aurora CS spectral sorter. Micrographs of the wells were taken daily with a Tecan Spark Cyto plate reader to identify true single clonal populations, and medium was refreshed every three days until the time when cell number allowed for trypsinization and expansion on larger plates. Evaluation of active Cas9 expression for each clone was performed as described above by flow cytometry.

### *CRISPR KO Screen*

To perform the CRISPR KO screen, $5.5 \cdot 10^6$ D42 m*Acly* KO Cas9 clone 6 cells were seeded in ten 15-cm dishes each with 15 mL of complete DMEM without pyruvate, 10 mg/mL polybrene, and 0.0125% v/v of murine whole genome gRNA CRISPR library buffer and incubated at 37 °C and 5% $CO_2$. From day 3 to day 21 of culture, spent medium was replaced with 20 mL of fresh complete DMEM without pyruvate every day and cells were trypsinized when surface confluency reached 80%. Between day 9 and day 17, cells were selected for puromycin resistance by supplementing the medium with 5 µg/mL puromycin. On day 22, cells were trypsinized and $5.5 \cdot 10^6$ cells were seeded in triplicate in 15-cm dishes with 20 mL of RPMI 1640 and the following supplementations for each condition: 1) 10% dFBS; 2) 10% LD-dFBS + 5 mM acetate; 3) 10% LD-dFBS + 5 mM pyruvate; 4) 10% LD-dFBS + 2 mM triacetin. For the following 15 days of culture, the spent medium was replaced with fresh 20 mL every day for each replicate dish. When the confluency of the most rapidly proliferating condition (10% LD-dFBS + 5 mM acetate) reached 80%, cells in all conditions were trypsinized and re-plated while keeping each replicate dish separate. On day 37, each replicate dish was trypsinized and, after washing with ice-cold PBS two times, genomic DNA extraction was performed using the NucleoBond CB 500 genomic DNA extraction kit (Macherey-Nagel cat. no. 740509) according to the manufacturer's instructions. DNA concentration was measured using a DeNovix DS-11 spectrophotometer, and 40 µg of DNA for each replicate was stored at -20 °C. PCR amplification of the gRNA regions, high-throughput sequencing, and gRNA identification was performed by VectorBuilder. Throughout the screen period, green wavelength epifluorescence micrographs of the cells were taken with an EVOS M5000 microscope.

### *Western blot*

For intracellular protein analysis, cells were scraped into ice cold PBS and lysed in RIPA buffer (50 mM Tris pH 8.0, 150 mM NaCl, 1% Triton X-100, 1.0% sodium deoxycholate, 1.0% SDS, pH 8.0) with fresh Pierce™ Protease inhibitor mini tablets (Fisher Scientific, cat.no. A32953), 0.5 mM PMSF, and 1 µL of Benzonase® endonuclease (MilliporeSigma, cat. no. 71205-M). Protein content was measured by BCA assay. For each cell lysate, equal amounts of protein were incubated in 1X Laemmli buffer (Bio-Rad, cat. no. 1610747) supplemented

with 10% β-mercaptoethanol for 5 minutes at 95 °C. Gel electrophoresis of the samples was performed on 4–20% Mini-PROTEAN® TGX™ precast polyacrylamide gels (Bio-Rad, cat. no. 4561096), setting a constant voltage of 50V for the first 20 minutes, followed by 120V for one hour. Separated proteins were transferred onto 0.45 µm nitrocellulose membranes using the Trans-Blot SD Semi-Dry Transfer Cell (Bio-Rad, cat. no. 1703940). Membranes were blocked from non-specific interactions using 5% w/v milk in Tris-buffered saline solution (20 mM Tris, 150 mM NaCl) with 0.1% w/v Tween-20 (TBST) for 1 hour at room temperature prior to overnight incubation with primary antibodies at 4 °C. Primary antibodies were diluted in a solution of 1% w/v bovine serum albumin (BSA) (MilliporeSigma, cat.no. A7030) and 0.05% w/v sodium azide in TBST. Primary antibodies directed against ACSS1 (ProteinTech, cat. no. 17138-1-AP) and ACSS2 (Cell Signaling Technology, cat. no. 3658) were used at a 1:1000 dilution. The primary antibody against β-actin was diluted 1:5000. The next day, membranes were washed three times with TBST and incubated with secondary antibodies at a 1:20000 dilution for 1 hour at room temperature. For fluorophore-conjugated secondary antibodies, final images were collected on a LiCor Odyssey Infrared Imaging System 9120 (LICORBio, cat. no. 26288). For HRP-conjugated secondary antibodies, the membranes were covered for 5 minutes with HRP substrate, and final images were collected on an Amersham Imager 680.

### *Cancer cell line gene expression data*

Data on gene expression levels for cancer cell lines were retrieved from the Cancer Cell Line Encyclopedia on May 15$^{th}$ 2025 through the Broad CCLE Portal (https://depmap.org) as raw RNAseq RPKM values. RNASeq RPKM values were normalized by setting RPKM values of cell line-gene pairs with very low expression levels to 0.01.

A composite score of ACSS1 and ACSS2 expression for the cell lines used in metabolic net flux experiments was calculated as a weighted sum of the normalized RNAseq RPKM values for the two genes from CCLE. The weights used ($w_1$ and $w_2$) were determined by computing a multiple linear regression in Excel using this model:

$$F = w_0 + w_1 G_1 + w_2 G_2 + \varepsilon \quad (9)$$

$F$ indicates the value of net acetate metabolic flux. $G_1$ and $G_2$ represent the expression level of ACSS1 and ACSS2. $w_0$ indicates the baseline value when $G_1 = G_2 = 0$. $w_1$ indicates the change in flux for a one-unit increase of the expression level of $G_1$, holding $G_2$ constant. $w_2$ indicates the change in flux for a one-unit increase of the expression level of $G_2$, holding $G_1$ constant. $\varepsilon$ indicates the residual error.

The heatmap of expression of all transporters was created by identifying solute carrier (SLC) gene names in CCLE and matching them with a curated list of SLC genes produced by integrating the information available on https://slc.bioparadigms.org/, the HUGO Gene Nomenclature Committee (https://www.genenames.org/data/genegroup/#!/group/752), and the most recent SLC transporter list produced by the RESOLUTE Consortium (Goldmann et al., 2025). The heatmap was created in R from a dataset matching normalized $Log_{10}$ RPKM values for each transporter to all CCLE cell lines. Clustering distance rows and columns were Euclidean and clustering method was complete. The heatmap including only SLC16 genes and cell lines used for metabolic net flux experiments was created in Prism 10.4.1 from the same dataset.

### *Triacetin conversion to acetate*

To assess the extent of triacetin hydrolysis in a non-biological environment, a solution of 2 mM triacetin in water was conserved at 4 °C for 6 months. Acetate content was analyzed and compared to a 2 mM triacetin solution made on the same day when metabolite extraction was performed. To assess the extent of enzymatic conversion of triacetin into acetate, $1 \cdot 10^6$ D42 m*Acly* KO cells were seeded in 6-cm dishes, and the following day medium was replaced with 3 mL of RPMI 1640 supplemented with 10% dFBS and 2 mM triacetin. 100 µL of medium was collected after 1 and 24 hours of incubation. Metabolite extraction and metabolomics analysis was performed as described above for the medium metabolite consumption assay.

*Statistics*

The methods used for statistical analysis are reported in the description of each figure. All statistical tests using experimental data were performed in Prism 10.4.1, except for those in **Fig.5.22** which were performed in Excel.

The Pearson correlation coefficient (r) and the coefficient of determination ($R^2$) between standard concentrations and peak intensities, those between metabolic net fluxes for acetate, glucose, and glutamine, as well as those between metabolic net fluxes and the expression levels of ACSS1 and ACSS2 were computed in Prism 10.4.1. The pairwise correlations between ACSS1 or ACSS2 and either all SLC genes (**Table 4.1**, **Fig. 4.3**) or only SLC16 genes (**Table 4.2**) were computed in R. Cell lines having RPKM values of 0.01 for at least one of the two genes in the pair were excluded from the calculation.

The $IC_{50}$ concentration values for NDI-091143 were calculated in Prism 10.4.1 by interpolation of a sigmoidal 4-parameter logistic model with 95% confidence interval (CI).

# CHAPTER 3: ACETATE IS A METABOLIC SOURCE FOR ENERGY PRODUCTION AND BIOSYNTHESIS IN CANCER CELLS

## *3.1 Introduction*

Acetate is recognized as a major alternative nutrient source of acetyl-CoA in cancer cells and immune cells, and its presence consequently influences oxidative respiration, lipid metabolism, and epigenetic regulation to sustain cell proliferation. In this chapter, we sought to build a quantitative and functional understanding of how different cell line models consume acetate, while validating the analytical metabolomics method and the chemical inhibitors that we employ throughout this work to manipulate and study the downstream metabolism of acetate.

## *3.2 Results*

### *LC-MS metabolomics method workflow and validation*

To investigate the metabolic activity of cancer models, our laboratory has developed a targeted metabolomics method employing liquid chromatography-mass spectrometry (LC-MS) to identify and quantify more than 250 polar metabolites. Our methodology, which relies on a triple quadrupole SCIEX QTRAP5500 LC-MS/MS system, allows the direct detection of low molecular weight carboxylic acids (LMWCA) such as short-chain fatty acids (SCFA). SCFA are not directly detected by Orbitrap mass spectrometry systems commonly used in contemporary academic research (245–248). This is due to the high polarity of SCFA, low molecular weight, poor retention on reversed phase chromatographic columns, and poor ionization (249,250). This issue can be addressed by applying chemical derivatization methods that modify the original molecule to improve ionization, molecular fragmentation and, ultimately, allow detection (251). However, derivatization introduces an additional element of variability to the processing of each sample and can lead to additional chemical reactions that complicate accurate identification and quantitation unless appropriate steps are taken to ensure the presence of suitable internal standards that undergo identical preparation steps (252).

With our targeted method, each analyte has been identified and validated from a reference standard in a pure matrix, and its limit-of-detection (LOD) concentration has been determined. As such, post-hoc fragment identification is not necessary, eliminating the possibility of incorrect identification of parental ions from ambiguous detected fragments in an untargeted fashion (253). These capabilities have been employed in this project to measure the impact of a variety of treatments on a panel of cancer cell line models through medium and intracellular metabolomic analyses (**Fig. 3.1**). Absolute quantitation was made possible by the concurrent analysis of custom-made external standard solutions of known concentration for specific analytes of interest, most notably acetate, glucose, and lactate (**Fig. 3.2e**), and of aliquots of the most commonly used commercial culture media, such as RPMI 1640, DMEM, and DMEM/F12 for quality control (QC) and supplementation of the standard curves.

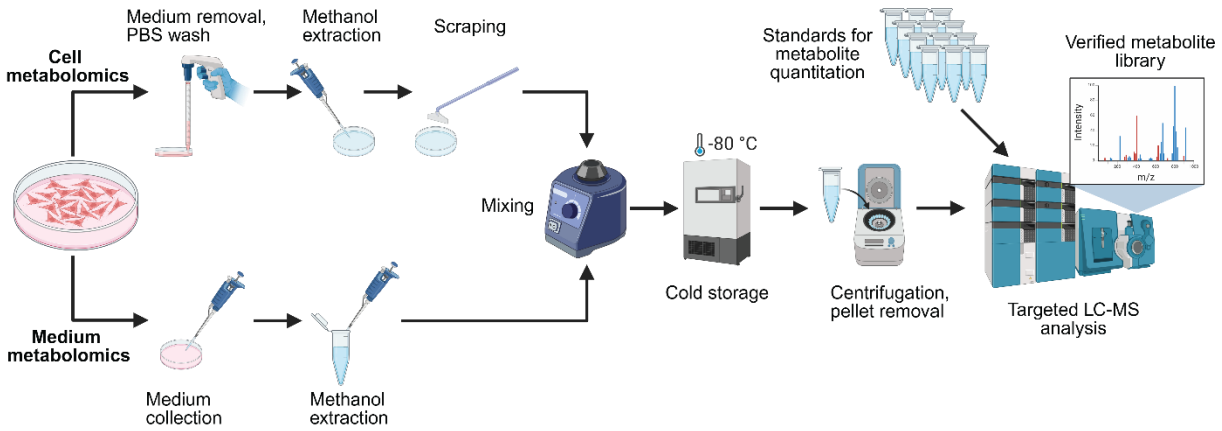


**Figure 3.1: Schematic summary of the procedure for medium and intracellular metabolite extraction and targeted LC-MS metabolomics analysis.**

Analytes identified by their specific mass-to-charge ratios and chromatographic retention times were quantified by their peak height and area intensity (**Fig. 3.2a**). With both parameters we determined that the analyte signal intensity and known concentration of each standard solution were linearly correlated with each other and could be used for quantitation by interpolation inside the concentration window measured (**Fig. 3.2b**). Experimental samples were analyzed in batches, and, during a period of 13 months,

repeated measurements of the same standard solutions remained broadly consistent both in terms of signal intensity of the same standard dilution and of relative difference between different dilutions (**Fig. 3.2c**). Similarly, peak area intensities for acetate, glucose, lactate, and glutamine measured between the first and the last analyses were found to be tightly correlated, indicating that the performance of the method remained comparable throughout the whole period considered (**Fig. 3.2d**). Overall, we find that our metabolomics platform allows us to accurately and consistently identify and quantify key metabolites involved in cancer cell biology.

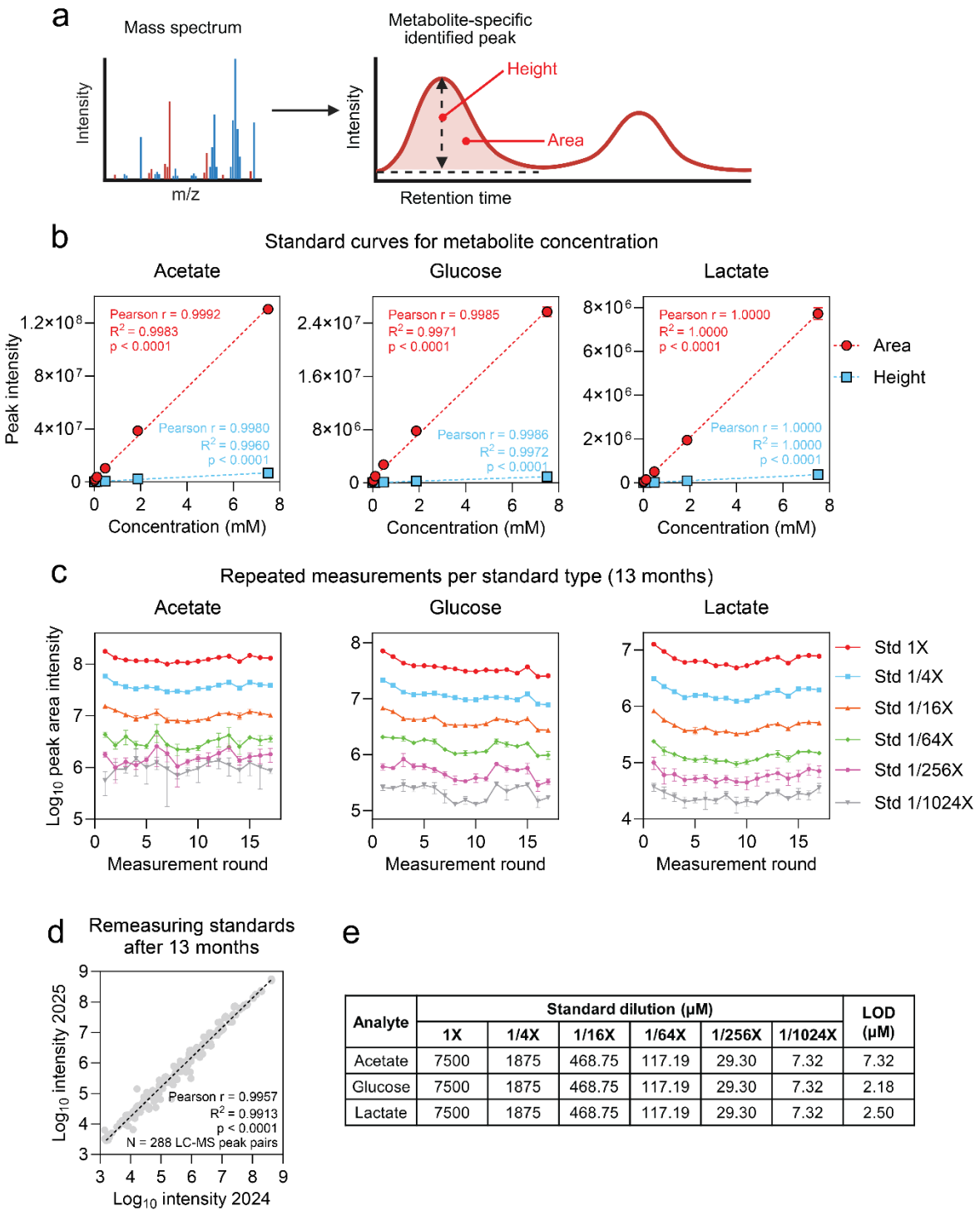


| Analyte | Standard dilution (μM) | | | | | | LOD (μM) |
|---|---|---|---|---|---|---|---|
| | 1X | 1/4X | 1/16X | 1/64X | 1/256X | 1/1024X | |
| Acetate | 7500 | 1875 | 468.75 | 117.19 | 29.30 | 7.32 | 7.32 |
| Glucose | 7500 | 1875 | 468.75 | 117.19 | 29.30 | 7.32 | 2.18 |
| Lactate | 7500 | 1875 | 468.75 | 117.19 | 29.30 | 7.32 | 2.50 |

**Figure 3.2: Our targeted LC-MS metabolomics method is accurate and consistent over a period of 13 months. (a)** Schematic of the process of analyte-peak assignment matching detected fragments with previously annotated mass-to-

charge ratios and chromatographic retention times, followed by peak height and area intensity signal recording. **(b)** Linear correlation between peak height or area intensity and known concentration inside the standard dilutions for acetate, glucose, and lactate. Data points represent means, error bars represent standard deviations ($n$ = 3). Coefficients of correlation (r) and determination ($R^2$) and p-value for Pearson's correlation test are reported. **(c)** Peak area intensities from standard dilutions for acetate, glucose, and lactate in 17 measurement rounds during a 13 months period. Data points represent $\log_{10}$(means), error bars represent standard deviations ($n$ = 3). **(d)** Linear correlation of peak height and area intensities measured for acetate, glucose, lactate, and glutamine between measurement round 1 (2024) and 17 (2025). Data points represent 288 individual peak pairs. Coefficients of correlation (r) and determination ($R^2$) and p-value for Pearson's correlation test are reported. **(e)** Summary table of the concentration of acetate, glucose, and lactate in each standard dilution and of their limit-of-detection (LOD) for the analytic method employed.

### *Acetate import into cells follows a zeroth-order kinetics indicative of active transport*

Active and facilitated membrane transport of a solute across the lipid bilayer of cells is dependent on the availability of transporter sites. Thus, if all sites are engaged by the solute, the mechanism is saturated, and the velocity of transport reaches a maximal value independent of the solute's concentration in a manner similar to that of an enzyme-substrate reaction. In this scenario, the transport rate or flux of the solute through the cell follows a zeroth-order kinetics model. On the other hand, passive diffusion and carrier-mediated transport at low solute concentration follow a first-order kinetics model, which is dependent on the solute's concentration (254) (**Fig.3.3a**).

To confirm that acetate import inside cells is mediated by active transport through one or more transporter proteins, we measured the disappearance of acetate from the medium of cultured COLO800 melanoma cells starting at a concentration of 0.8 mM. This cell model was chosen because our laboratory has previously demonstrated their ability to rapidly

metabolize acetate (151). As expected, we confirm that acetate, similarly to glucose, disappears from the medium following a zeroth-order kinetics model whereby the rate of consumption remains constant even as the concentration in the medium drops by more than 75% in twelve hours (**Fig.3.3b**).

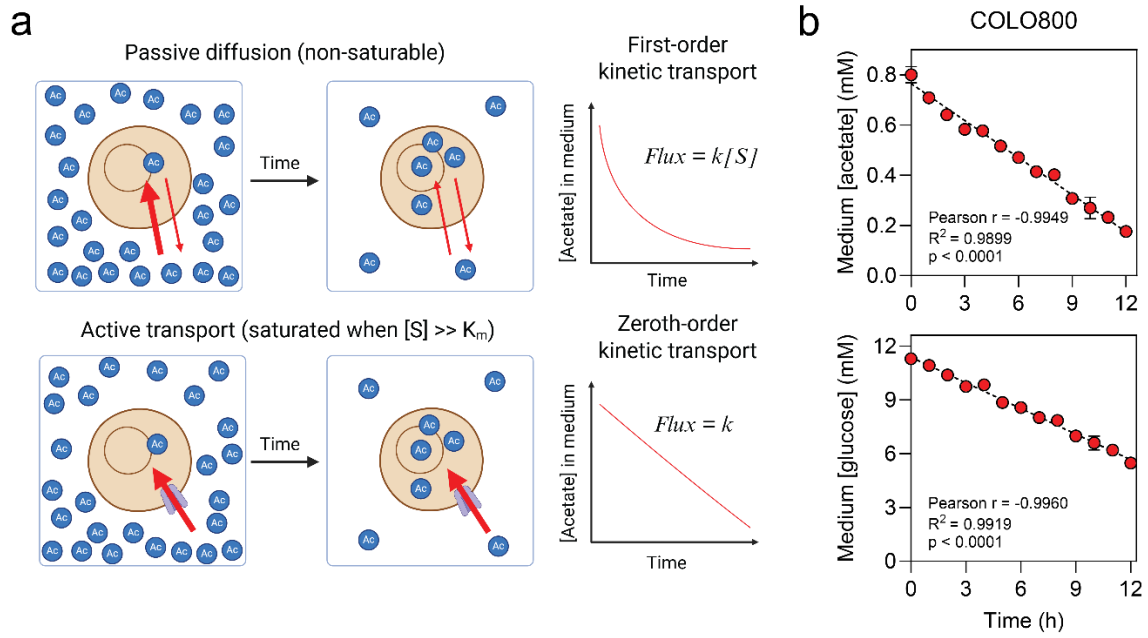


**Figure 3.3: Acetate disappearance from culture medium follows a zeroth-order kinetics model like glucose. (a)** Schematic scenarios comparing the processes of passive diffusion and active carrier-mediated transport of high concentration solutes for acetate. In the case of passive diffusion (top), transport is non-saturable, and transport flux directly depends on the solute's concentration. In the case of active transport at high solute concentration (bottom), the transport mechanism is saturated, and flux is independent from the solute's concentration. [S]: solute concentration; k: solute-specific transport constant; $K_m$: equilibrium constant, i.e. the concentration of solute at which transport rate is half of the maximal rate. **(b)** Acetate (top) and glucose (bottom) concentration (mM) in the medium of cultured COLO800 cells. Data points represent means, error bars represent standard deviations ($n$ = 3). Coefficients of correlation (r) and determination ($R^2$) and p-value for Pearson's correlation test are reported.

*Acetate consumption varies between cancer cell lines and does not correlate with glutamine or glucose consumption*

To better understand the magnitude of acetate utilization in different cancer models, we measured the disappearance of acetate in the medium of 28 cultured human cell lines of various cancer type backgrounds. To account for the different proliferation rates of the various lines during the culture period, we calculated the net flux of metabolite consumption for acetate, glucose, and glutamine. Given that flux is the change in metabolite quantity normalized by the total volume of cells present in culture throughout the time considered, it allows the comparison of net consumption or secretion of metabolites between different cell lines, regardless of their number or the total time of culture for each experiment performed, as long as steady-state metabolic conditions are maintained. (**Fig. 3.4a**). Overall, we find that the magnitude of acetate consumption flux varies both between different cancer types and between cancer lines of the same tissue of origin (**Fig. 3.4c**). For example, the breast cancer cell lines HCC1569, HCC1419 and BT-474 exhibit some of the largest net acetate consumption fluxes among all surveyed cell lines, while another breast cancer model in the form of the MDA-MB-231 cell line shows the lowest net consumption of acetate. In a similar way, the colorectal cancer cell lines HT-55 and HCT116 are again found at the opposite ends of the list, having one of the highest and one of the lowest net consumption fluxes of acetate respectively. For many of the cell lines surveyed, glutamine consumption flux is similar or higher than that of acetate except for four in which, surprisingly, it is significantly lower (breast HCC1419, BT-474, T47D and melanoma WM793), highlighting the role that acetate performs in acting as a carbon source for actively proliferating cancer cells together with glucose and glutamine. Lastly, by comparing the concentration of acetate in the medium at the start and end of experiments where it was not originally added, we find that cell lines not meaningfully consuming acetate, such as the human colorectal cancer HCT116 or the murine triple negative breast cancer B6TAg2.03, readily secrete acetate to concentrations above 100 μM after 24 hours. On the contrary, highly consuming cell lines such as HCC1419 do not appear to secrete any significant amount of acetate after 24 hours and only secrete around 20 μM of acetate after 48 hours,

although, unlike net flux, these concentration measurements are contingent on the specific conditions of each experiment (**Fig.3.4d**). Overall, these data point to a pattern whereby cell lines capable of metabolizing acetate in large quantities can recycle endogenously derived acetyl moieties derived from protein de-acetylation or acetyl-CoA hydrolysis, while cell lines that have limited acetate-metabolizing capabilities secrete it in the extracellular environment (**Fig.3.4b**).

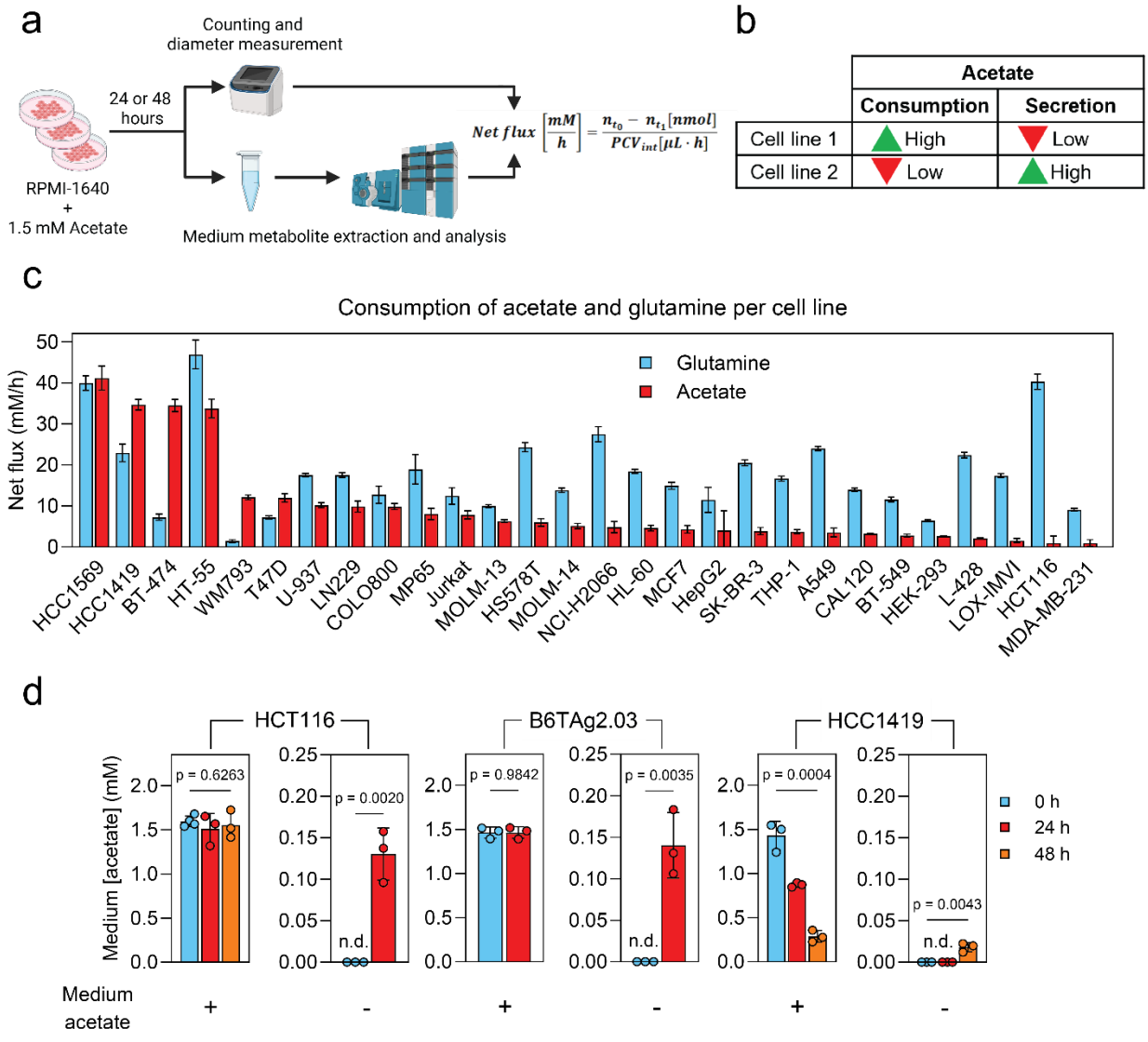


**Figure 3.4: Acetate net consumption varies between cancer cell lines is comparable to glutamine net consumption. (a)** Schematic of the experimental procedures for the calculation of cellular metabolite net flux following LC-MS

analysis on SCIEX QTRAP5500 of spent medium. $n_{t0} - n_{t1}$: variation of metabolite quantity during the assay period; $PCV_{int}$: packed cell volume integrated for the duration of the experiment. **(b)** Table summarizing the observation that acetate consumption and secretion are inversely correlated in different cell lines. **(c)** Acetate and glutamine net consumption flux (mM/h) measurements in 28 human cell lines. Cell lines are listed in descending order of acetate net flux. Bar heights represent means, error bars represent standard deviations (*n = 3*). **(d)** Medium acetate concentration in fresh and spent medium of HCT116, B6TAg2.03, and HCC1419 cell lines. "+" denotes experiments in which 1.5 mM acetate was added at the start, "-" denotes experiments in which acetate was not added. "n.d." indicates conditions where acetate was not detected in the medium. Bar heights represent means, error bars represent standard deviations (*n = 3*). P-value for unpaired two-tailed Student's t test is reported.

As expected, while acetate and glutamine net consumption fluxes are mostly found to be between 5 and 40 mM/h, glucose net consumption flux is higher for most cell lines and is found to be between 50 and 150 mM/h. However, the BT-474 cell line is again a unique exception in which glucose net consumption is lower than that of acetate (**Fig.3.5a**). As an indication of overall metabolic activity of the different cell lines, glucose and glutamine net fluxes positively correlate with each other. On the other hand, acetate flux does not correlate with glucose or glutamine flux, suggesting that acetate consumption may be dependent on either the expression of its transporter proteins or of the two acetyl-CoA synthetases ACSS1 and ACSS2, rather than on overall metabolic activity (**Fig.3.5b**).

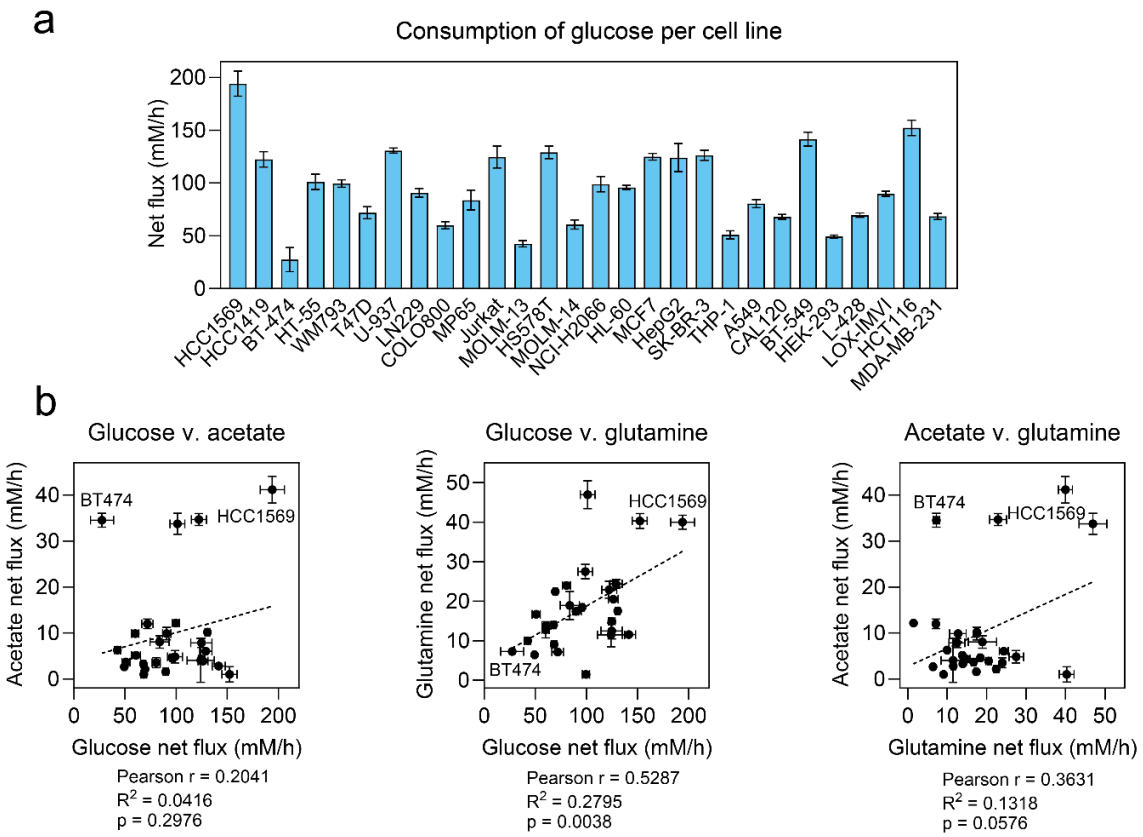


**Figure 3.5: Acetate consumption flux does not correlate with those of glucose or glutamine. (a)** Glucose net consumption flux (mM/h) measurements in 28 human cell lines. Cell lines are listed in descending order of acetate net flux according to the previous figure. Bar heights represent means, error bars represent standard deviations (*n = 3*). **(b)** Linear correlation between glucose and acetate net flux (left), glucose and glutamine net flux (center), and acetate and glutamine net flux (right). Data points represent means, error bars represent standard deviations (*n* = 3). Coefficients of correlation (r) and determination ($R^2$) and p-value for Pearson's correlation test are reported.

*Acetate consumption flux positively correlates with ACSS1 and ACSS2 gene expression*

The enzymes ACSS1 and ACSS2, located in the mitochondrial and nucleocytosolic compartments respectively, are primarily responsible for metabolizing acetate by converting it into acetyl-CoA (**Fig.3.6a**). For this reason, it is not surprising to find that experimentally measured acetate net consumption flux positively correlates with the expression levels of

ACSS1 and ACSS2 based on the data from the Cancer Cell Line Encyclopedia (CCLE) (**Fig.3.6b**). Overexpression of ACSS1, ACSS2 or both in cell lines previously shown to have low acetate consumption flux and low expression of the two enzymes (HEK-293 and LOX-IMVI) indicate that consumption can be influenced by manipulating the expression levels of the two acetate-metabolizing enzymes (**Fig.3.6c, d**). In particular, we find that ACSS1 overexpression has a larger effect on acetate flux than ACSS2, which agrees with similar isotopic labeling results in the literature (151), but was not previously directly described in terms of consumption flux.

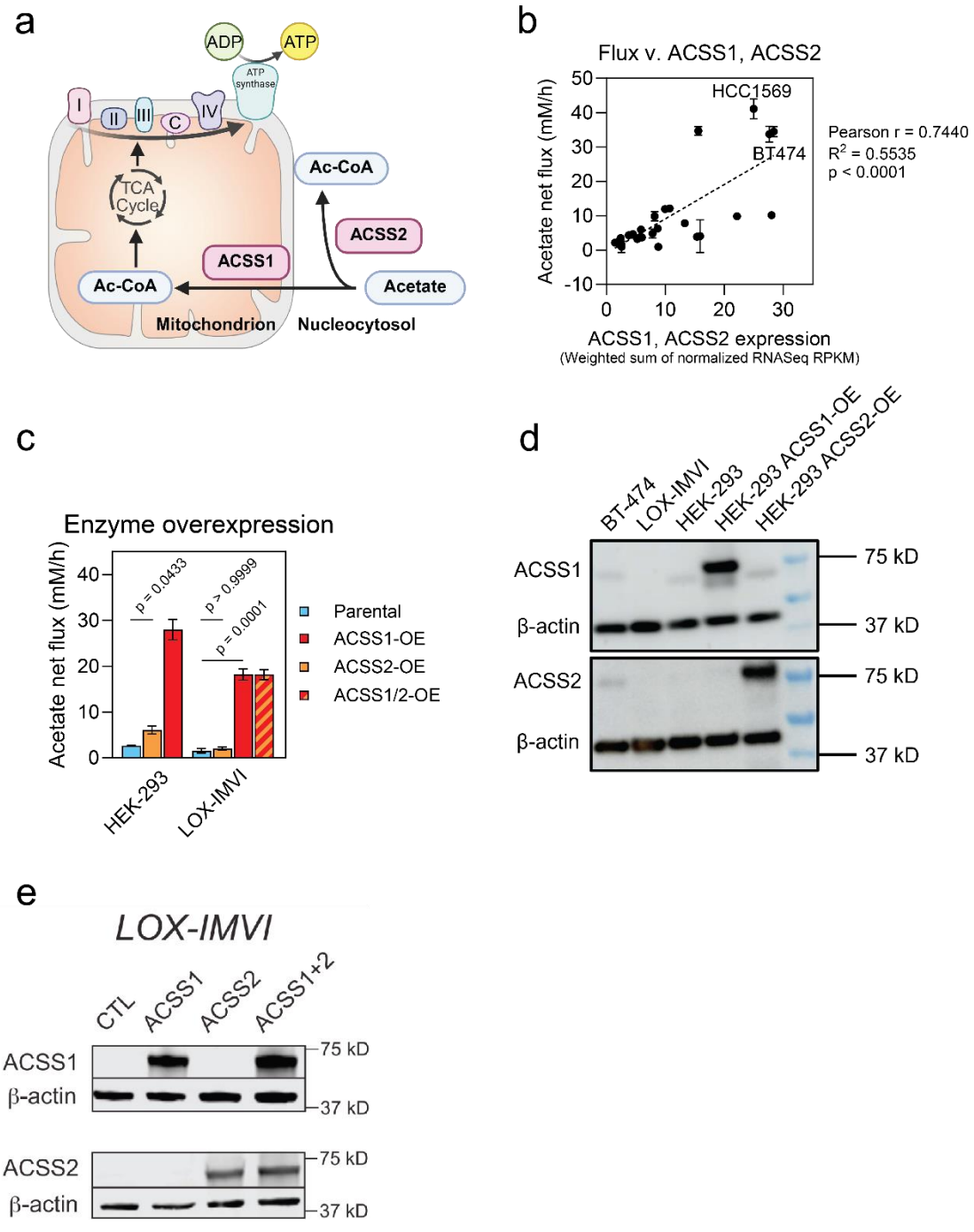


**Figure 3.6: Acetate consumption flux positively correlates with ACSS1 and ACSS2 gene expression. (a)** Schematic of the metabolic pathway for acetate conversion to acetyl-CoA (Ac-CoA) in the mitochondrion and the nucleocytosol, as catalyzed by ACSS1 and ACSS2 respectively. **(b)** Linear correlation between net acetate consumption flux and ACSS1 + ACSS2 combined expression score. The

ACSS1 + ACSS2 combined expression score was calculated as a weighted sum of normalized RPKM values for each cell line as obtained from the Cancer Cell Line Encyclopedia (CCLE 2019). Data points represent means for flux and combined expression scores for each cell line, error bars represent standard deviations ($n$ = 3). Coefficients of correlation (r) and determination ($R^2$) and p-value for Pearson's correlation test are reported. **(c)** Acetate net consumption flux (mM/h) measurements in HEK-293 and LOX-IMVI cells overexpressing the two acetyl-CoA synthetases ACSS1 and ACSS2. Bar heights represent means, error bars represent standard deviations ($n = 3$). P-value for Šídák's multiple comparisons test following one-way ANOVA is reported. **(d)** Immunoblots for ACSS1 (top) and ACSS2 (bottom) protein expression in parental, ACSS1 and ACSS2 overexpressing HEK-293, as well as BT-474 and LOX-IMVI. **(e)** Immunoblots for ACSS1 (top) and ACSS2 (bottom) protein expression in LOX-IMVI parental cell lines and ACSS1, ACSS2 and ACSS1 + ACSS2 overexpression lines. Adapted from Hlavaty, Salcido et al. 2024 (151).

### *The TCA cycle is the primary downstream pathway contributing to acetate consumption*

The main metabolic role of acetate inside the cell is to act as a precursor for the synthesis of acetyl-CoA (125). Due to the inability of acetyl-CoA molecules to directly cross between the mitochondrial and nucleocytosolic compartments, two distinct pools of acetyl-CoA are present inside the cell. Notwithstanding the activity of indirect acetyl-CoA shuttles, each pool has distinct roles, namely supporting the generation of reducing equivalents by fueling the tricarboxylic acid (TCA) cycle in the mitochondrion, and both supporting biosynthesis of fatty acids, cholesterol and acetylated metabolites and direct acetylation of proteins like histones to regulate gene expression and protein activity in the nucleocytosol (**Fig. 3.7a**). The consumption of exogenously provided acetate reflects the different functional roles of the two acetyl-CoA pools. For this reason, we hypothesized that, by selectively blocking metabolic pathways downstream of acetate or acetyl-CoA, it would be possible to separate the contribution of each metabolic function to the overall level of acetate consumption. To do so, we treated BT-474 cells, previously shown to highly express ACSS1 and ACSS2 and to have a high acetate net consumption flux (**Fig.3.6b**), with the following chemical inhibitors:

GSK2194069, an inhibitor of fatty acid biosynthesis targeting the fatty acid synthase (FASN) complex; Fasnall, a Complex I inhibitor previously described as a FASN inhibitor, but recently re-classified by our laboratory as mainly targeting oxidative phosphorylation (OXPHOS) (255); and VY-3-135, a selective ACSS2 inhibitor previously described by our laboratory (124) (**Fig.3.7b**). In agreement with the previous experimental results showing the more prominent role of ACSS1 in determining the magnitude of acetate net consumption, we find that FASN or ACSS2 inhibition reduces overall acetate consumption by less than one third. On the other hand, Complex I inhibition and, upstream of it, shRNA-mediated knockdown (KD) of ACSS1 drastically reduce net acetate consumption, which is completely abolished when ACSS1-KD and inhibition of ACSS2 are combined (**Fig.3.7c**). In contrast to the effects on acetate consumption, inhibition of FASN and ACSS2 do not have significant effects on glucose consumption or lactate secretion, while Fasnall treatment predictably increases the rate of glycolysis (**Fig.3.7d**). Overall, these and previous data show that, in purely quantitative terms, fueling the TCA cycle is the primary metabolic fate of acetate in this breast cancer model cell line, while biosynthesis and acetylation account for between one-third and one-fourth of net consumed acetate.

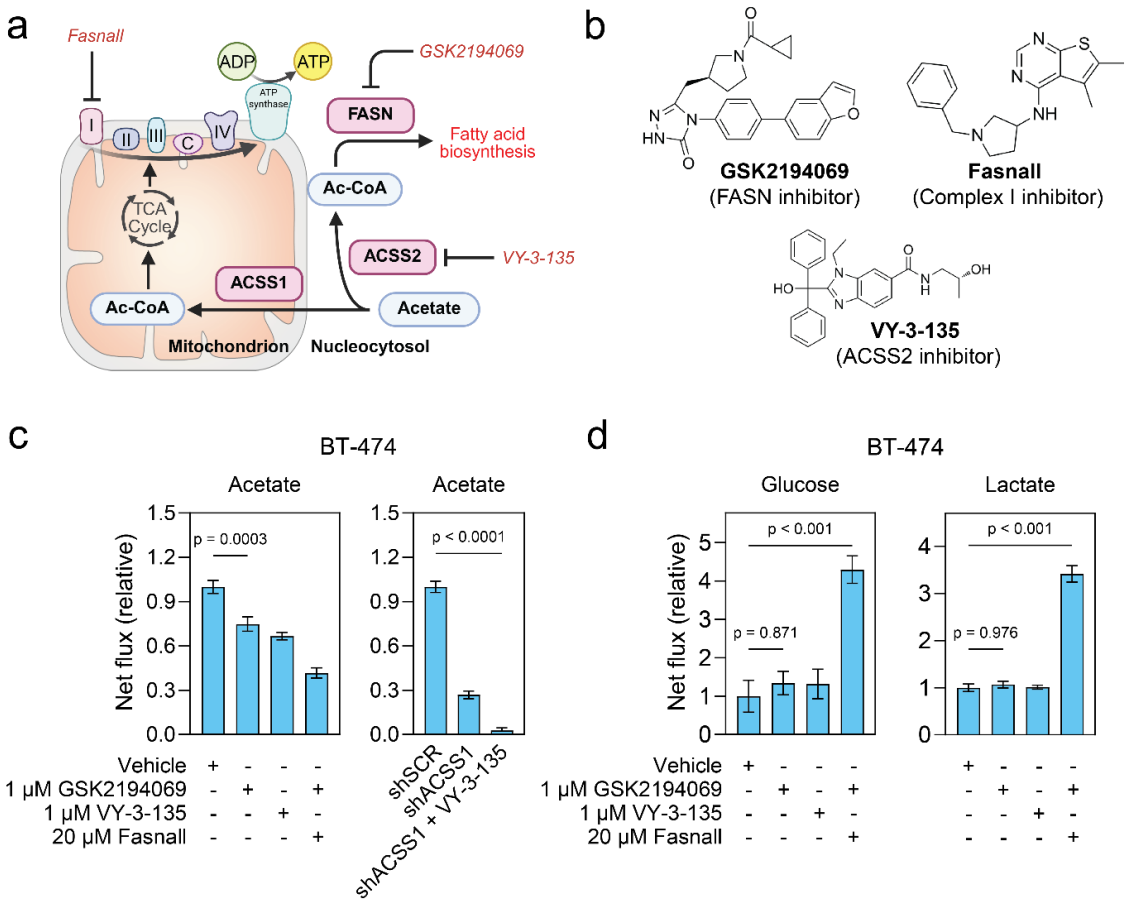


**Figure 3.7: The TCA cycle is the primary downstream pathway contributing to acetate consumption. (a)** Schematic of the activity of inhibitors for Complex I, FASN and ACSS2 in the downstream metabolism of acetate. **(b)** Chemical structures of the GSK2194069, VY-3-135 and Fasnall small molecule inhibitors. **(c)** Acetate net consumption flux relative to vehicle condition after treatment of BT-474 cells with 1 μM GSK2194069, 1 μM VY-3-135 or 1 μM GSK2194069 + 20 μM Fasnall (left). Acetate net consumption flux relative to BT-474 shSCR (scramble) cell line of BT-474 shACSS1 cell line alone or treated with 1 μM VY-3-135 (right). Bar heights represent means, error bars represent standard deviations (*n* = *3*). P-value for Šídák's multiple comparisons test following one-way ANOVA is reported. **(d)** Glucose (left) and lactate (right) net consumption fluxes relative to vehicle condition after treatment of BT-474 cells with 1 μM GSK2194069, 1 μM VY-3-135 or 1 μM

GSK2194069 + 20 μM Fasnall. Bar heights represent means, error bars represent standard deviations (*n = 3*). P-value for Šídák's multiple comparisons test following one-way ANOVA is reported.

### *VY-3-135 selectively inhibits the contribution of acetate to fatty acid biosynthesis mediated by ACSS2*

Previous experimental data reported above have shown that the relative contribution of acetate to fatty acid biosynthesis, while lower than that to the TCA cycle, is still substantial. Since we planned to make use of acetate's role as a fatty acid biosynthetic precursor to identify its transporter proteins (**Chapter 5**), we set out to confirm that our ACSS2 inhibitor of choice (VY-3-135) selectively blocks fatty acid biosynthesis from acetate only while leaving the contribution to nucleocytosolic acetyl-CoA by glucose- and glutamine-derived carbon units through the citrate-malate shuttle intact. To achieve this goal, we performed stable isotopic tracing in BT-474 cells by supplying them with either $^{13}C_6$-glucose, $^{13}C_5$-glutamine, or $^{13}C_2$-acetate and treating them with the ACSS2 inhibitor VY-3-135 (**Fig. 3.8a**). We find that cells incubated with $^{13}C_2$-acetate and treated with VY-3-135 shift their isotopologue distribution of the fatty acid myristic acid from a peak labeled fraction of 12 out of 14 carbons to a peak labeled fraction of 6 out of 14 carbons. We do not observe any ulterior decreasing shift in the isotopologue distribution when the concentration of VY-3-135 treatment is increased 10-fold, indicating that a concentration of 1 μM is sufficient to fully inhibit ACSS2, leaving the remaining labeled fraction due to the activity of ACSS1 and ATP citrate lyase (ACLY) (**Fig.3.8b**). On the other hand, VY-3-135 treatment does not shift the isotopologue distribution of myristic acid from either labeled glucose, glutamine, or a combination of the two (**Fig.3.8c**). Overall, these data indicate that VY-3-135 is a selective inhibitor of ACSS2 that impedes the contribution of acetate to fatty acid biosynthesis mediated by ACSS2 only, while leaving the contribution of acetate mediated by the activity of ACSS1 and the citrate-malate shuttle intact.

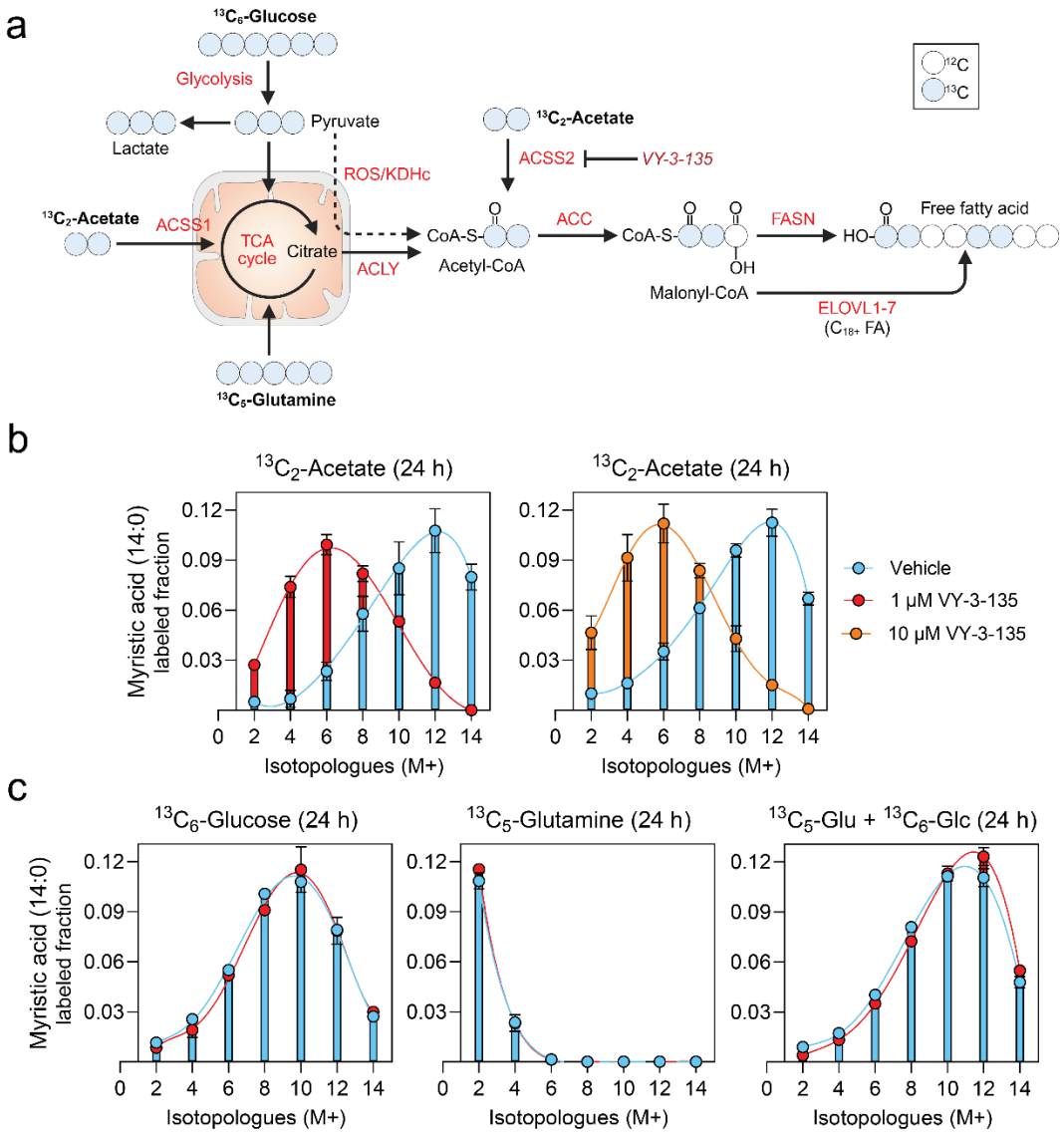


**Figure 3.8: VY-3-135 selectively inhibits the contribution of acetate to fatty acid biosynthesis mediated by ACSS2. (a)** Schematic of the *de novo* fatty acid biosynthesis pathway showing entry points of carbon originating from $^{13}C_6$-glucose, $^{13}C_5$-glutamine, and $^{13}C_2$-acetate and the position of ACSS2 inhibition by VY-3-135 in the pathway. KDHc: ketoacid dehydrogenase complexes; ACLY: ATP citrate lyase; ACC: acetyl-CoA carboxylase; ELOVL; very long chain fatty acid elongases. **(b – c)** isotopologue distribution of relative $^{13}C$ labeled fraction of myristic acid in vehicle and VY-3-135 treated conditions from $^{13}C_2$-acetate **(b)** and $^{13}C_6$-glucose, $^{13}C_5$-

glutamine or both **(c)**. Legend indicating treatment applies to both **(b)** and **(c)**. Data points represent means, error bars represent standard deviations (*n* = 3).

# CHAPTER 4: THE MONOCARBOXYLATE TRANSPORTERS SLC16A1 (MCT1) AND SLC16A3 (MCT4) ARE NOT SOLELY RESPONSIBLE FOR CELLULAR IMPORT OF ACETATE

*Credit for Figure 4.1a,b and Tables 4.1 and 4.2 goes to Dr. Dzmitry Mukha (Thomas Jefferson University).*

## *4.1 Introduction*

Previous literature has primarily ascribed active acetate transport inside cells to the activity of the proton-coupled monocarboxylate transporters MCT1 and MCT4 belonging to the SLC16 family of solute carrier transporters (SLC) (236). While evidence of significant substrate affinity of these transporters for acetate in cell-free systems is available, their role in acetate import in cancer models has not been systematically studied, in favor of a focus on other substrates, primarily lactate and pyruvate (201,206). Moreover, outside of the known tumor suppressor gene SLC5A8, which encodes for the sodium-coupled monocarboxylate transporter 1 (SMCT1), no other monocarboxylate transporter has been investigated in cancer models for its role in acetate transport. In this chapter, we sought to describe the landscape of SLC expression in available cancer cell models and to link transporter mRNA expression profiles with acetate metabolism. We also set out to test the hypothesis that other transporter proteins outside of MCT1 and MCT4 are responsible for acetate import through the plasma membrane.

## *4.2 Results*

### *SLC16A13 and ACSS2 gene expression are positively correlated in cancer*

To understand the landscape of solute carrier transporter (SLC) gene expression in cancer, we analyzed the mRNA expression data for all genes currently classified as SLC available on the Cancer Cell Line Encyclopedia (CCLE) for 1020 cell lines. To be included as an SLC, a gene needed to be present on one of either the SLC list hosted on https://slc.bioparadigms.org/ and curated by Prof. Matthias A. Hediger (University of Bern, Switzerland), the SLC gene group curated by the HUGO Gene Nomenclature Committee, or

the most recent SLC transporter list produced by the RESOLUTE Consortium (Goldmann et al., 2025). Pseudogenes were excluded so that a total of 436 genes were considered. The values of Reads per Kilobase of transcript per Million mapped reads (RPKM) were normalized to limit the spread of the dynamic range caused by very low values (**Fig. 4.1b**). The normalized gene expression levels of each SLC per cell line were tabulated on a heatmap and clustered in an unsupervised manner (**Fig. 4.1a**). By doing so we find that SLC genes can be broadly categorized in three groups depending on their relative expression level: 1) ubiquitously and very highly expressed transporters, 2) ubiquitously and highly expressed transporters and 3) sporadically and lowly expressed transporters. The only member of the SLC16 family found in group 1 is SLC16A1, which encodes for the monocarboxylate 1 (MCT1) transporter. Group 2 includes SLC16A13 (MCT13) and SLC16A3 (MCT4). All other members of the SLC16 family are found in group 3, which also includes SLC5A8, the gene encoding for the sodium-coupled monocarboxylate transporter 1 (SMCT1). Interestingly, a cluster of breast cancer cell lines which include SK-BR-3, T47D, BT-474 and HCC1419 is found to have lower than average expression of SLC16A1, which is of note given their high levels of acetate consumption relative to the panel of cell lines investigated in this study. Similarly, when considering only the 26 human cell lines of the acetate consumption panel for which gene expression data is available on CCLE, the three members of the SLC16 family that are most highly expressed are again SLC16A1, SLC16A3 and SLC16A13, in agreement with the overall trend for all cell lines in CCLE.

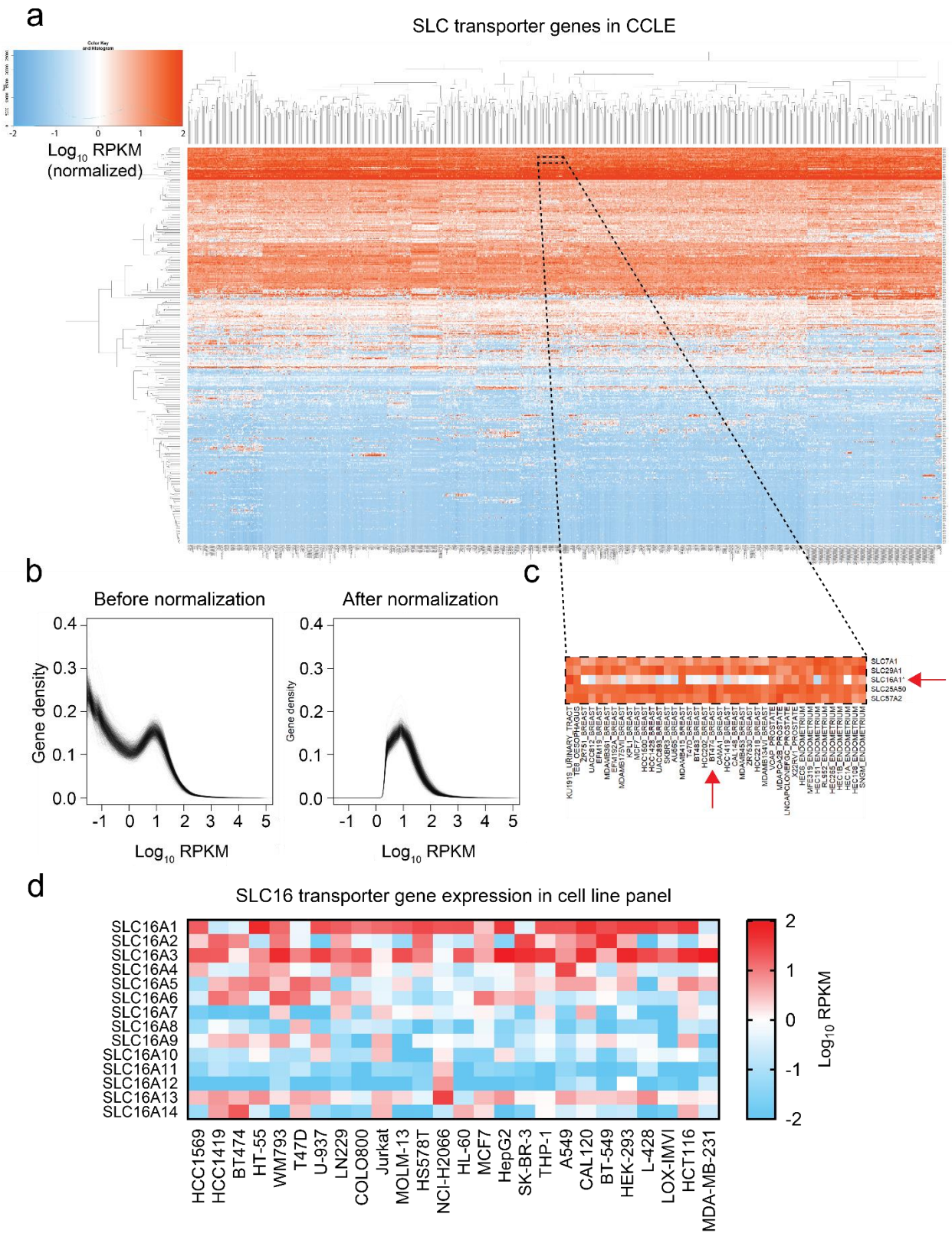
a
SLC transporter genes in CCLE
Log10 RPKM
(normalized)
b
Before normalization
After normalization
Gene density
Log10 RPKM
c
SLC7A1
SLC29A1
SLC16A1
SLC25A50
SLC57A2
d
SLC16 transporter gene expression in cell line panel
SLC16A1
SLC16A2
SLC16A3
SLC16A4
SLC16A5
SLC16A6
SLC16A7
SLC16A8
SLC16A9
SLC16A10
SLC16A11
SLC16A12
SLC16A13
SLC16A14
HCC1569
HCC1419
BT474
HT-55
WM793
T47D
U-937
LN229
COLO800
Jurkat
MOLM-13
HS578T
NCI-H2066
HL-60
MCF7
HepG2
SK-BR-3
THP-1
A549
CAL120
BT-549
HEK-293
L-428
LOX-IMVI
HCT116
MDA-MB-231
Log10 RPKM

**Figure 4.1: SLC16A1, SLC16A3 and SLC16A13 are highly expressed in most cancer cell line models. (a)** Clustered gene expression of 436 SLC genes in 1020 cancer cell lines (CCLE 2019). Each square represents the normalized $\log_{10}$(RPKM) value for a SLC-cell line pair. **(b)** Gene density plots of gene-cell line pairs in CCLE before (left) and after (right) normalization. **(c)** Heatmap inset highlighting a cluster of low SLC16A1 expressing breast cancer cell lines. BT-474 and SLC16A1 are indicated by red arrows. **(d)** SLC16 transporter family gene expression in the human panel of cell lines for which net acetate consumption flux was quantified. Each square represents the normalized $\log_{10}$(RPKM) value for a SLC-cell line pair.

We previously determined that acetate consumption and the expression level of the enzymes ACSS1 and ACSS2 are correlated. Consequently, we hypothesized that the expression levels of potential acetate transporters would also be linked to the presence of acetate-metabolizing enzymes in the various cell lines. To test this, we computed pairwise correlation tests between ACSS1 or ACSS2 individually and either all 436 SLC genes (**Table 4.1**) or only the 14 genes belonging to the SLC16 family (**Table 4.2**). The two separate calculations were performed in order not to obscure potential significant relationships between the two acetyl-CoA synthetases and members of the SLC16 family which could be lost after multiple comparison testing correction when all SLC genes are considered. In this manner, we find that, when all SLC genes are tested, the only gene expression pair that is significantly positively correlated is ACSS2-SLC16A13 (**Fig.4.2a**). Interestingly, the pair ACSS1-SLC16A3 is found to be significantly negatively correlated (**Fig.4.2b**). Positive correlation between ACSS2 and SLC16A1 is significant only if testing is limited to the SLC16 family genes (**Fig.4.2c, Table 4.2**). Overall, these data indicates that MCT1 and MCT4, encoded by SLC16A1 and SLC16A3 respectively, are unlikely to be solely responsible for the transport of acetate across the plasma membrane of different cancer types. Additionally, gene expression data points to a potential link between acetate metabolism and MCT13.

| Gene 1 | Gene 2 | p-value | n. cell lines | Pearson r | q-value |
|---|---|---|---|---|---|
| ACSS2 | SLC35C2 | 7.9924E-16 | 944 | 0.257771361 | 7.2571E-13 |
| ACSS2 | SLC11A2 | 7.5122E-15 | 942 | 0.249393631 | 6.8211E-12 |

| | | | | | |
|---|---|---|---|---|---|
| ACSS2 | SLC50A1 | 9.7801E-15 | 943 | 0.248226539 | 8.8803E-12 |
| ACSS2 | SLC26A6 | 1.5927E-13 | 927 | 0.238910347 | 1.4461E-10 |
| ACSS2 | CLN3 | 4.0706E-13 | 943 | 0.232999882 | 3.6961E-10 |
| ACSS2 | SLC33A2 | 9.9273E-13 | 938 | 0.229790474 | 9.014E-10 |
| ACSS2 | SLC25A1 | 1.8629E-12 | 944 | 0.226352894 | 1.6915E-09 |
| ACSS2 | SLC35D2 | 3.0287E-12 | 812 | 0.241271679 | 2.7501E-09 |
| ACSS2 | SLC49A4 | 3.3394E-11 | 811 | 0.229785997 | 3.0322E-08 |
| ACSS2 | SLC35A3 | 5.8881E-11 | 931 | 0.212164324 | 5.3464E-08 |
| ACSS2 | SLC9A8 | 1.2765E-10 | 883 | 0.213935432 | 1.1591E-07 |
| ACSS2 | SLC31A1 | 1.676E-10 | 943 | 0.20585844 | 1.5218E-07 |
| ACSS1 | SLC35E2B | 4.8357E-10 | 446 | 0.28859877 | 4.3908E-07 |
| ACSS2 | SLC35A2 | 9.4889E-10 | 944 | 0.197210336 | 8.6159E-07 |
| ACSS2 | SLC39A4 | 3.8006E-09 | 769 | 0.210184417 | 3.451E-06 |
| ACSS2 | SLC29A2 | 8.6209E-09 | 708 | 0.213885327 | 7.8278E-06 |
| ACSS2 | SLC22A18 | 2.4955E-08 | 702 | 0.208127777 | 2.2659E-05 |
| ACSS2 | SLC44A2 | 3.1145E-08 | 907 | 0.182290826 | 2.8279E-05 |
| ACSS1 | SLC43A1 | 3.2054E-08 | 294 | 0.314550682 | 2.9105E-05 |
| ACSS2 | SLC55A3 | 3.5927E-08 | 944 | 0.177942344 | 3.2622E-05 |
| ACSS2 | SLC8B1 | 9.0034E-08 | 761 | 0.192040594 | 8.1751E-05 |
| ACSS2 | SLC37A4 | 1.0041E-07 | 931 | 0.173276638 | 9.117E-05 |
| ACSS2 | SLC12A2 | 2.4119E-07 | 896 | 0.171301975 | 0.000219 |
| ACSS2 | SLC12A9 | 2.43E-07 | 937 | 0.167519742 | 0.00022065 |
| ACSS1 | SLC25A42 | 4.345E-07 | 310 | 0.281407986 | 0.00039452 |
| **ACSS2** | **SLC16A13** | **5.5665E-07** | **575** | **0.206585167** | **0.00050544** |
| ACSS2 | SLC20A2 | 6.8116E-07 | 935 | 0.161404219 | 0.00061849 |
| ACSS1 | SLC19A1 | 8.5723E-07 | 420 | 0.236877007 | 0.00077836 |
| ACSS2 | SLC52A2 | 9.7998E-07 | 944 | 0.158374017 | 0.00088982 |
| ACSS1 | SLC25A24 | 2.1921E-06 | 413 | -0.229995514 | 0.00199043 |
| ACSS2 | SLC25A28 | 2.196E-06 | 944 | 0.153224588 | 0.00199394 |
| ACSS1 | SLC39A3 | 2.5259E-06 | 449 | 0.219499354 | 0.00229348 |
| ACSS2 | SLC33A1 | 3.0371E-06 | 916 | 0.153373187 | 0.00275768 |
| ACSS1 | SLC25A38 | 4.0109E-06 | 448 | 0.215398569 | 0.00364186 |
| ACSS2 | SLC1A5 | 5.5302E-06 | 944 | 0.147115141 | 0.00502143 |
| ACSS1 | SLC17A9 | 5.95141E-06 | 239 | 0.287013191 | 0.00540388 |
| ACSS2 | UNC93B1 | 8.17235E-06 | 894 | 0.148400114 | 0.00742049 |
| ACSS1 | SLC25A19 | 8.42015E-06 | 426 | 0.213440701 | 0.007645493 |
| ACSS1 | SLC55A3 | 8.45447E-06 | 450 | 0.207752991 | 0.007676657 |
| **ACSS1** | **SLC16A3** | **9.75364E-06** | **338** | **-0.237286889** | **0.008856307** |

**Table 4.1: Statistically significant pairwise correlations between ACSS1 or ACSS2 and all SLC transporters.** Table summarizing all pairwise correlations

tested between gene expression for ACSS1 or ACSS2 and the 436 SLC genes found to have q-value > 0.01. Gene pairs including members of the SLC16 family are highlighted. The "n. cell lines" column indicates the number of cell lines whose gene expression data were included in the calculation. Cell lines were excluded if normalized RPKM values for at least one of the two genes were equal to 0.01. Coefficient of correlation (r), p-value for Pearson's correlation test and q-value for Benjamini-Hochberg multiple comparisons correction are reported.

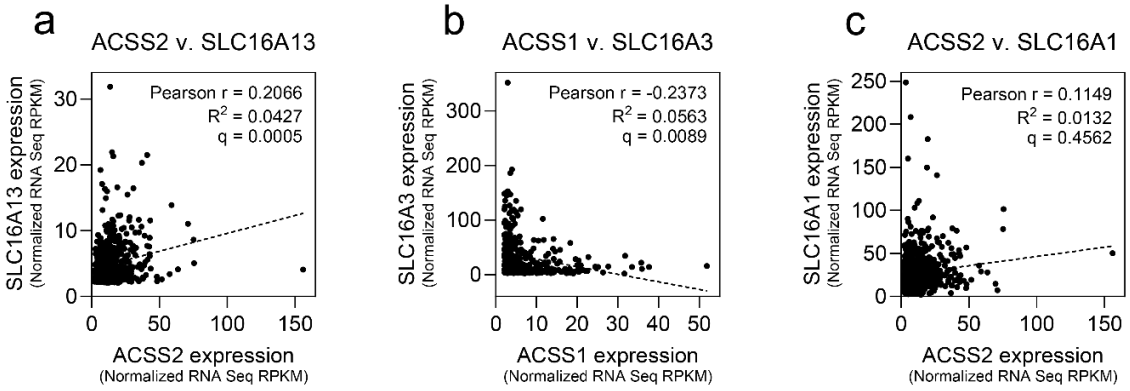


**Figure 4.2: Gene expression levels of ACSS2 and SLC16A13 are correlated in cancer. (a – c).** Linear correlations between gene expression levels for cancer cell lines in CCLE of **(a)** ACSS2 and SLC16A13, **(b)** ACSS1 and SLC16A3 and **(c)** ACSS2 and SLC16A1. Data points represent normalized RPKM of the two genes for each cell line. Coefficients of correlation (r) and determination ($R^2$) and q-value for Benjamini-Hochberg multiple comparisons correction of Pearson's correlation test are reported.

| Gene 1 | Gene 2 | p-value | n. cell lines | Pearson r | q-value |
|---|---|---|---|---|---|
| **ACSS2** | **SLC16A13** | **5.5665E-07** | **575** | **0.20658517** | **1.5586E-05** |
| **ACSS1** | **SLC16A3** | **9.7536E-06** | **338** | **-0.23728689** | **0.0002731** |
| **ACSS2** | **SLC16A1** | **0.00050243** | **912** | **0.11486632** | **0.01406797** |
| ACSS2 | SLC16A11 | 0.00268083 | 6 | 0.89486699 | 0.07506315 |
| ACSS1 | SLC16A8 | 0.00887798 | 16 | 0.59716947 | 0.24858353 |
| ACSS2 | SLC16A5 | 0.0215915 | 494 | 0.10314479 | 0.60456192 |
| ACSS2 | SLC16A4 | 0.02243967 | 328 | 0.12564469 | 0.6283108 |
| ACSS2 | SLC16A2 | 0.60025261 | 462 | 0.02438999 | 1 |
| ACSS2 | SLC16A3 | 0.23281089 | 740 | -0.04385475 | 1 |

| | | | | | |
|---|---|---|---|---|---|
| ACSS2 | SLC16A6 | 0.91165535 | 173 | 0.00844748 | 1 |
| ACSS2 | SLC16A7 | 0.22492439 | 200 | 0.08575901 | 1 |
| ACSS2 | SLC16A8 | 0.35255097 | 30 | -0.16990143 | 1 |
| ACSS2 | SLC16A9 | 0.19616539 | 283 | 0.07678867 | 1 |
| ACSS2 | SLC16A10 | 0.51532668 | 27 | -0.12586152 | 1 |
| ACSS2 | SLC16A12 | 0.09798923 | 44 | 0.24697051 | 1 |
| ACSS2 | SLC16A14 | 0.76878454 | 281 | 0.01755075 | 1 |

**Table 4.2: Pairwise correlations between ACSS1 or ACSS2 and SLC16 family transporters.** Table summarizing all pairwise correlations tested between gene expression for ACSS1 or ACSS2 and the 14 SLC16 family genes. Gene pairs with q-value > 0.05 are highlighted. The "n. cell lines" column indicates the number of cell lines whose gene expression data were included in the calculation. Cell lines were excluded if normalized RPKM values for at least one of the two genes were equal to 0.01. Coefficient of correlation (r), p-value for Pearson's correlation test and q-value for Benjamini-Hochberg multiple comparisons correction are reported.

*Functional inhibition of MCT1 and MCT4 does not abolish acetate import inside cells*

The monocarboxylate transporters 1 (MCT1) and 4 (MCT4) are the most studied members of the SLC16 transporter family, and multiple selective small molecule inhibitors are available to target each one individually (204,256–260). To assess the extent of their role in the import of acetate inside cancer cells, we treated three cell lines previously characterized as having high net acetate consumption flux (HCC1569, HT-55 and BT-474) with AZD3965 and AZD0095, two potent chemical inhibitors that selectively target MCT1 and MCT4 respectively (**Fig.4.3a**). In addition to their high consumption of acetate, these three cell lines were chosen because of their different transporter expression profile. MCT1 and MCT4 are highly expressed by HCC1569 and HT-55 cells, but not by BT-474 (**Fig.4.1d**). Upon inhibition of MCT1 alone, we find that none of the three cell lines exhibit significantly reduced net acetate consumption flux (**Fig. 4.3b, c, d)**. Inhibition of MCT4 alone significantly affects acetate consumption only in HCC1569 cells. Inhibition of both transporters at the same time significantly affects acetate consumption in HCC1569 and HT-55, but not BT-474. MCT1 and MCT4 are primarily described as lactate and pyruvate transporters, so the impact of their

loss of activity on glucose and pyruvate consumption and on lactate secretion was also assessed. We find that MCT1 inhibition only affects the net fluxes of glucose and lactate in HT-55 cells, while MCT4 inhibition affects lactate fluxes in both HCC1569 and BT-474 cells (**Fig. 4.3b, c, d)**. In a similar manner to acetate flux, combined inhibition of MCT1 and MCT4 affects lactate flux in all three cell lines. Predictably, the effect of MCT1 and MCT4 inhibition on glutamine flux was limited, but pyruvate flux was affected in all cell lines and treatments except for MCT4 inhibition alone in HT-55. Overall these data indicate that MCT1 and MCT4 inhibition does not completely abolish net acetate flux through the plasma membrane in the same way that combined inactivation of ACSS1 and ACSS2 does (**Fig.3.7c**). Moreover, the effects of MCT1 and MCT4 inhibition on glucose, lactate and pyruvate metabolism point to a larger rewiring of catabolic metabolism that involves substrates other than acetate.

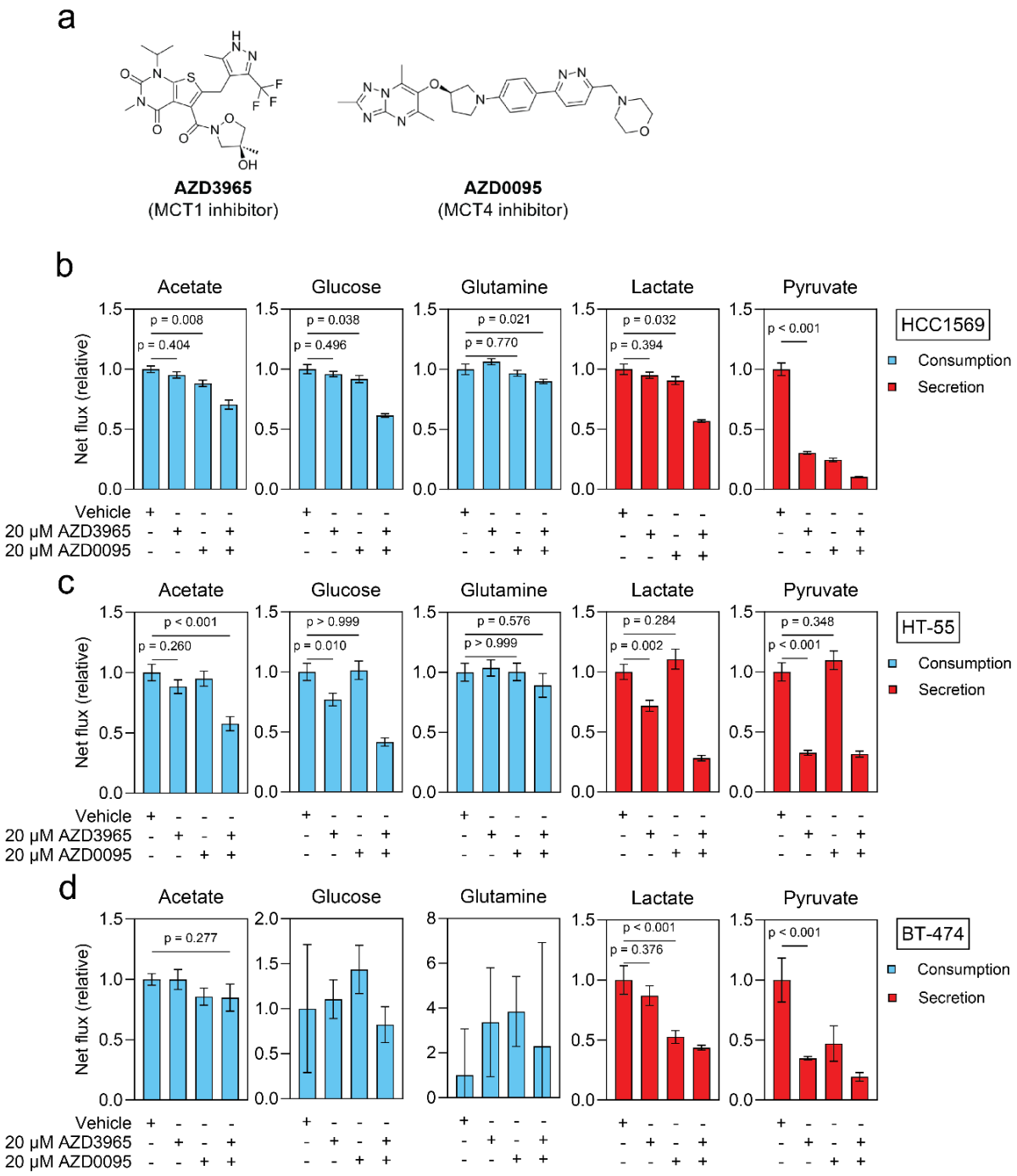


**Figure 4.3: Functional inhibition of MCT1 and MCT4 does not abolish acetate import inside cells. (a)** Chemical structures of the MCT1 inhibitor AZD3965 and MCT4 inhibitor AZD0095. **(b – d)** relative net flux of acetate (first panel to the left), glucose (second panel to the left), glutamine (center), lactate (second panel to the

right) and pyruvate (first panel to the right) for HCC1569 **(b)**, HT-55 **(c)** and BT-474 **(d)** cells treated with 20 μM AZD3965 and AZD0095 alone or in combination. Bar heights represent means, error bars represent standard deviations (*n = 3*). P-value for Šídák's multiple comparisons test following one-way ANOVA is reported.

### *Acidic extracellular pH increases acetate consumption while decreasing lactate secretion*

The transport mechanism of MCT1-4 involves the symport of protons in a 1:1 stoichiometry to the solute. To investigate the role that the concentration of protons in the extracellular environment has on net acetate flux, BT-474 cells were cultured for a short period of three hours in acidic pH conditions. We find that lowering medium pH increases net acetate consumption flux, while at the same time decreasing net lactate secretion flux (**Fig.4.4**) This indicates that the transport mechanisms of these two monocarboxylate species can both be partially influenced by the concentration of protons outside the cell.

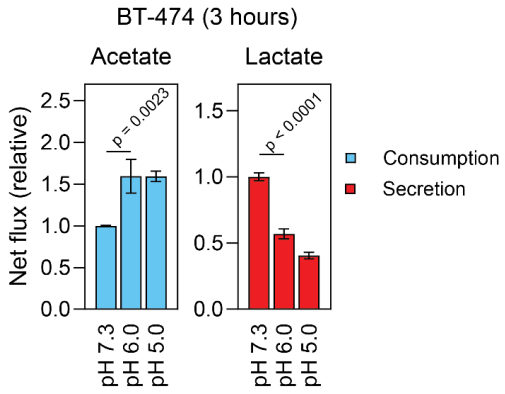


**Figure 4.4: Acidic extracellular pH increases acetate consumption while decreasing lactate secretion.** Relative net flux of acetate consumption (left) and lactate secretion (right) for BT-474 cells cultured for three hours at different medium pH values. Bar heights represent means, error bars represent standard deviations (*n = 3*). P-value for Šídák's multiple comparisons test following one-way ANOVA is reported.

# CHAPTER 5: A CRISPR KO SCREEN HIGHLIGHTING DEPENDENCIES ON ACETATE METABOLISM FOR FATTY ACID BIOSYNTHESIS REVEALS A ROLE FOR SLC16A13 IN ACETATE IMPORT INSIDE CANCER CELLS

*Credit for Figure 5.8a,c goes to Dr. Dzmitry Mukha (Thomas Jefferson University).*

## *5.1 Introduction*

Previous findings in the literature have shown that transporters are often top hits in CRISPR screens (209,261–264), and recently several new transporter functional annotations have been described starting from data obtained through genomic screening (207–210,212,265,266). For this reason, in this chapter we set out to identify conditions that would allow us to perform a CRISPR knockout (KO) screen in order to identify novel putative acetate transporters. To do so, we determine culture conditions in which cells become reliant on acetate for lipid biosynthesis and, ultimately, proliferation. We then use these conditions to find that the monocarboxylate transporter MCT13 is involved in the utilization of acetate by cancer cells.

## *5.2 Results*

### *Resazurin reduction is an accurate and reliable method to assess cell proliferation*

Employing a CRISPR KO screen methodology to identify genes involved in acetate utilization, like transporters, requires the determination of cell culture conditions where proliferation is affected by the presence of acetate and its catabolism. To find suitable culture conditions that would achieve this goal, we decided to employ the conversion of the blue dye resazurin to the pink fluorescent compound resorufin by metabolically active cells as a medium-to-high throughput assay alternative to direct cell counting procedures (267). This assay measures the reduction of cell-membrane permeable resazurin to resorufin by NADH, NADPH, FADH, or other reductive species in the presence of cellular reductases. Thus, it directly reports on metabolic activity while providing an indirect readout on cell number and viability (**Fig.5.1a**) (268). For this reason, it is necessary to properly validate the assay so that

conclusions on cell proliferation capabilities can be drawn accurately and consistently across experiments with different treatments and cell types. To do so we used a cancer cell line model proliferating in suspension, namely the T cell leukemia-derived Jurkat cells, to avoid the necessity of waiting for cell adhesion before metabolic steady state is achieved.

Firstly, we confirmed that resorufin fluorescence and known cell number are linearly correlated (**Fig.5.1b**). Given that average metabolic activity can change between cell lines, absolute cell numbers were never calculated from resorufin signal, and only cell numbers relative to each experiment's internal control condition are reported in experimental results.

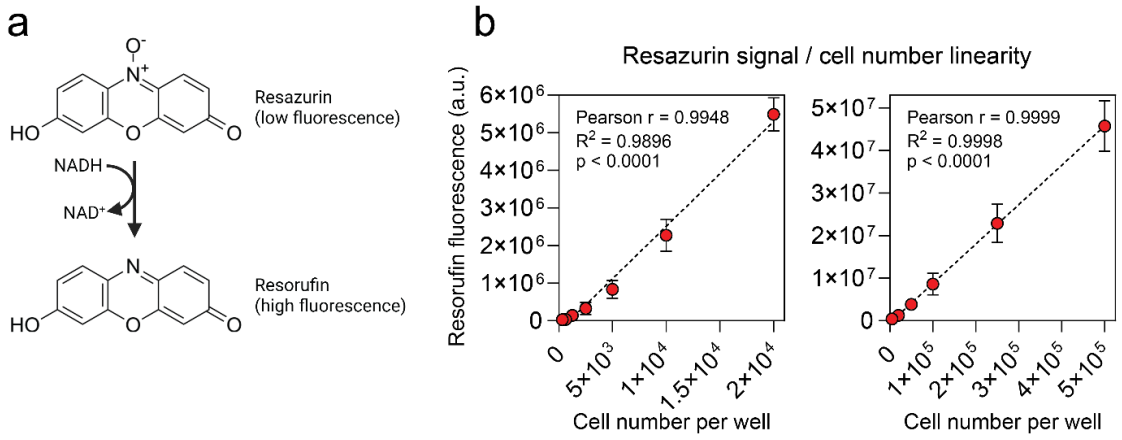


**Figure 5.1: Resazurin reduction to fluorescent resorufin is proportional to cell number. (a)** Schematic of the irreversible reduction of resazurin to resorufin by reducing agents inside metabolically active cells. **(b)** Linear correlation between resorufin fluorescence signal and Jurkat cell number for low (left) and high (right) cell counts. Data points represent mean resorufin fluorescence for each seeded cell number per well, error bars represent standard deviations (*n* = 12). Coefficients of correlation (r) and determination ($R^2$) and p-value for Pearson's correlation test are reported.

Next, as the medium composition can also affect cellular reducing capabilities, we tested the effect of multiple culture conditions inside the short time period used for incubation with resazurin (90 minutes), without any prior treatment that could affect cell number. We find

that in this experimental setup the presence of acetate in the medium has a statistically significant, but very minor effect on resorufin fluorescence signal (**Fig.5.2a**). This is similar for the Complex I inhibitor Fasnall (**Fig. 5.2b**) and the ACSS2 inhibitor VY-3-135 (**Fig. 5.2c**). On the other hand, the absence of glucose or its substitution with galactose greatly affects the readout of resazurin reduction even in this short time window (**Fig.5.2d, e**). Increasing the concentration of glucose three times from that originally present in the medium has no effect on the assay (**Fig. 5.2f**). Compared to glucose absence, adding galactose slightly increases the assay's readout signal (**Fig. 5.2g**). Lastly, the presence of fetal bovine serum (FBS) in dialyzed formulation (dFBS) significantly quenches the fluorescence readout (**Fig. 5.2h**). In light of these results, we decided that we could compare cell treatments following incubation of 24 hours or more only with two key steps added to the protocol: 1) replacement of the spent medium containing the various treatments tested with complete medium supplemented with 10% dFBS when incubating with resazurin for the last 90 minutes, and 2) preparation of separate controls for each individual cell line and treatment. For example, if a condition of interest included the combination of acetate and VY-3-135, the two compounds would also be tested separately every time the combined condition was measured. Lastly, the fluorescence signal intensities of plates coming from different experiments not performed at the same time were never directly compared to each other. Overall, by applying specific design considerations to our protocol, we find that resazurin reduction is an effective methodology to test the effects of variations in culture conditions on cell proliferation.

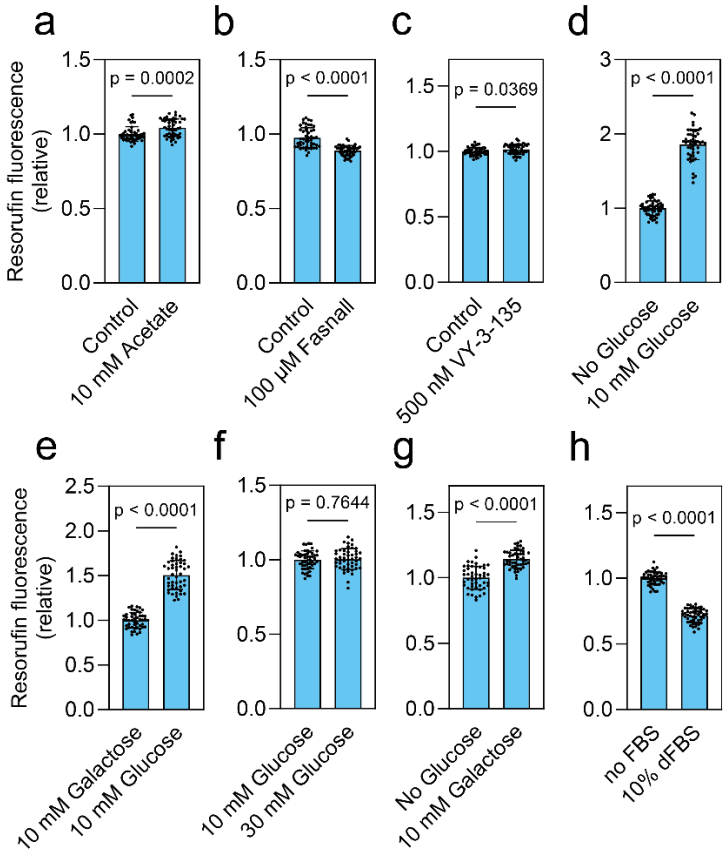


**Figure 5.2: Medium composition during resazurin incubation affects the fluorescence readout. (a – h)** Relative resorufin fluorescence of Jurkat cells incubated for 90 minutes with RPMI 1640 medium containing resazurin and 10 mM acetate **(a),** 100 µM Fasnall **(b)**, 500 nM VY-3-135 **(c)**, no glucose or 10 mM glucose **(d)**, 10 mM galactose or 10 mM glucose **(e)**, 10 mM glucose or 30 mM glucose **(f)**, no glucose or 10 mM galactose **(g)**, and no fetal bovine serum (FBS) or 10% dialyzed FBS (dFBS). For panels **a – g** medium is always supplemented with 10% dFBS. Bar heights represent means, error bars represent standard deviations (*n = 48*). P-value for unpaired two-tailed Student's t test is reported.

*Acetate spares glutamine utilization to extend cell survival in an ACSS1-dependent manner when galactose replaces glucose in the medium*

As previously shown, acetate is among the three most consumed nutrient sources of carbon for cancer cells (**Fig.3.4c, 3.5a**). Given that a majority of the consumption flux of acetate is

due to the activity of ACSS1 as compared to ACSS2 (**Fig.3.6c**), we hypothesized that we could devise culture conditions in which acetate becomes the main source of mitochondrial acetyl-CoA to fuel the TCA cycle. In such an environment, the KO of genes involved in acetate metabolism or transport will be deleterious to cell survival and proliferation, allowing us to distinguish them in a CRISPR KO screen. To do so, we decided to solely direct the conversion of acetate to mitochondrial acetyl-CoA by inhibiting ACSS2 with VY-7-137, a more potent variant of VY-3-135 recently described by our laboratory (151), and to replace glucose in the medium with galactose (**Fig.5.3a**). Galactose is catabolized through a series of four enzymatic reactions collectively known as the Leloir pathway, after which it enters the glycolytic pathway as glucose-6-phosphate (G6P) (269). Kinetically, galactolysis is considerably slower than direct conversion of glucose to G6P (270–272), providing cells with metabolic flexibility at the cost of reduced energy production rates. Additionally, by severely reducing the metabolic flux through glycolysis, galactose replacement forces cells to generate ATP exclusively through OXPHOS, creating a survival dependency on respiration (273,274).

We find that Jurkat cells, which previous results have shown to be among the most glycolytic cell lines used in this study (**Fig.3.5a**), drastically reduce their proliferation rate when cultured in the galactose + VY-7-137 condition (**Fig.5.3b**). Moreover, by starting the experiment at low cell density ($1.25 \cdot 10^5$ cells per mL) and for a period of four days, we do not find that adding acetate has any additional effects on proliferation (**Fig.5.3b**). In contrast, when the galactose + VY-7-137 condition is applied to cells already at high cell density ($2 \cdot 10^6$ cells per mL), we observe that, after three to four days in culture, a majority of the population undergoes a process of cell death and that supplementing acetate reduces the fraction of non-viable cells recorded at the same time point (**Fig.5.3c**). This survival advantage in high cell density with galactose and ACSS2 inhibition is also provided by supplementation of lactate or pyruvate, although the effect of acetate is the strongest (**Fig.5.3d**). Additionally, we confirm that partial shRNA knockdown of ACSS1 (**Fig.5.3e**) significantly reduces the survival advantage provided by acetate (**Fig.5.3d**).

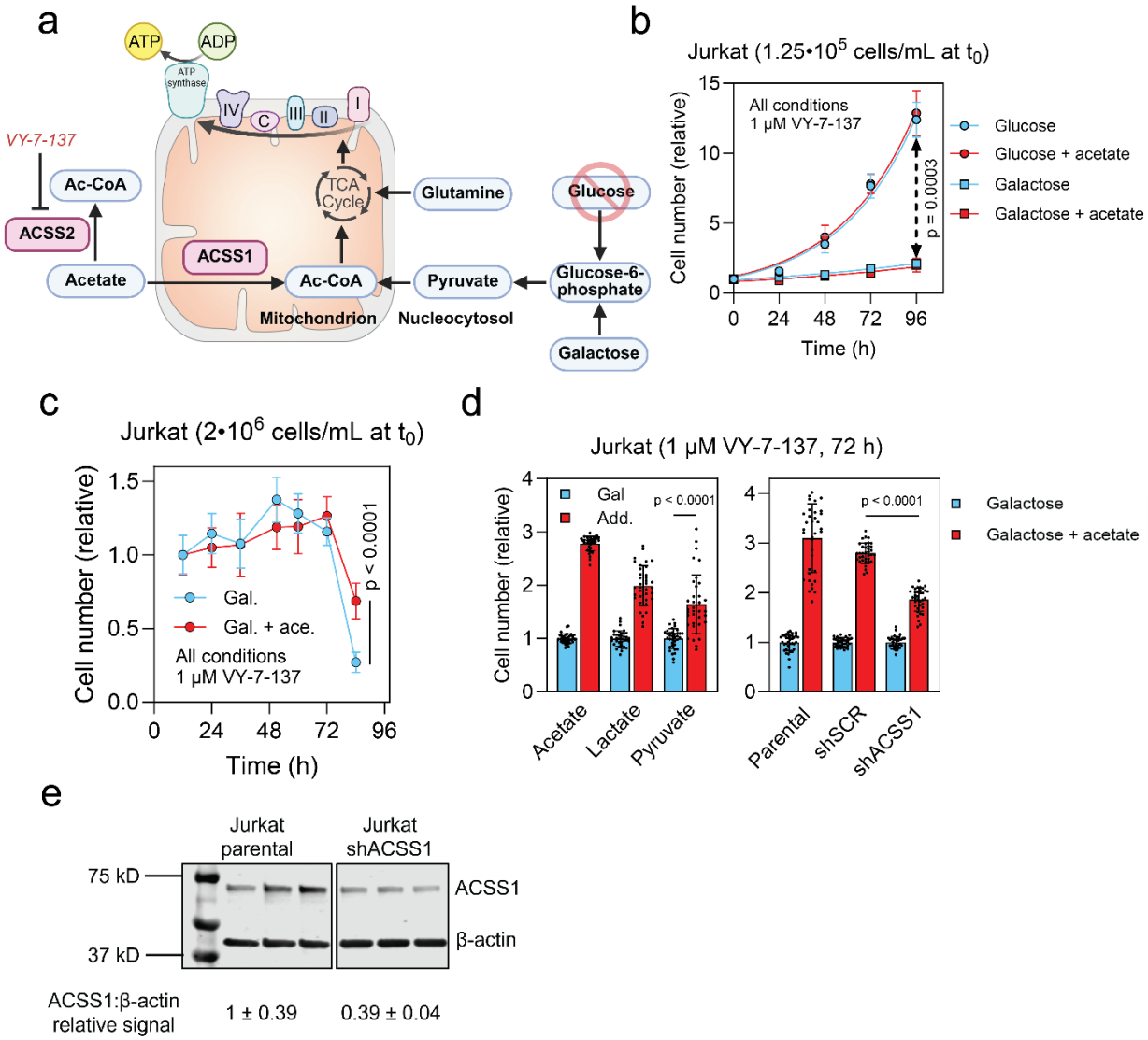


**Figure 5.3: Acetate extends cell survival when glucose is replaced with galactose and ACSS2 is inhibited. (a)** Schematic of the metabolic pathways for the downstream contribution to the TCA cycle of acetate, glucose, galactose, and glutamine, as well as the inhibition of ACSS2 by VY-7-137. Ac-CoA: acetyl-CoA. **(b)** Proliferation of Jurkat cells in 10 mM glucose or 10 mM galactose medium with 1 μM VY-7-137 and 5 mM acetate supplementation. Starting cell density of the experiment is $1.25 \cdot 10^5$ cells per mL of medium. Data points represent means of cell counting, error bars represent standard deviations (*n = 3*). P-value for unpaired two-tailed Student's t test between "Glucose" and "Galactose" conditions is reported. **(c)**

Proliferation of Jurkat cells in 10 mM galactose medium with 1 μM VY-7-137 and 5 mM acetate supplementation. Starting cell density of the experiment is $2 \cdot 10^6$ cells per mL of medium. Data points represent means of resazurin assay measurements per well, error bars represent standard deviations (*n = 20*). P-value for unpaired two-tailed Student's t test is reported. **(d)** Relative number of Jurkat cells in 10 mM galactose medium and 1 μM VY-7-137 after 72 hours in culture. Supplementation of 5 mM acetate, 5 mM lactate, or 5 mM pyruvate (left) and supplementation of 5 mM acetate to parental, shSCR, and shACSS1 Jurkat cells (right). Starting cell density of the experiments is $2 \cdot 10^6$ cells per mL of medium. Bar heights represent means of resazurin assay measurements per well, error bars represent standard deviations (*n = 36*). P-value for Šídák's multiple comparisons test following one-way ANOVA is reported. **(e)** Immunoblot for ACSS1 protein expression in parental and shACSS1 Jurkat cells. Means and standard deviations of relative ACSS1:β-actin expression are reported.

By investigating the metabolism of Jurkat cells cultured with galactose or glucose, we find that the net consumption fluxes for acetate and glutamine are increased when glucose is absent, while the net consumption of galactose itself is drastically lower than that of glucose (**Fig.5.4a**). Similarly, the net secretion fluxes of pyruvate and lactate are almost completely abrogated when galactose substitutes glucose (**Fig.5.4a**). By measuring the relative concentration of intracellular metabolites, we find that, when cultured in galactose medium, supplementation of acetate increases the level of many TCA cycle-associated metabolites and nucleotide biosynthesis precursors, pointing to metabolic adaptations to the presence of acetate in conditions that do not favor rapid cell proliferation (**Fig.5.4b**). As a result of the increased consumption flux of glutamine, we find that when cells are cultured starting from high cell density in galactose, glutamine is completely consumed from the medium by 72 hours after the start of the experiment (**Fig.5.4c**), which coincides with the onset of widespread cell death (**Fig.5.3c**). On the other hand, when acetate is supplemented glutamine remains available in the medium for a longer period of time (**Fig.5.4c**). This reduced rate of glutamine consumption is also observed when pyruvate and lactate are

supplemented to the medium instead of acetate (**Fig.5.4d**). Overall, these data indicate that when cells are made to rely solely on OXPHOS for their energetic needs by the replacement of glucose with galactose, acetate and glutamine become the main nutrient sources fueling the TCA cycle, followed by lactate and pyruvate. Additionally, the rate of glutamine consumption can be slowed by the addition of one of the three other monocarboxylates, and this effect is responsible for delaying cell death that is triggered by the complete disappearance of glutamine from the medium.

While this adaptive metabolic process is useful as a targeted confirmatory assay to assess potential acetate transporter candidates, which if inactivated would stop acetate from sparing glutamine utilization, we ultimately find that it is not amenable to being used for an untargeted CRISPR KO screen setting. This is because the assay relies directly on cell death triggered by absence of glutamine in the medium and only indirectly on the cells' ability to import and metabolize acetate. In other words, in a CRISPR KO setting where only a small fraction of cells would have KO'd genes related to acetate metabolism, most cells would still be able to slow down their own glutamine consumption thanks to their ability to metabolize acetate. This would in turn allow even those few cells incapable of metabolizing acetate to survive the assay, as glutamine would remain available in the medium for all cells regardless of their genetic background, so that their CRISPR guide RNA (gRNA) would not disappear from the population in the way the screen is designed to work. The relationship between a KO'd gene and acetate metabolism can be revealed by this assay only if the whole cell population is homogeneously incapable of metabolizing acetate because of the gene's loss of function (**Fig.5.5**).

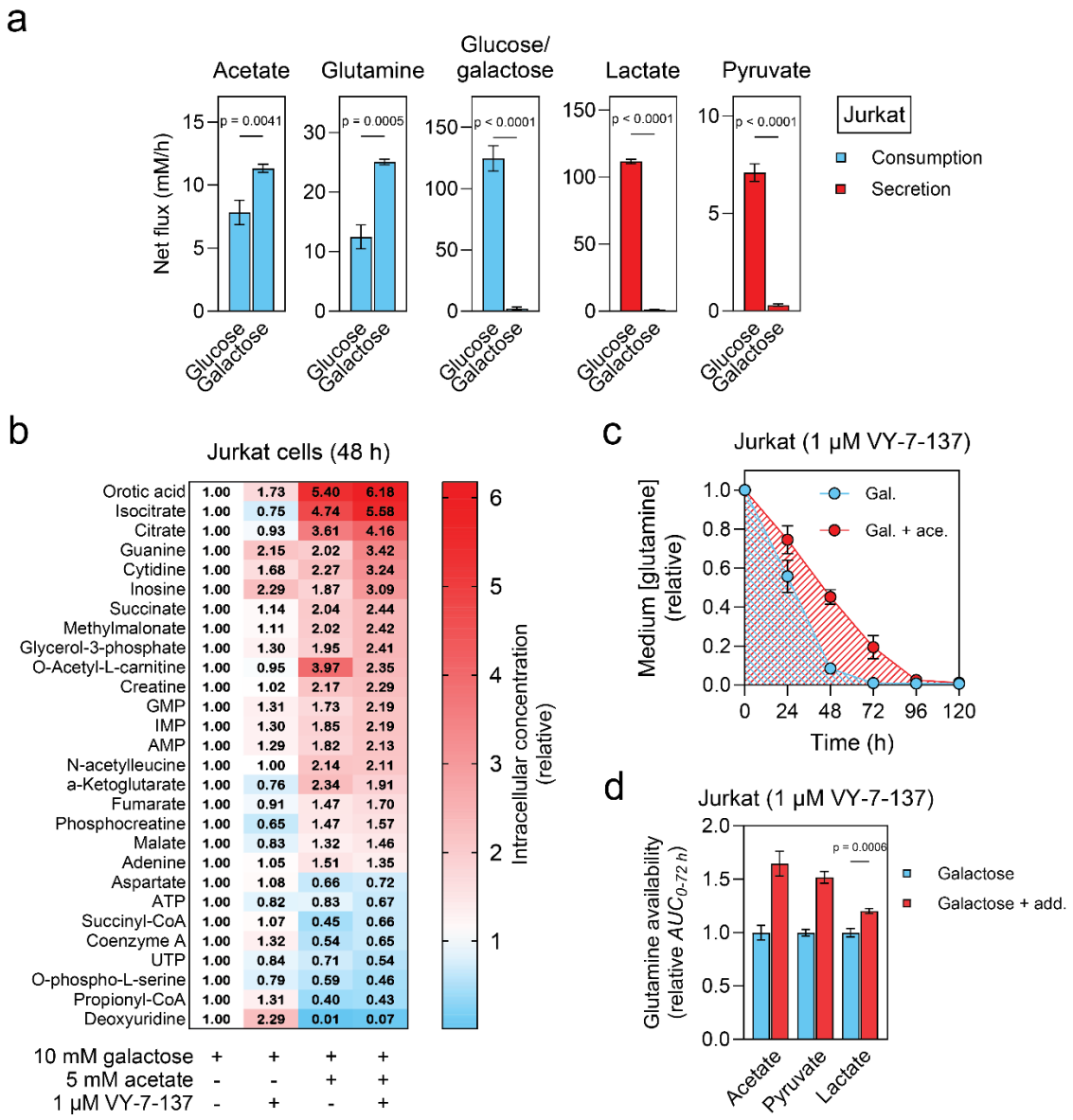


**Figure 5.4: Acetate spares glutamine utilization in an ACSS1-dependent manner when medium glucose is replaced with galactose. (a)** Relative net metabolic flux of acetate, glutamine, and glucose/galactose consumption, as well as lactate and pyruvate secretion of Jurkat cells cultured in 10 mM galactose or 10 mM glucose medium. Bar heights represent means, error bars represent standard deviations (*n = 3*). P-value for unpaired two-tailed Student's t test is reported. **(b)** Heatmap of relative intracellular metabolite concentration of Jurkat cells cultured for 48 hours in 10 mM galactose medium and treated with 5 mM acetate, 1 µM VY-7-

137, or both. Squares represent means (*n* = *3*). **(c)** Medium glutamine concentration relative to $t_0$ for Jurkat cells cultured in 10 mM galactose + 1 µM VY-7-137 and supplemented with 5 mM acetate. Starting cell density of the experiments is $2 \cdot 10^6$ cells per mL of medium. Data points represent means, error bars represent standard deviations. Area-under-the-curve (AUC) is highlighted for the two conditions. **(d)** Glutamine availability in the medium as AUC between $t_0$ and 72 hours of culture of Jurkat cells in 10 mM galactose + 1 µM VY-7-137 and supplemented with either 5 mM acetate, 5 mM pyruvate, or 5 mM lactate. P-value for Šídák's multiple comparisons test following one-way ANOVA is reported.

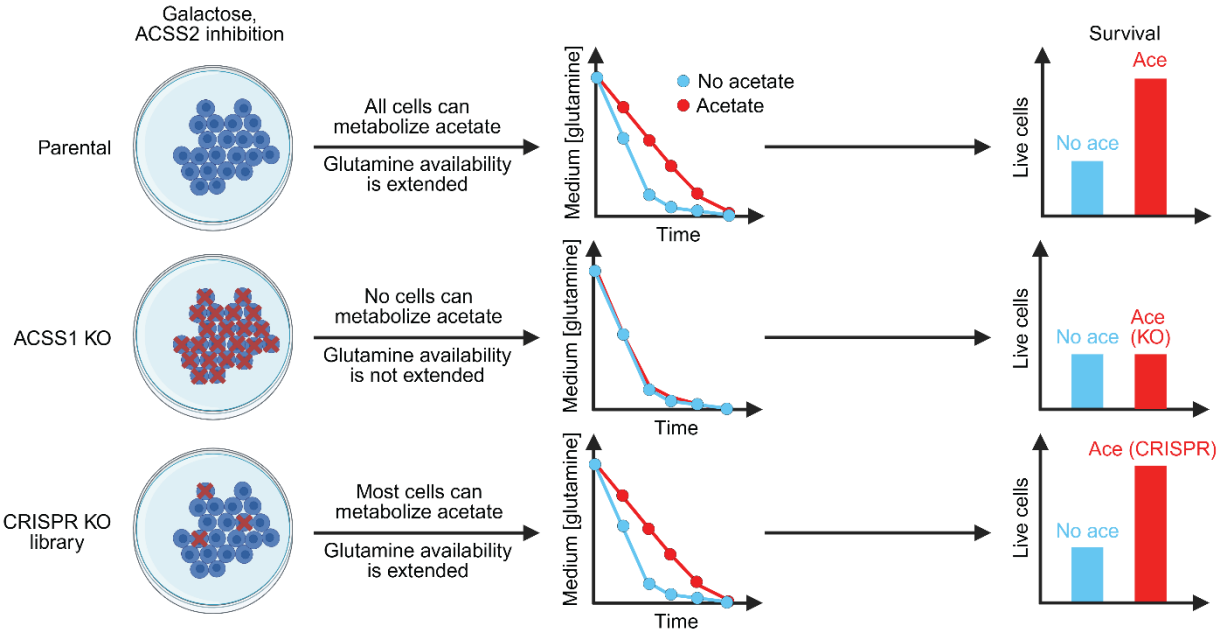


**Figure 5.5: The galactose-acetate survival assay cannot be used in an untargeted CRISPR KO screen.** Schematic of the three hypothetical types of cell populations that could be used in the galactose-acetate survival assay (parental, ACSS1-KO or CRISPR KO library-infected) and the results of presence or absence of acetate on medium glutamine concentration and cell number.

### *Lipid-depletion from culture medium renders cancer cells dependent on de novo fatty acid biosynthesis for proliferation*

Since the ACSS1-based assay intended to improve survival and proliferation of cells capable of metabolizing acetate instead proved effective as a potential targeted approach to be used after acetate transporter genes have already been identified (**Fig.5.5**), we hypothesized that we could use acetate's role as a precursor of nucleocytosolic acetyl-CoA to develop an untargeted approach viable for a CRISPR KO screen. In this case, we sought to position acetate as the main nutrient source for *de novo* fatty acid biosynthesis, while cutting off most alternative sources of fatty acids, endogenous and exogenous. Cancer cells are known to rely on fatty acids for both the biosynthesis of complex lipids and for energy production, and to switch from acquiring extracellular fatty acids to upregulate *de novo* synthesis depending on their surrounding environment and proliferative needs (275–277). As such, we reasoned that a dual strategy of 1) removing available fatty acids from the culture medium and 2) blocking the activity of ATP citrate lyase (ACLY), which is the enzyme mainly, though not solely (278), responsible for indirectly allowing glucose-derived acetyl-CoA in the mitochondria to cross into the nucleocytosolic compartment and contribute to fatty acid biosynthesis (**Fig.5.6**) (125,279), could render cancer cells directly dependent on acetate metabolism for their proliferation. This hypothesis was based on previous studies showing that inactivation of ACLY leads to upregulation of ACSS2 and to partial rescue of lipogenesis and histone acetylation by acetate catabolism, both *in vitro* (280) and *in vivo* (281).

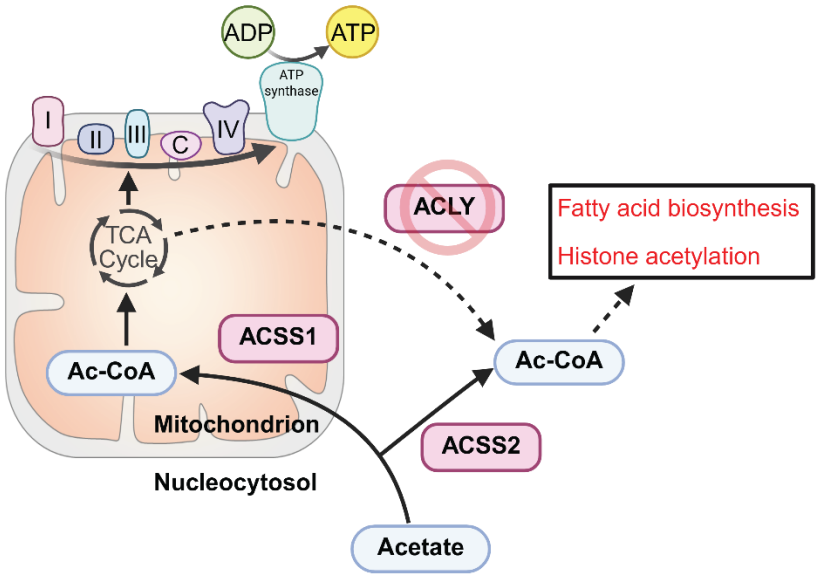


**Figure 5.6: Acetate contributes to both the mitochondrial and the nucleocytosolic acetyl-CoA pools, and ACLY links mitochondrial acetyl-CoA to cytosolic biosynthetic processes.** Schematic of the pathways by which acetate is converted into acetyl-CoA (Ac-CoA) in both the mitochondrial and nucleocytosolic compartments. Mitochondrial acetyl-CoA, derived from catabolism of glucose, lipids, amino acids, ketone bodies and acetate (125) can cross into the nucleocytosol by the activity of the citrate-malate shuttle-linked enzyme ATP citrate lyase (ACLY), which cleaves citrate into oxaloacetate and acetyl-CoA in the cytosol, where the latter can be the substrate for *de novo* lipogenesis and acetylation of metabolites and proteins.

Serum, and specifically fetal bovine serum (FBS) is the source of exogenous lipids primarily used in cell culture (282–284). For this reason, we employed a method of lipid removal based on the use of two organic solvents (di-isopropyl ether and butanol) (243) to produce lipid-depleted dialyzed fetal bovine serum (LD-dFBS) from dialyzed bovine serum (dFBS) while maintaining the growth-sustaining properties of serum proteins intact (**Fig. 5.7a**). We produced two batches of LD-dFBS (batch #1 and batch #2), to test whether one cycle of lipid stripping by the organic solvent mix was sufficient to achieve lipid depletion (LD-dFBS batch #1) or if repeating the procedure twice (LD-dFBS batch #2) would improve the efficiency of

the process. We performed lipidomic analysis by LC-MS on LD-dFBS batch #2 and confirmed that, compared to control dFBS matched for the same production lot number, our lipid-depleted serum contains significantly fewer lipid species both in terms of lipid classes (18 out of 19 are significantly depleted) (**Fig.5.7b**) and individual lipid species (367 out of 387 are significantly depleted) (**Fig.5.7c**).

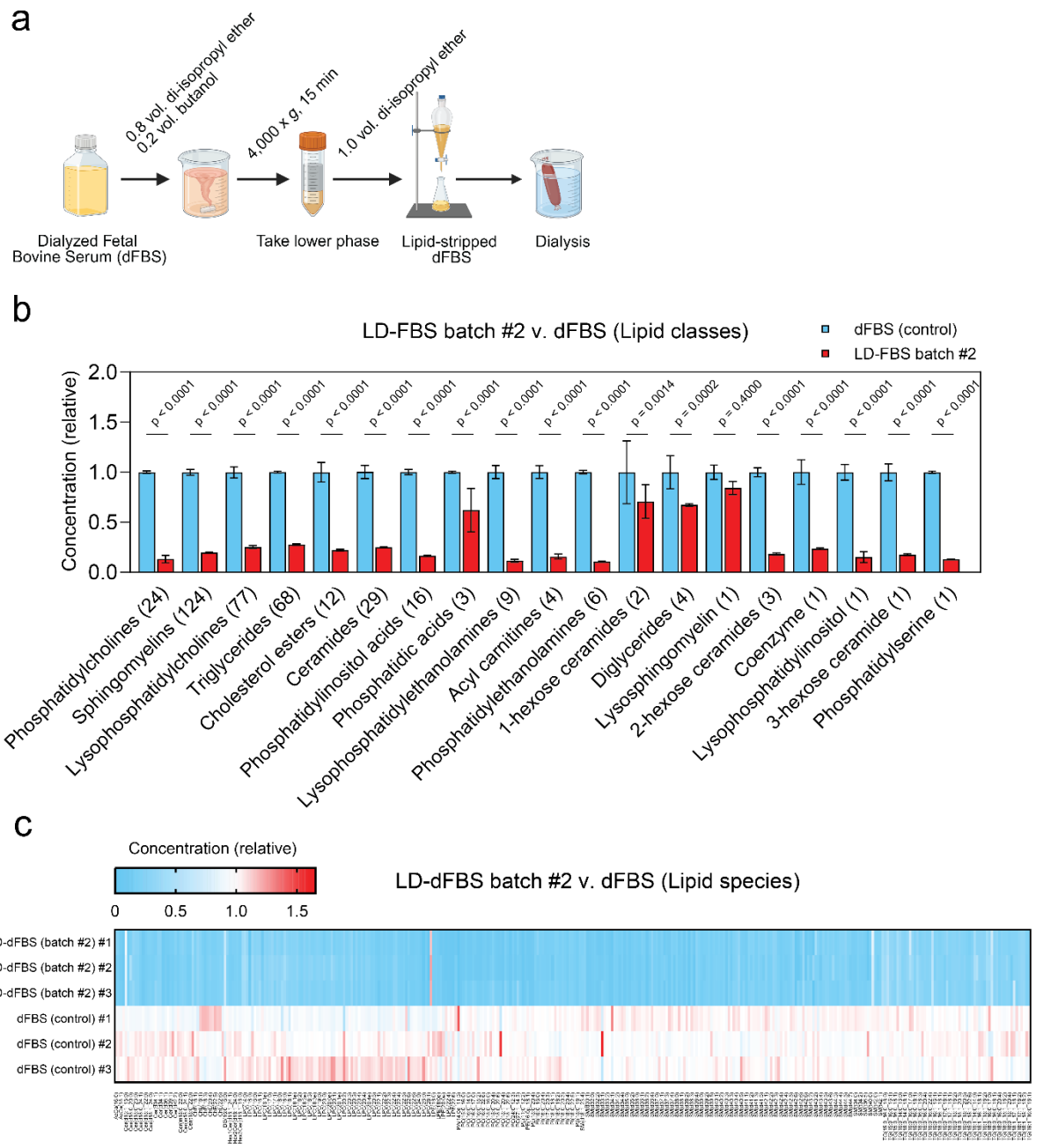

**Figure 5.7: Fetal bovine serum is effectively stripped of lipid species by an organic solvents-mediated extraction. (a)** Schematic of the process of lipid stripping by di-isopropyl ether and butanol extraction, followed by dialysis of the resulting LD-dFBS batches. For LD-dFBS batch #1, the first three steps pictured were performed only once, while for LD-dFBS batch #2 they were repeated twice. **(b)** Relative concentration of lipid classes in dFBS and LD-dFBS batch #2. Bar heights represent means of summed peak intensities for all lipid species belonging to the same class, error bars represent standard deviations (*n = 3*). P-value for unpaired two-tailed Student's t test is reported. **(c)** Relative concentration of lipid species in dFBS and LD-dFBS batch #2. Each square represents a single peak intensity measurement pairing a sample replicate with one of 387 lipid species. Concentrations are normalized on the average peak intensity for each lipid species in dFBS.

Once we confirmed that lipid species were removed from the serum by our method, we asked whether the total content of fatty acids in our LD-dFBS batches # 1 and #2 was comparable to that of commercially available lipid-depleted sera (LD-FBS). We selected three representative commercial LD-FBS, one from Cocalico Biologicals (Cocalico LD-FBS), one from Hyclone (Hyclone LD-FBS) and one from PurMa Biologics (PurMa LD-FBS). For the serum from PurMa we also tested the matching non-lipid-depleted serum from the same company (PurMa-FBS) as a control for the starting content of fatty acids. We performed free fatty acid content analysis by LC-MS and found that when the different sera were clustered in an unguided manner solely by their fatty acid content, the sera with the least fatty acid content were LD-dFBS batch #2, Cocalico LD-FBS and LD-dFBS batch #1 (**Fig.5.8a**). On the other hand, we found that the fatty acid content of Hyclone LD-FBS was not different from control dFBS for many fatty acid species (**Fig.5.8a**). PurMa LD-FBS had significantly reduced fatty acid species compared to dFBS in most cases, but we found that the starting serum from which PurMa LD-FBS derives (PurMa-FBS) contains a higher quantity of many fatty acids compared to dFBS, such as some of the most common biologically-derived fatty acids like stearic, palmitic, oleic, myristic, and linoleic, as well as some that are not normally found

in the other sera, such as the branched-chain fatty acids phytanic and pristanic (**Fig. 5.8 a, b**). Despite a similar level of fatty acid depletion between our two batches of LD-dFBS and the Cocalico LD-FBS, we found that cells cultured with medium supplemented with the latter commercial option presented proliferative responses that were not consistent with our hypotheses and could not be readily interpreted. In particular, when we tested the previously characterized (285) murine hepatocellular carcinoma cell line D42 with either KO of murine fatty acid synthase (m*Fasn* KO) or re-expression of human FASN from m*Fasn* KO clones (hFASN WT), we found that while our LD-dFBS supplemented medium caused an expected reduction of proliferative capabilities in cells with impaired FASN activity, Cocalico LD-FBS instead boosted cell proliferation for the mutant cell lines (**Fig.5.8c**). We hypothesized that these paradoxical proliferative effects could be due to a different make up of growth factors present in Cocalico LD-FBS compared to our dFBS and LD-dFBS, but we did not investigate further. Overall, these data validate our method for lipid depletion of serum as comparable if not superior to commercially available options. All experiments described for the remainder of this work using lipid-depleted sera were performed using LD-dFBS batch #2, which heretofore is referred to as LD-dFBS.

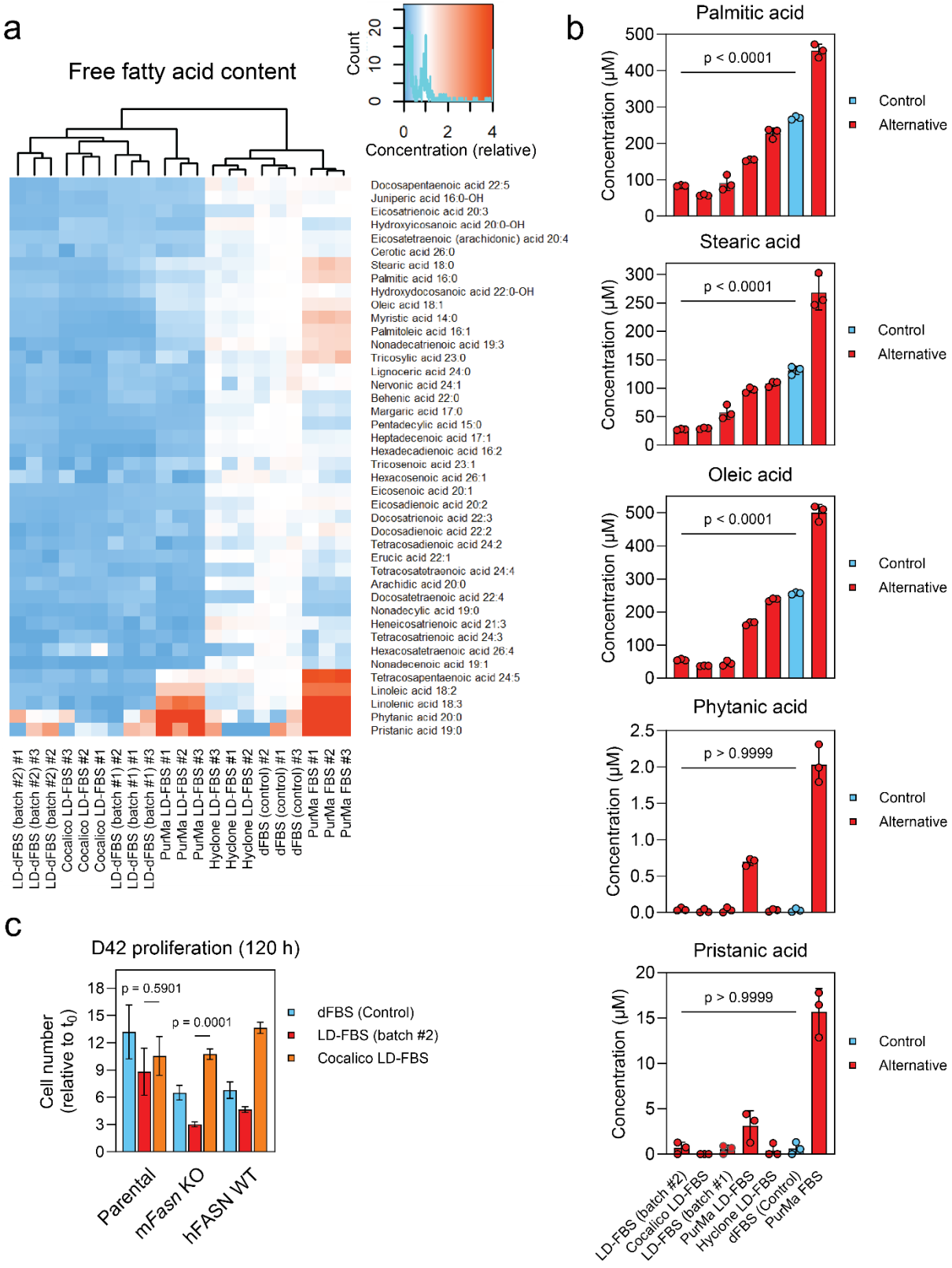
a
Free fatty acid content
Count
0
10
20
0
2
4
Concentration (relative)
Docosapentaenoic acid 22:5
Juniperic acid 16:0-OH
Eicosatrienoic acid 20:3
Hydroxyicosanoic acid 20:0-OH
Eicosatetraenoic (arachidonic) acid 20:4
Cerotic acid 26:0
Stearic acid 18:0
Palmitic acid 16:0
Hydroxydocosanoic acid 22:0-OH
Oleic acid 18:1
Myristic acid 14:0
Palmitoleic acid 16:1
Nonadecatrienoic acid 19:3
Tricosylic acid 23:0
Lignoceric acid 24:0
Nervonic acid 24:1
Behenic acid 22:0
Margaric acid 17:0
Pentadecylic acid 15:0
Heptadecenoic acid 17:1
Hexadecadienoic acid 16:2
Tricosenoic acid 23:1
Hexacosenoic acid 26:1
Eicosenoic acid 20:1
Eicosadienoic acid 20:2
Docosatrienoic acid 22:3
Docosadienoic acid 22:2
Tetracosadienoic acid 24:2
Erucic acid 22:1
Tetracosatetraenoic acid 24:4
Arachidic acid 20:0
Docosatetraenoic acid 22:4
Nonadecylic acid 19:0
Heneicosatrienoic acid 21:3
Tetracosatrienoic acid 24:3
Hexacosatetraenoic acid 26:4
Nonadecenoic acid 19:1
Tetracosapentaenoic acid 24:5
Linoleic acid 18:2
Linolenic acid 18:3
Phytanic acid 20:0
Pristanic acid 19:0
LD-dFBS (batch #2) #1
LD-dFBS (batch #2) #3
LD-dFBS (batch #2) #2
Cocalico LD-FBS #3
Cocalico LD-FBS #2
Cocalico LD-FBS #1
LD-dFBS (batch #1) #2
LD-dFBS (batch #1) #1
LD-dFBS (batch #1) #3
PurMa LD-FBS #1
PurMa LD-FBS #2
PurMa LD-FBS #3
Hyclone LD-FBS #3
Hyclone LD-FBS #1
Hyclone LD-FBS #2
dFBS (control) #2
dFBS (control) #1
dFBS (control) #3
PurMa FBS #1
PurMa FBS #2
PurMa FBS #3
b
Palmitic acid
p < 0.0001
Concentration (μM)
Control
Alternative
Stearic acid
p < 0.0001
Oleic acid
p < 0.0001
Phytanic acid
p > 0.9999
Pristanic acid
p > 0.9999
LD-FBS (batch #2)
Cocalico LD-FBS
LD-FBS (batch #1)
PurMa LD-FBS
Hyclone LD-FBS
dFBS (Control)
PurMa FBS
c
D42 proliferation (120 h)
Cell number (relative to t0)
p = 0.5901
p = 0.0001
dFBS (Control)
LD-FBS (batch #2)
Cocalico LD-FBS
Parental
mFasn KO
hFASN WT

**Figure 5.8: Our LD-dFBS has superior fatty acid depletion when compared to commercially available alternatives. (a)** Relative concentrations of free fatty acids in all sera tested. Each square represents a single peak intensity measurement pairing a sample replicate with one of 42 fatty acid species. Concentrations are normalized on the average peak intensity for each fatty acid species in dFBS. **(b)** Absolute concentrations (μM) of palmitic, stearic, oleic, phytanic, and pristanic acids in all tested sera. Bar heights represent means, error bars represent standard deviations (*n = 3*). P-value for Šídák's multiple comparisons test following one-way ANOVA is reported. **(c)** Relative cell number of D42 parental, m*Fasn* KO, and hFASN WT cells cultured for 120 hours in medium supplemented with either 10% dFBS, LD-dFBS (batch #2) or Cocalico LD-FBS. Bar heights represent means, error bars represent standard deviations (*n = 4*). P-value for Šídák's multiple comparisons test following one-way ANOVA is reported.

To orthogonally test the effect of LD-dFBS on cells unable to synthesize fatty acids endogenously, we treated HEK-293 and Jurkat cells with the FASN inhibitor GSK2194069 and analyzed their proliferation and survival in LD-dFBS (**Fig.5.9a**). We find that while both cell lines are not sensitive to FASN inhibition with regular lipid content, their proliferation is significantly reduced by the inhibitor when the medium is lipid-depleted (**Fig.5.9b**). Additionally, supplementing a chemically defined lipid mixture (LM1) containing 2 μg/ml of arachidonic acid, 10 μg/ml each of linoleic acid, linolenic acid, myristic acid, oleic acid, palmitic acid, and stearic acid and 0.22 mg/ml of cholesterol rescues the inhibition of FASN in lipid-depleted medium (**Fig. 5.9b**). Similarly, when assessing cell death by propidium iodide (PI) staining, we find that FASN inhibition increases the fraction of dead cells only in lipid-depleted conditions, and that LM1 can rescue the phenotype (**Fig.5.9c, d**). Overall, these data show that our LD-dFBS can be used to effectively investigate conditions in which cancer cells are rendered dependent on *de novo* fatty acid biosynthesis.

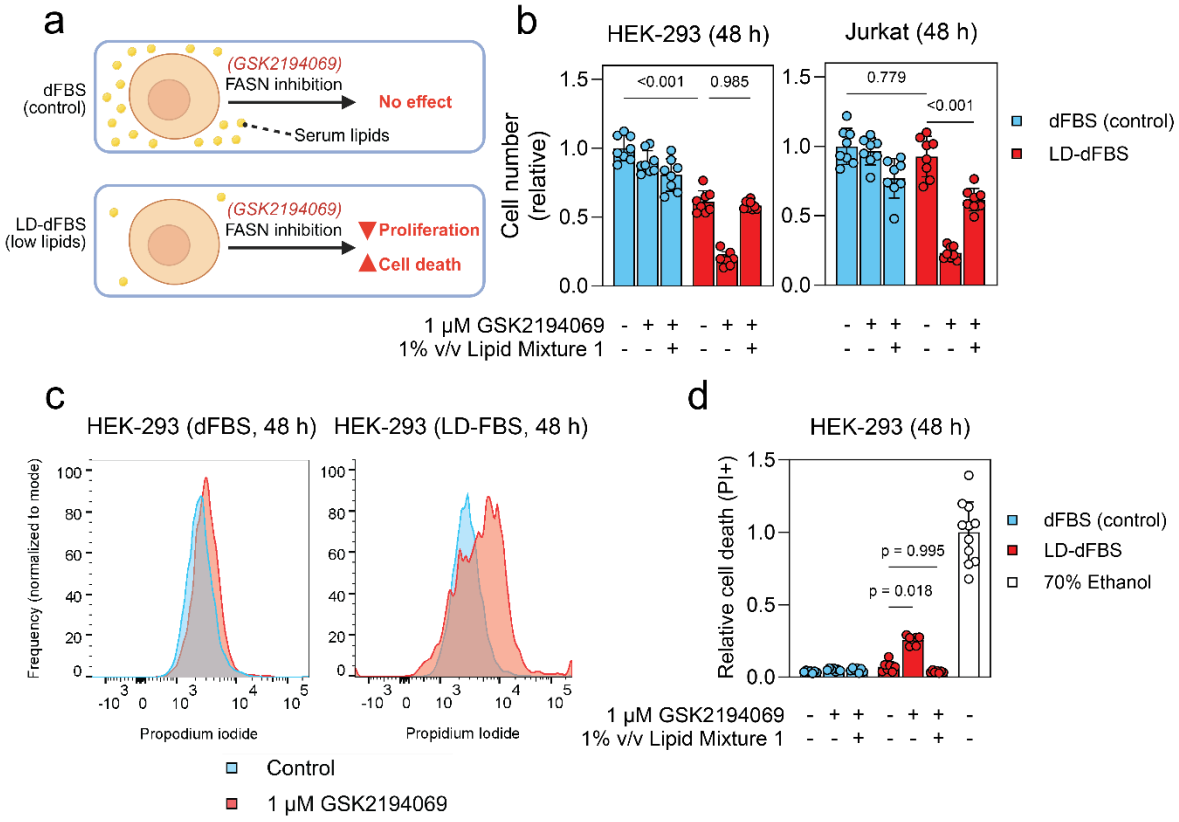


**Figure 5.9: LD-dFBS supplementation to the medium sensitizes cells to FASN inhibition. (a)** Schematic of expected outcomes from FASN inhibition in culture medium supplemented with 10% dFBS (top) or 10% LD-dFBS (bottom). **(b)** Relative number of HEK-293 (left) and Jurkat (right) cells cultured in medium supplemented with 10% dFBS or 10% LD-dFBS and treated with 1 μM GSK2194069 and 1% v/v Lipid Mixture 1 (LM1). Bar heights represent means, error bars represent standard deviations (*n = 8*). P-value for Šídák's multiple comparisons test following one-way ANOVA is reported. **(c)** Normalized frequency of control- and 1 μM GSK2194069-treated HEK-293 cells in dFBS and LD-dFBS medium, stained with propidium iodide (PI) and analyzed by flow cytometry (10,000 events recorded). **(d)** Fraction of non-viable HEK293 cells positive for PI staining in dFBS or LD-dFBS medium, treated with 1 μM GSK2194069 and 1% v/v LM1. Bar heights represent means, error bars represent standard deviations (*n = 7; 70% EtOH negative control n = 11*). P-value for Šídák's multiple comparisons test following one-way ANOVA is reported.

*Exogenous lipid removal and ACLY inactivation render cells dependent on acetate for proliferation*

Having validated our methodology for the removal of exogenous lipids in culture, we then sought to reliably inhibit the activity of ACLY, to then combine the two treatments and make *de novo* fatty acid biosynthesis, and ultimately cell proliferation, dependent on acetate metabolism. For this purpose we validated two previously described small molecule chemical inhibitors of ACLY, namely NDI-091143 (286,287) and BMS-303141 (288,289) (**Fig.5.10b**). We hypothesized that selective ACLY inhibition would provide us with a specific intracellular metabolic signature when either of these two ACLY inhibitors were given to cells concomitantly with the FASN inhibitor GSK2194069 (**Fig.5.10a**). It has been previously reported that FASN inhibition (FASNi) leads to an intracellular accumulation of malonyl-CoA due to the nature of the *de novo* fatty acid biosynthetic pathway (255). When ACLY is also inhibited at the same time, we expected that this upstream blockage of the metabolic pathway would cause a reversal of the FASNi-derived malonyl-CoA accumulation. Indeed, when analyzing the intracellular metabolic content of treated HEK-293 cells, we find that FASN inhibition alone causes a 40-fold intracellular accumulation of malonyl-CoA, which is rescued by both NDI-091143 and BMS-303141, as well as by disrupting mitochondrial metabolism with the Complex I inhibitor Fasnall (**Fig.5.10c**). Overall, these data validated the reported inhibitory activity of these two molecules against ACLY.

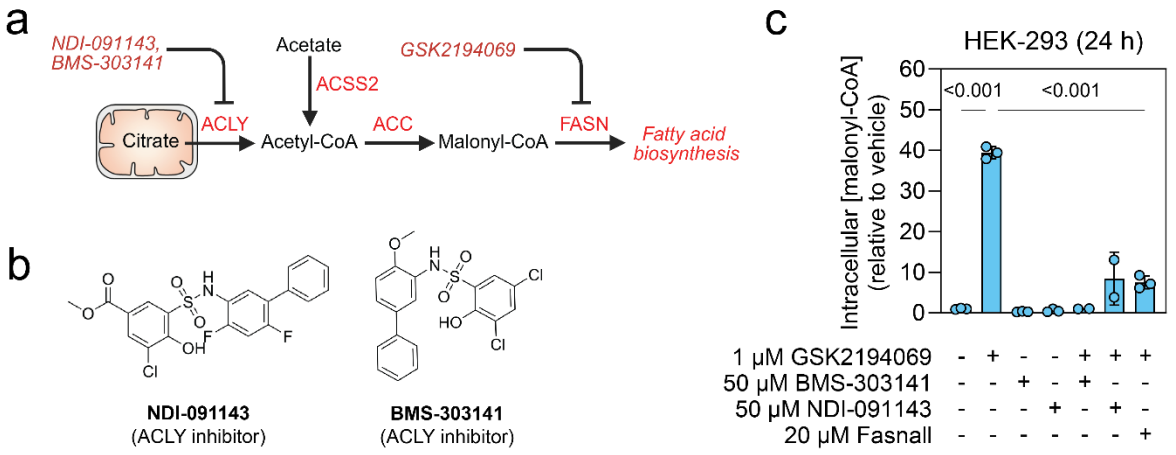

**Figure 5.10: NDI-091143 and BMS-303141 are true inhibitors of ACLY activity. (a)** Schematic of the metabolic pathway that links TCA cycle-derived citrate in the mitochondria and fatty acid biosynthesis in the cytosol. The location of activity of the inhibitors of ACLY and FASN is indicated. **(b)** Chemical structure of the two small molecule inhibitors of ACLY, NDI-091143 and BMS-303141. **(c)** Relative intracellular concentration of malonyl-CoA in HEK-293 cells treated with combinations of 1 μM GSK29104069 and one of either 50 μM NDI-091143, 50 μM BMS-303141, or 20 μM Fasnall. Bar heights represent means, error bars represent standard deviations (*n = 3, except BMS-303141 + GSK2194069 and NDI-091143 + GSK2194069 for which n = 2*). P-value for Šídák's multiple comparisons test following one-way ANOVA is reported.

Following technical validation of the culture conditions that we hypothesized would make cells dependent on acetate metabolism for proliferation, we then sought to test this hypothesis. As expected, we find that acetate does not affect proliferation when cells are cultured in lipid-depleted medium without any additional treatment (**Fig. 5.11a**), as *de novo* fatty biosynthesis is not impaired. On the other hand, acetate rescues impaired proliferation caused by ACLY inhibition when cells are cultured with LD-dFBS, and the magnitude of rescue is stronger in cells overexpressing ACSS2 (**Fig. 5.11b**). Similarly, when testing the dose-response curve of HEK-293 cells to NDI-091143, we find that the $IC_{50}$ concentration of the drug can be increased by acetate, i.e. decreasing the inhibitor's potency, in both lipid-replete and lipid-depleted culture conditions, but that the stronger effect is achieved in HEK-293 ACSS2-OE cells cultured in lipid-depleted medium (**Fig. 5.11c-f**). We confirmed that changes in proliferation and inhibitor sensitivity were not specific to one cell line, tissue, or species of origin, as we replicated the findings in BT-474 (human breast cancer), Jurkat (human T-cell leukemia), and B6TAg2.03 (murine breast cancer) (**Fig.5.12a-d**). For B6TAg2.03, which are characterized by rapid proliferation (doubling time ~13 hours) (**Fig.5.22b**) (290), we find that ACLY inhibition and acetate supplementation in lipid-replete medium is already sufficient to obtain conditions where acetate-metabolizing cells have a large proliferation advantage over cells that cannot metabolize acetate. Additionally

removing lipids is counterproductive to our purposes due to the excessive cytotoxic impact on these highly proliferative cells (**Fig.5.12d**).

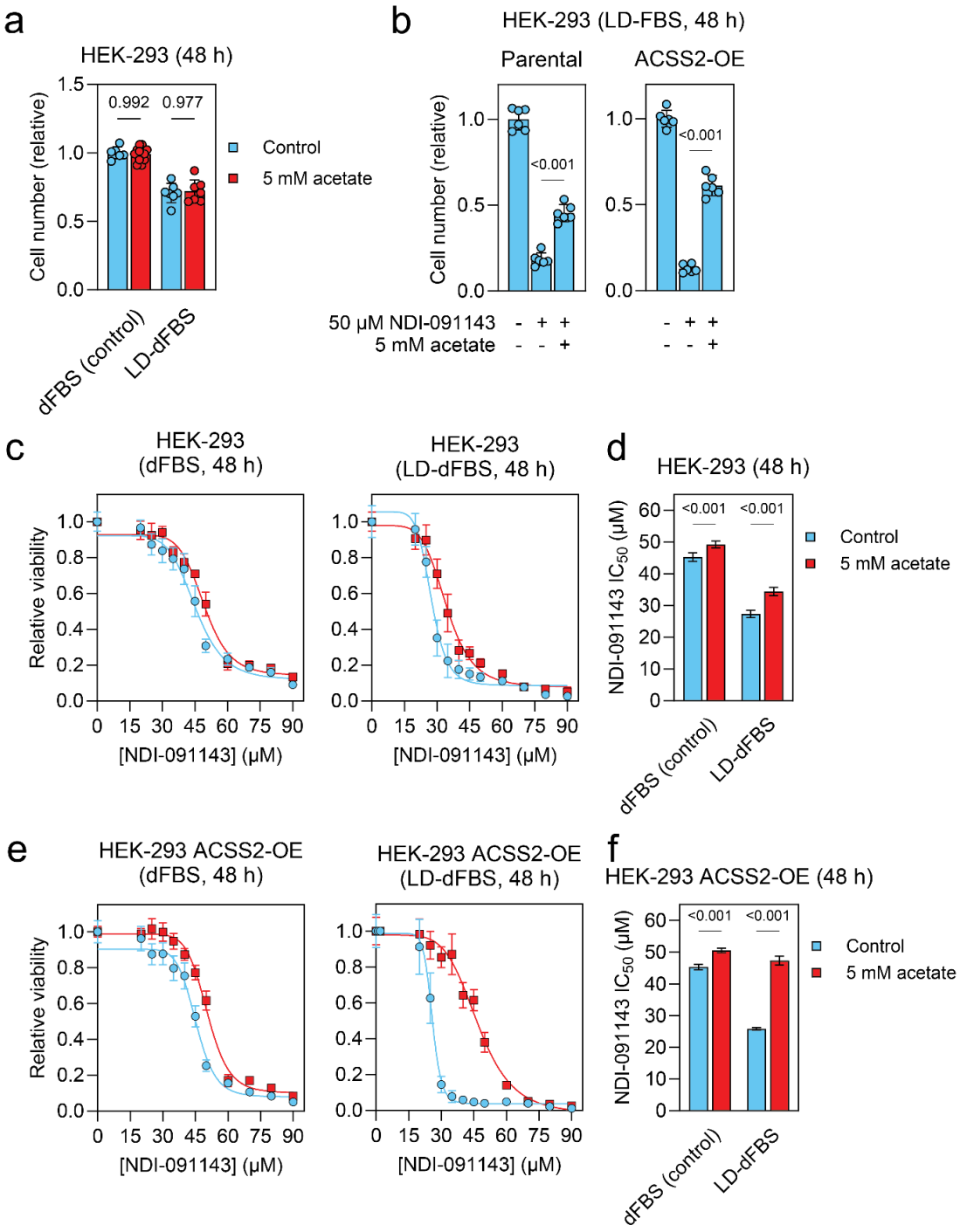

**Figure 5.11: Acetate rescues proliferation following medium lipid depletion and ACLY inhibition in an ACSS2-dependent manner. (a)** Relative cell number of HEK-293 cells cultured for 48 hours in medium supplemented with 10% dFBS or 10% LD-dFBS and treated with 5 mM acetate. Bar heights represent means, error bars represent standard deviations (*dFBS n = 6, LD-dFBS n = 7*). All conditions normalized to dFBS without acetate. P-value for unpaired two-tailed Student's t test is reported. **(b)** Relative cell number of HEK-293 parental and ACSS2-OE cells cultured for 48 hours in medium supplemented with 10% dFBS or 10% LD-dFBS and treated with 50 μM NDI-091143 and 5 mM acetate. Bar heights represent means, error bars represent standard deviations (*n = 6*). Conditions normalized to their relative vehicle control depending on serum type. P-value for Šídák's multiple comparisons test following one-way ANOVA is reported. **(c, e)** Dose-response curve on cell viability of HEK-293 parental **(c)** and HEK-293 ACSS2-OE **(e)** cells cultured for 48 hours with increasing concentrations of NDI-091143 and 5 mM acetate in medium supplemented with 10% dFBS (left) or 10% LD-dFBS (right). Data points represent means, error bars represent standard deviations (*n = 8*). **(d, f)** $IC_{50}$ concentrations (μM) for NDI-091143 treatment of HEK-293 parental **(d)** and HEK-293 ACSS2-OE **(f)** cells cultured for 48 hours with 10% dFBS or 10% LD-dFBS. Bar heights represent means, error bars represent standard deviations (*n = 8*). P-value for unpaired two-tailed Student's t test is reported.

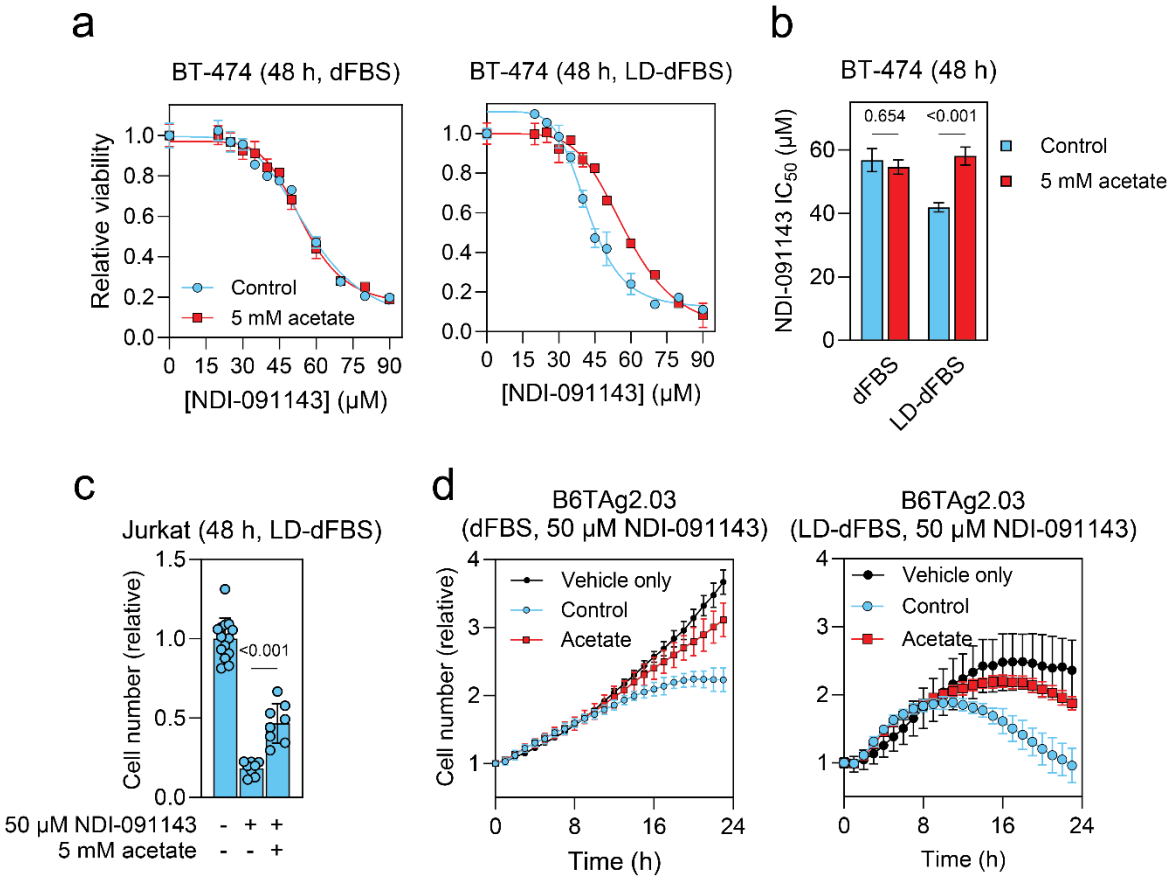


**Figure 5.12: The ability of acetate to rescue ACLYi-mediated cell proliferation impairment is not cell line-specific. (a)** Dose-response curve on cell viability of BT-474 cells cultured for 48 hours with increasing concentrations of NDI-091143 and 5 mM acetate in medium supplemented with 10% dFBS (left) or 10% LD-dFBS (right). Data points represent means, error bars represent standard deviations (*n = 8*). **(b)** $IC_{50}$ concentrations (μM) for NDI-091143 treatment of BT-474 cells cultured for 48 hours with 10% dFBS or 10% LD-dFBS. Bar heights represent means, error bars represent standard deviations (*n = 8*). P-value for unpaired two-tailed Student's t test is reported. **(c)** Relative cell number of Jurkat cells cultured for 48 hours in medium supplemented with 10% LD-dFBS and treated with 50 μM NDI-091143 and 5 mM acetate. Bar heights represent means, error bars represent standard deviations (*n = 14 for vehicle, n = 8 for treatments*). P-value for Šídák's multiple comparisons test following one-way ANOVA is reported. **(d)** Proliferation of

B6TAg2.03 cells cultured for 24 hours with either vehicle only, 50 μM NDI-091143 only (control) or 50 μM NDI-091143 and 5 mM acetate in medium supplemented with 10% dFBS (left) or 10% LD-dFBS (right). Data points represent means, error bars represent standard deviations (*n = 3*).

We orthogonally validated our CRISPR KO screen culture conditions by testing the rescue of proliferation by acetate in the murine hepatocellular cell line D42 with murine *Acly* KO (m*Acly* KO) and re-introduction of human ACLY activity to the KO clones (hACLY WT), which have been previously described in the literature (278). In agreement with the results for chemical ACLY inhibition, we find that parental cells having intact m*Acly* activity, as well as cells in which hACLY has been re-expressed, are not affected by acetate in lipid-depleted medium, while m*Acly* KO cells proliferate significantly more in the presence of acetate, with the magnitude of difference being larger in lipid-depleted medium (**Fig. 5.13a**). We confirmed that, like in cells treated with GSK2194069 to inhibit FASN (**Fig.5.9b**), D42 m*Acly* KO cells can be rescued by the addition of a defined mixture of lipids (LM1) (**Fig.5.13b**). When testing ACLY inhibition by NDI-091143, we predictably find that D42 parental and hACLY WT cells respond to the drug and acetate in the same way as all other cell lines considered, while the proliferation of m*Acly* KO cells is not further affected by treatment with the ACLY inhibitor, but can still be rescued by acetate supplementation (**Fig. 5.13c**). In agreement with the data about cell proliferation, we find that parental HEK-293 and D42 hACLY WT cells have a lower net acetate consumption flux when compared to D42 m*Acly* KO cells, and that this difference widens further when cells are cultured in lipid-depleted medium (**Fig.5.13d**). Overall, these data indicate that removing lipids from the medium and inactivating the enzyme ACLY is an effective and cell line-agnostic strategy to render cells dependent on acetate metabolism for *de novo* fatty acid biosynthesis. As the dependency is directly tied to the individual cell's ability to metabolize acetate, these conditions can be applied to a CRISPR KO screen targeting genes associated with acetate import.

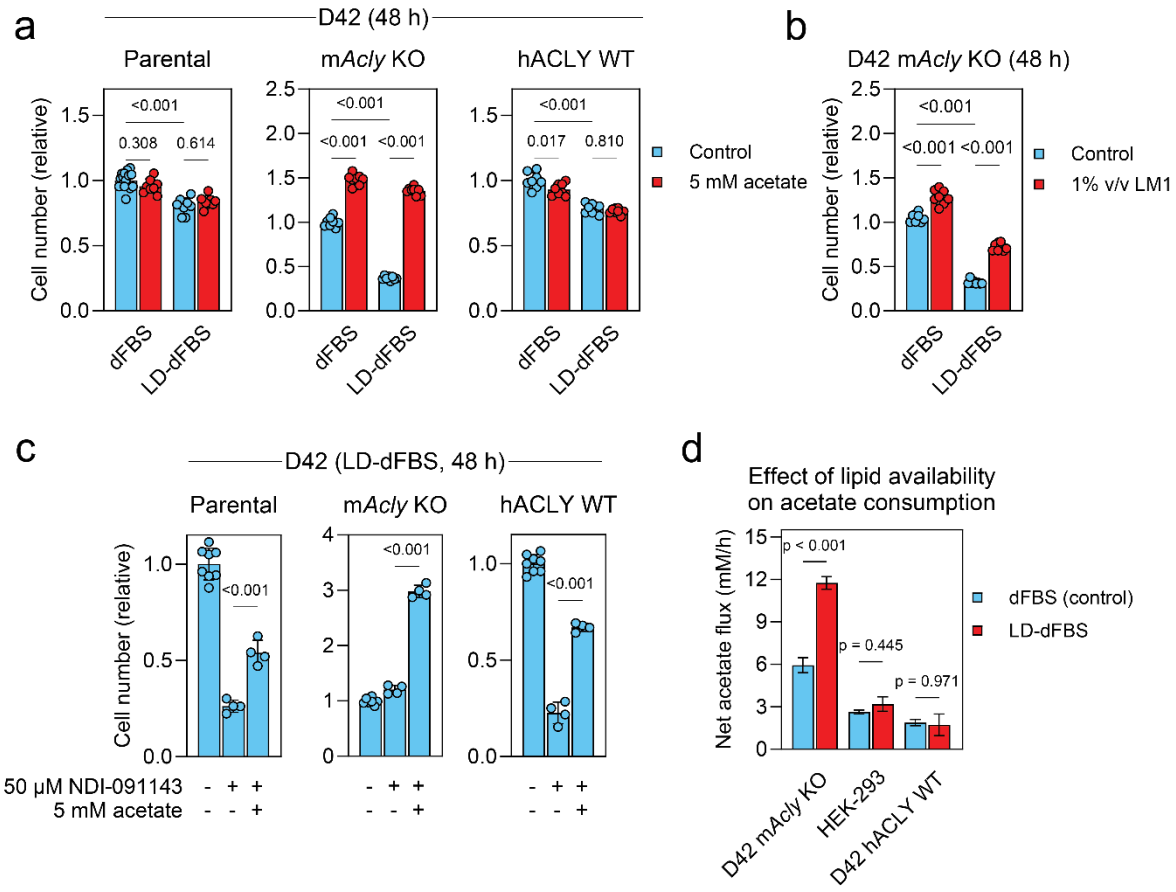


**Figure 5.13: Acetate rescues proliferation in *Acly* KO cells. (a)** Relative cell number of D42 parental (left), m*Acly* KO (center) and hACLY WT (right) cells cultured for 48 hours in medium supplemented with 10% dFBS or 10% LD-dFBS and treated with 5 mM acetate. Bar heights represent means, error bars represent standard deviations (*n = 8*). P-value for Šídák's multiple comparisons test following one-way ANOVA is reported. **(b)** Relative cells number of D42 m*Acly* KO cells cultured for 48 hours in medium supplemented with 10% dFBS or 10% LD-dFBS and treated with 1% v/v LM1. Bar heights represent means, error bars represent standard deviations (*n = 8*). P-value for Šídák's multiple comparisons test following one-way ANOVA is reported. **(c)** Relative cell number of D42 parental (left), m*Acly* KO (center) and hACLY WT (right) cells cultured for 48 hours in medium supplemented with 10% LD-dFBS and treated with 50 µM NDI-091143 and 5 mM acetate. Bar heights represent means, error bars represent standard deviations (*n = 8 for vehicle, n = 4 for*

*treatments*). P-value for Šídák's multiple comparisons test following one-way ANOVA is reported. **(d)** Net acetate consumption flux (mM/h) of D42 m*Acly* KO and hACLY cells and HEK-293 parental cells. Bar heights represent means, error bars represent standard deviations (*n = 3*). P-value for unpaired two-tailed Student's t test is reported.

### *Pyruvate and triacetin can rescue proliferation of cells in the same conditions as acetate*

To have additional control conditions in the CRISPR KO screen that could allow us to discriminate genes essential for acetate metabolism only, we tested a number of different nutrients for their ability to rescue proliferation in lipid-depleted medium when ACLY is inhibited or ablated. In particular, we were interested in testing triacetin (glycerol triacetate), which has been previously used to increase systemic acetate levels *in vivo* (291). In accordance with previous studies on the hydrolysis of triacetin to yield acetate (**Fig. 5.14a**) (292), we find that non-enzymatic conversion of triacetin to acetate occurs in sterile solutions over a period of months, while the process is greatly accelerated when triacetin comes in contact with live cells (**Fig.5.14b**). While previous reports indicate that lipases are involved in this reaction (293), we did not investigate whether the conversion of triacetin to acetate occurs outside or inside the cell. By assaying a number of compounds including triacetin, we find that in both D42 m*Acly* KO and HEK-293 cells, triacetin and pyruvate are both capable of rescuing proliferation (**Fig. 5.14c**). Additionally, we find that the proliferation rescue mediated by acetate, but also triacetin and to some extent pyruvate can be negated by treating cells with GSK2194069 and VY-3-135 to inhibit FASN and ACSS2 respectively (**Fig.5.14d,e**). We also tested if the MCT1 inhibitor AZD3965 could abrogate the acetate-mediated proliferation advantage in the same way as VY-3-135, but we find that the inhibitor does not impact the effect of acetate on D42 m*Acly* KO cells (**Fig.5.15**) Overall, these data indicate the triacetin and pyruvate can be used as additional treatments to rescue proliferation in a CRISPR KO screen in order to discriminate genes specifically essential for acetate import.

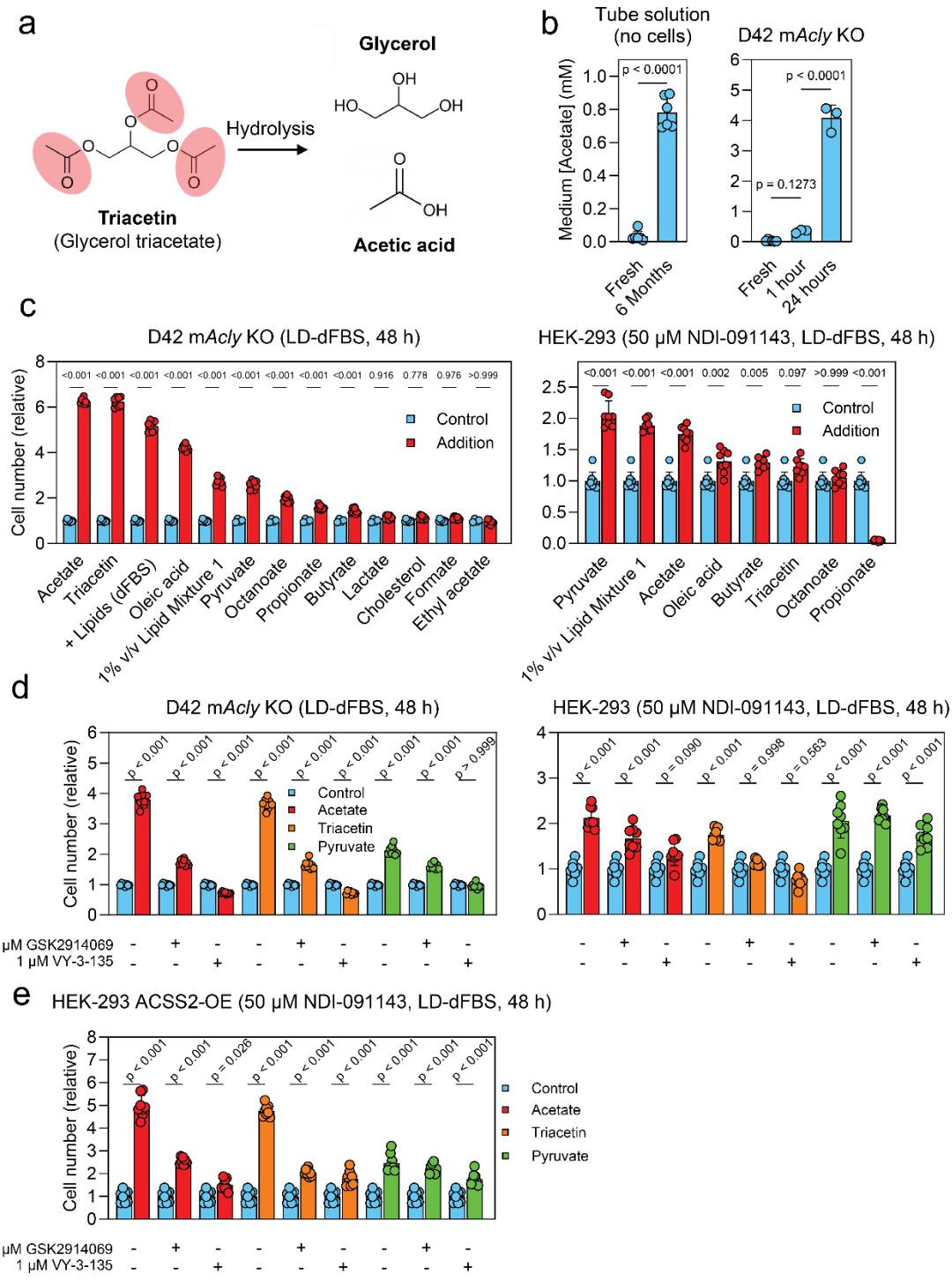


**Figure 5.14: Triacetin and pyruvate confer a proliferation advantage like acetate to cells in the CRISPR KO screen culture conditions. (a)** Schematic of triacetin conversion to glycerol and acetic acid. Each molecule of triacetin carries three

acetyl moieties and can be hydrolyzed to 3 molecules of acetatic acid for each molecule of glycerol. **(b)** Concentration of acetate (mM) measured from a sterile tube solution (left) or from medium in contact with live D42 m*Acly* KO cells. In both experiments triacetin was originally dissolved at a concentration of 2 mM. Bar heights represent means, error bars represent standard deviations (*n = 6 for sterile solutions, n = 3 for medium samples*). P-value for unpaired two-tailed Student's t test (left) and for Šídák's multiple comparisons test following one-way ANOVA (right) is reported. **(c)** Relative cell number of D42 m*Acly* KO (left) and HEK-293 parental (right) cells cultured for 48 hours in medium supplemented with 10% LD-dFBS. HEK-293 cells were treated with 50 μM NDI-091143, and both cell lines were supplemented with one of the following (unless otherwise indicated in the figure): 5 mM acetate, 2 mM triacetin, 10% dFBS in place of LD-dFBS, 30 μM oleic acid, 1% v/v LM1, 5 mM pyruvate, 60 μM octanoate, 500 μM propionate, 250 μM butyrate, 5 mM lactate, 6 μM cholesterol, 500 μM formate, or 2 mM ethyl acetate. Bar heights represent means, error bars represent standard deviations (*n = 8*). Control conditions belonging to the same experiment are repeated for clarity of comparison. P-value for Šídák's multiple comparisons test following one-way ANOVA is reported. **(d,e)** Relative cell number of D42 m*Acly* KO (left), HEK-293 parental (right) **(d)**, and HEK-293 ACSS2-OE **(e)** cells cultured for 48 hours in medium supplemented with 10% LD-dFBS. HEK-293 parental and ACSS2-OE cells were treated with 50 μM NDI-091143, and all three cell lines were supplemented with one of the following: 5 mM acetate, 2 mM triacetin or 5 mM pyruvate. All supplementations were tested with 1 μM GSK2194069 and 1 μM VY-3-135. Bar heights represent means, error bars represent standard deviations (*n = 8*). Control conditions belonging to the same experiment are repeated for clarity of comparison. P-value for Šídák's multiple comparisons test following one-way ANOVA is reported.

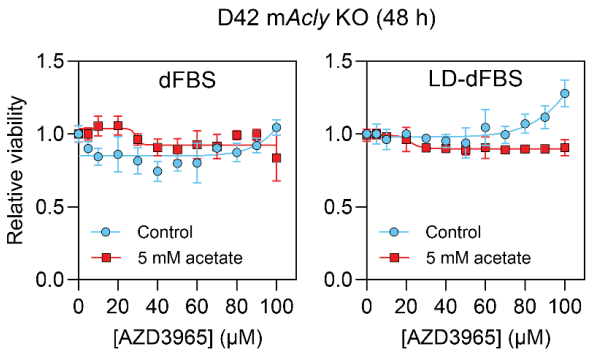


**Figure 5.15: Inhibition of MCT1 by AZD3965 does not affect the proliferation rescue of acetate in m*Acly* KO cells.** Dose-response curve on cell viability of D42 m*Acly* KO cells cultured for 48 hours with increasing concentrations of AZD3965 and 5 mM acetate in medium supplemented with 10% dFBS (left) or 10% LD-dFBS (right). Data points represent means, error bars represent standard deviations (*n* = *8*). Each condition is normalized to its relative cell number with no drug.

*Lipid depletion and Complex I inhibition render cells depended on acetate for proliferation*

Although we ultimately decided to apply inhibition of ACLY with low lipid content as our main CRISPR KO screen condition, we also hypothesized that treatment with the Complex I inhibitor Fasnall combined with lipid-depleted culture conditions could provide an environment in which cells would become dependent on acetate for proliferation. This was based on the understanding that, by avoiding $NAD^+$ consuming reactions for the production of cytosolic acetyl-CoA, acetate can reduce the dependence on exogenous lipids when electron acceptors are limited by OXPHOS inhibition (**Fig. 5.16a**) (294). Indeed, while we find that acetate has no effect on proliferation in cells treated with Fasnall in dFBS medium, the same treatment in LD-dFBS shows that acetate can rescue cell proliferation (**Fig.5.16b,c**). Overall, these data indicate that Complex I inhibition and lipid depletion also render cells dependent on acetate metabolism.

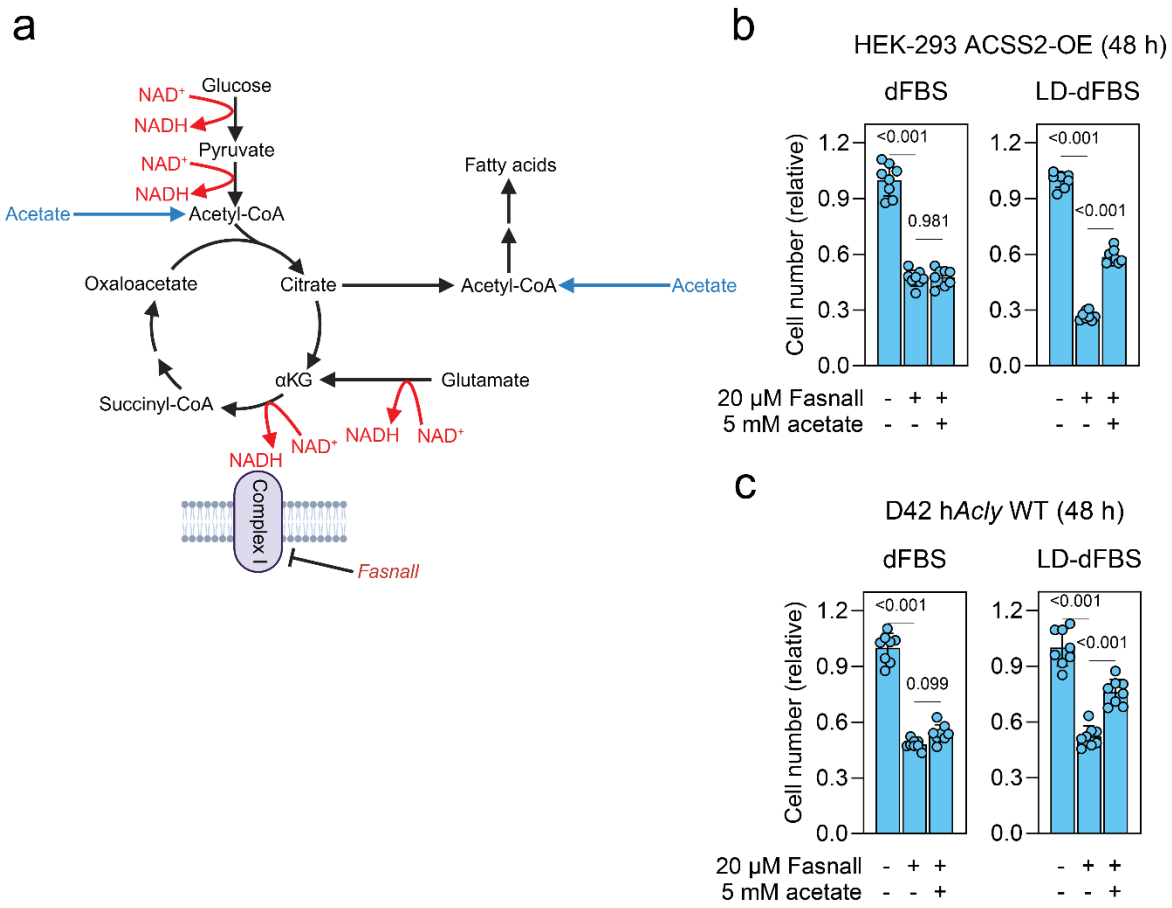


**Figure 5.16: Acetate rescues proliferation following medium lipid depletion and Complex I inhibition**. **(a)** Schematic of the metabolic pathways for nucleocytosolic acetyl-CoA production and their associated requirements for electron disposal in the form of generation of NADH. Fasnall inhibitory activity against complex I is shown. **(b,c)** Relative cell number of HEK-293 ACSS2-OE **(b)** and D42 m*Acly* KO **(c)** cells cultured for 48 hours in medium supplemented with 10% dFBS or 10% LD-dFBS and treated with 20 μM Fasnall and 5 mM acetate. Bar heights represent means, error bars represent standard deviations (*n* = *8*). P-value for Šídák's multiple comparisons test following one-way ANOVA is reported.

*CRISPR KO screen conditions can be sustained in long-term culture*

To carry out a CRISPR KO screen and allow genes essential in the culture conditions tested to disappear from the cell population it is necessary to culture cells for a certain number of days, which can depend on the specific cell line's proliferation rate. As a consequence of this, we tested the ability of cells that were previously only subjected to experimental conditions for up to 48 hours to a long-term trial of multiple passages under lipid-depletion and ACLY inhibition conditions. We find that cells change their morphology and significantly slow down their proliferation when treated with the ACLY inhibitor NDI-091143, but remain viable even after multiple passages (**Fig.5.17**). We did observe that trypsinization and surface attachment are processes that can increase cell death in treated conditions, so we considered this when performing the experimental CRISPR screen, by splitting at a lower fraction or in some cases passaging the whole population to conserve cells undergoing selection under the screening conditions. We did not test a condition with ACLY inhibition, lipid-depletion and no acetate as most cell lines tested either do not survive it or alternatively remain viable, but do not proliferate. Overall, we find that cells can remain viable for long-term culturing in the CRISPR KO screen conditions we elected to employ.

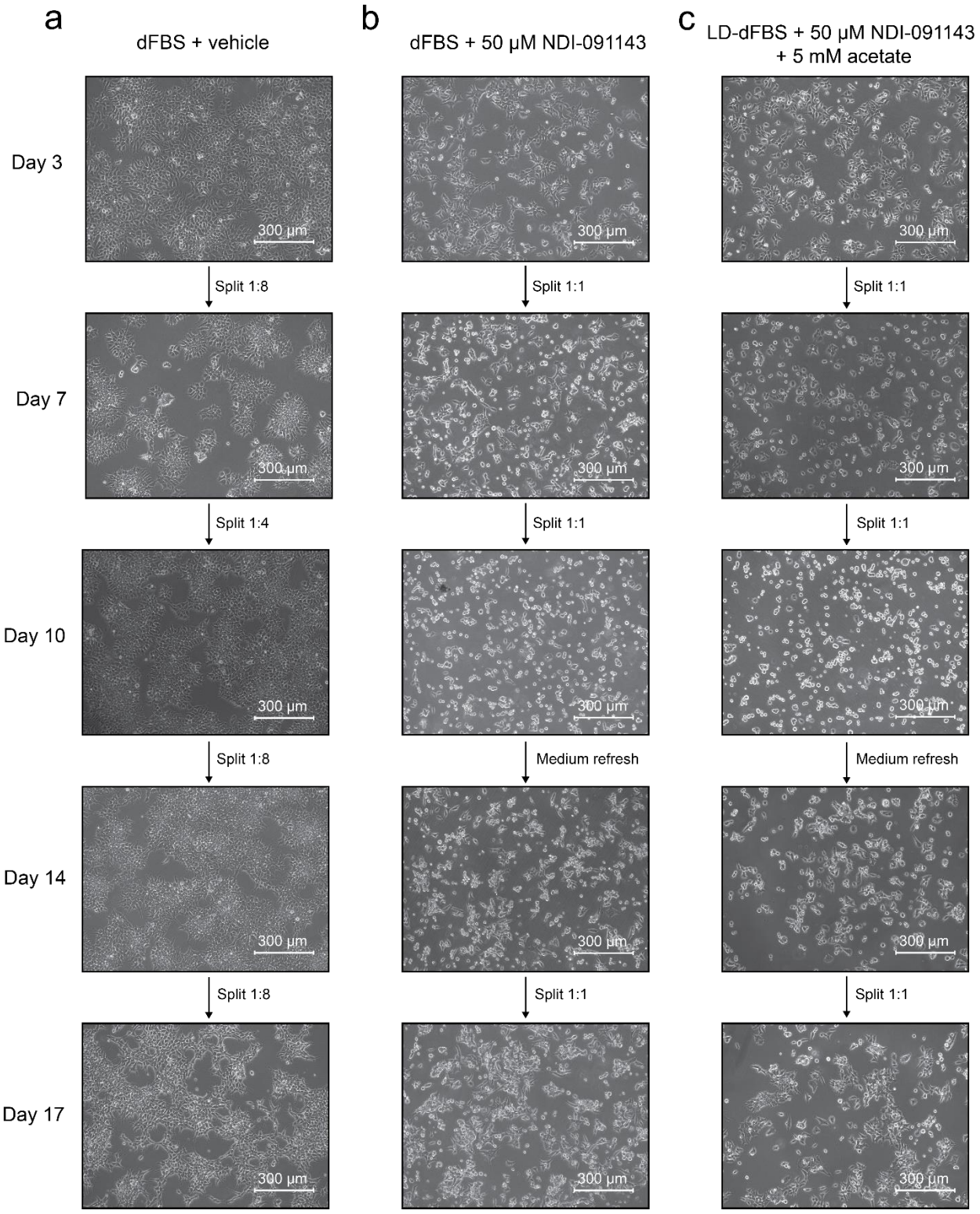


**Figure 5.17: HEK-293 ACSS2-OE cells remain viable in CRISPR KO screen conditions.** Phase-contrast micrographs of HEK-293 ACSS2-OE cells cultured for

17 days under one of three conditions: 1) 10% dFBS + vehicle, 2) 10% dFBS + 50 μM NDI-091143, and 3) 10% LD-dFBS + + 50 μM NDI-091143. Successive instances of passaging and split ratio or medium refresh are indicated. Representative examples of *n = 3* experiments shown.

### *CRISPR KO screen preparation*

Pooled CRISPR screens rely on a library of guide RNAs (gRNA) to introduce genetic perturbations inside a cell population in a heterogeneous fashion. This is then followed by a biological challenge that affects cell proliferation (or other measurable phenotypes) differently based on the specific genetic modification inside each cell in the pool, which in the case of a CRISPR KO screen is gene deletion (295). The result is that the KO of genes that are essential for cell proliferation in the challenge condition will cause the associated gRNAs to disappear from the cell population. This can be quantified once the experiment is over by collection of the pooled genomic DNA, followed by PCR amplification of the gRNA regions and high-throughput sequencing and identification of those regions.

To introduce gRNAs, it is necessary to carefully calibrate the multiplicity of infection (M.O.I.) of the lentiviral library. The objective is to maximize the number of cells with a single gRNA integration event in their genome, while avoiding instances of multiple integration events, which can complicate the interpretation of results. In accordance with the Poisson distribution for the occurrence of random events, CRISPR screens are usually carried out at a M.O.I. of 0.3, which roughly corresponds to 30% of the cell population successfully transduced by the lentiviral pooled gRNA library (296). Additionally, unless all-in-one libraries containing both a single gRNA (sgRNA) and a Cas9 expression construct are used, cells need to be clonally selected before the screen to confirm that the entire experimental population expresses Cas9 and will thus be subjected to the genetic perturbations and biological challenge of the experimental conditions as hypothesized (297).

We employed two whole-genome dual-gRNA libraries, one for the human genome and one for the murine genome. The human library covered 20,048 genes with 91,926 gRNA pairs, while the murine library covered 20,493 genes with 90,344 gRNA pairs. “Dual-gRNA” implies

the presence of pairs of gRNAs whose purpose is to introduce large deletions in the genome, instead of single point mutations. We decided to employ a whole-genome library, instead of one focused on solute carrier transporters (SLC), in order to probe genes that may not be currently classified as SLC, but are still involved in metabolite transport. The classification of SLCs is in constant revision, and genes that at the time of their discovery were not classified as SLCs, like the serine transport family of sideroflexins (SFXNs), have since been included, in the case of SFXNs as making up the SLC56 family (207,298). We therefore adapted the number of cells involved in the screen to guarantee at least 250 reads per sgRNA, before the dropout of essential housekeeping genes is considered.

To prepare for the screen, we set out to define an assay that would allow us to determine the viral transduction efficiency. Given that the gRNA libraries include an expression construct for green fluorescent protein (GFP), we employed flow cytometry measurements for all determinations of transduction efficiency and active Cas9 presence. We confirmed that our method of assaying transduction efficiency is reliable by testing increased amounts of lentiviral vectors for GFP expression (**Fig.5.18a**), noting that transduction efficiency against viral amount follows a sigmoidal curve (**Fig.5.18b**). While for all other viral manipulations we used the cationic polymer polybrene to enhance transduction efficiency, we validated our assay by recapitulating the reported fact that lymphocytes, like the T cell leukemia-derived Jurkat cell line, can have their transduction efficiency dramatically increased by treatment with the poloxamer Synperonic F108 in place of polybrene, although this is not the case for other cell lines such as the myeloid leukemia-derived MOLM-13 (**Fig.5.18c,d**).

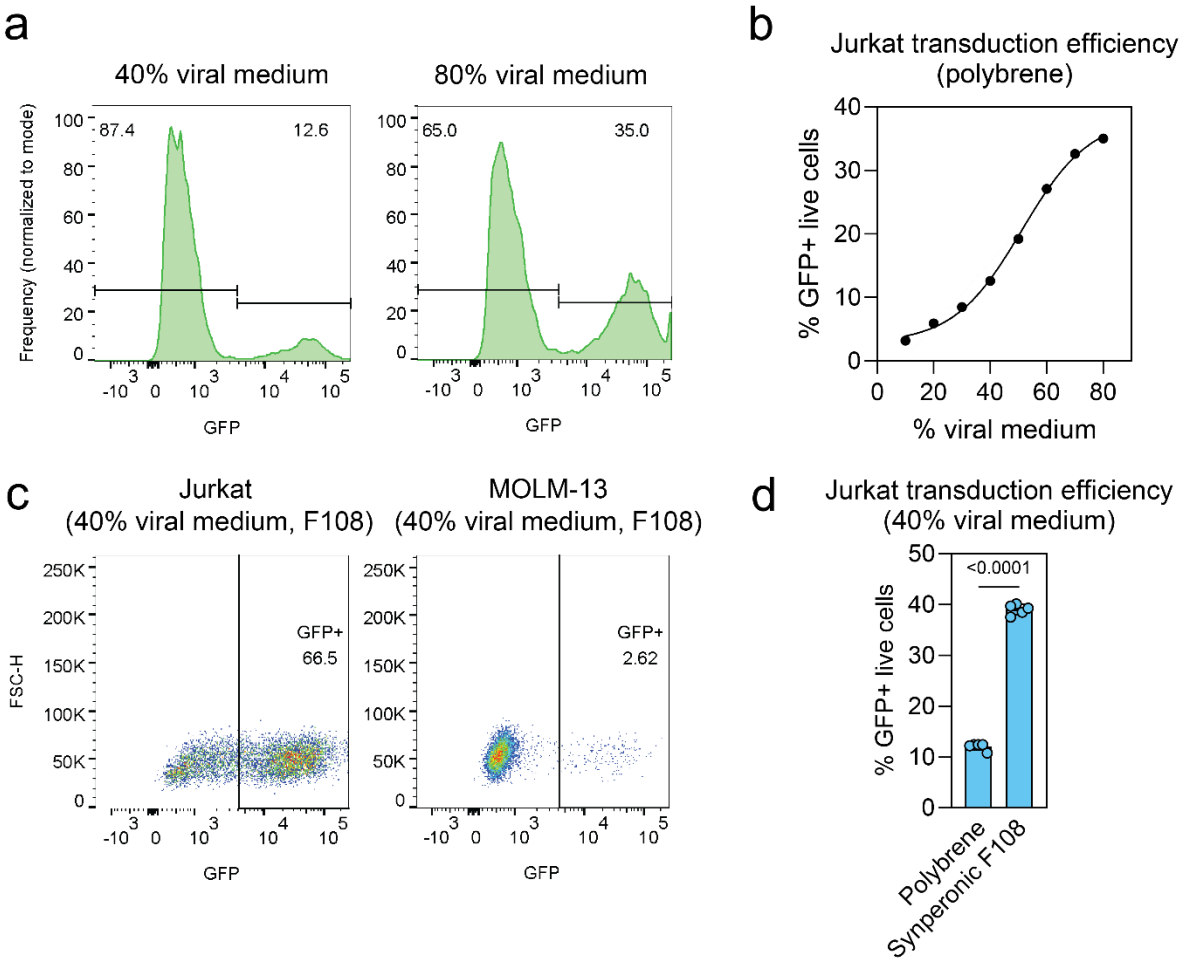


**Figure 5.18: GFP fluorescence can be used to measure lentiviral transduction efficiency.** **(a)** Normalized frequency of GFP negative or positive Jurkat cells infected with 40% (left) or 80% (right) v/v lentiviral medium and 10 µg/mL polybrene. Representative examples, 10,000 events recorded for each. **(b)** Lentiviral transduction efficiency of Jurkat + 10 µg/mL polybrene and increasing percentage of v/v lentiviral medium. Data points represent the percentage of GFP+ cells in a single recording of 10,000 events. **(c)** Pseudocolor dot plot of cell events gated for GFP fluorescence of Jurkat (left) and MOLM-13 (right) cells infected with 40% v/v viral medium and 1 mg/mL Synperonic F108. Representative example of *n* = *5* experiments, 10,000 events recorded for each replicate. **(d)** Lentiviral transduction efficiency of Jurkat infected with 40% v/v viral medium and either 10 µg/mL

polybrene or 1 mg/mL Synperonic F108. Bar heights represent means, error bars represent standard deviations (*n* = *5*). P-value for unpaired two-tailed Student's t test

To employ stable clonal cell lines expressing Cas9 it is not sufficient to transduce a pool of cells with a Cas9 lentiviral vector, select them for the presence of an antibiotic marker and then isolate clonal populations. This is because antibiotic-resistant but Cas9-inactive cells are always present in the transduced pooled population due to mutations in the proviral Cas9 coding sequence and epigenetic silencing of the inserted Cas9 gene (297,299). For this reason, after clonal expansion, we analyzed the clones' Cas9 activity by a dual fluorescence reporter system (**Fig.5.19a**) (297). The reporter system relies on the concomitant expression of green fluorescent protein (GFP) and blue fluorescent protein (BFP) in transduced cells, and harbors a gRNA sequence targeting GFP, such that if a transduced cell expresses active Cas9, then the signal for green fluorescence disappears and only blue fluorescence is recorded (**Fig. 5.19b**). With this reporter system we analyzed 45 clones for the D42 m*Acly* KO cell line (**Fig.5.19c**), 96 clones for the HEK-293 ACSS2-OE cell line (**Fig.5.20a**), and 21 clones for the B6TAg2.03 cell line (**Fig.5.20b**). Each clonal cell line was considered as having homogeneous Cas9 activity sufficient to be employed in the CRISPR KO screen if the percentage of the infected subpopulation having lost GFP fluorescence was between 98 to 99%. The best clones for each cell line were then used to titrate the M.O.I. of the species-matched CRISPR gRNA library to determine the infection conditions achieving 30% of positively transduced cells (**Fig. 5.21a-c**).

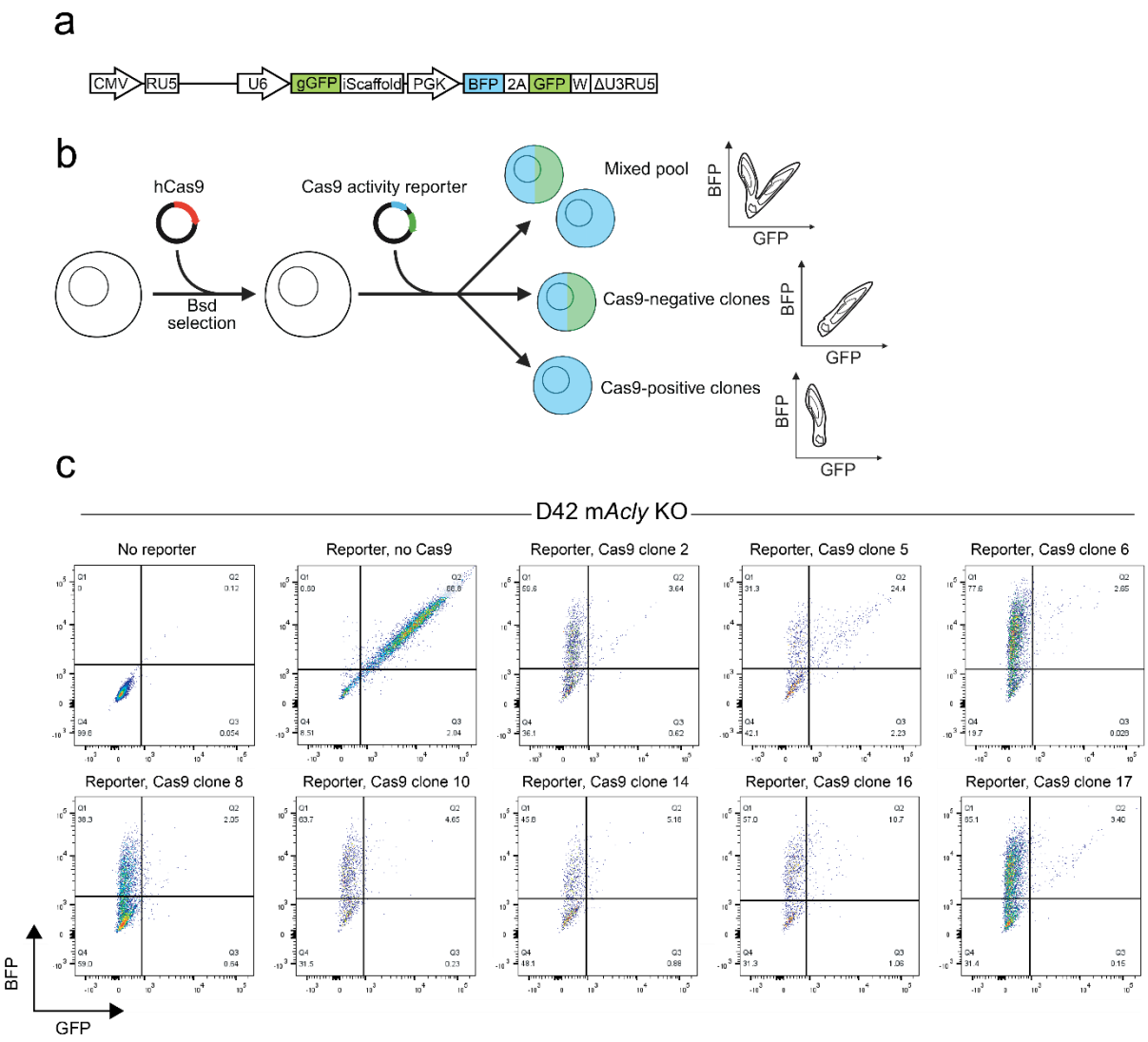


**Figure 5.19: A dual fluorescence reporter system is used to identify Cas9-active clonal cell lines. (a)** Schematic of the reporter construct. CMV: Cytomegalovirus promoter; gGFP: guide RNA targeting GFP; PGK: phosphoglycerate kinase promoter. **(b)** Schematic of the workflow for confirming Cas9 activity in clonal populations: a non-clonal mixed pool will contain cells expressing both GFP and BFP and others only expressing BFP; all cells of a Cas9-negative clonal population will express both GFP and BFP; all cells of Cas9-positive clonal population will express only BFP. **(c)** Pseudocolor dot plot of D42 m*Acly* KO transduced with Cas9 and tested with the activity reporter. Cell events gated for BFP+ and GFP+. Representative examples for 10 clones out of 45 analyzed, 10,000 events recorded for each.

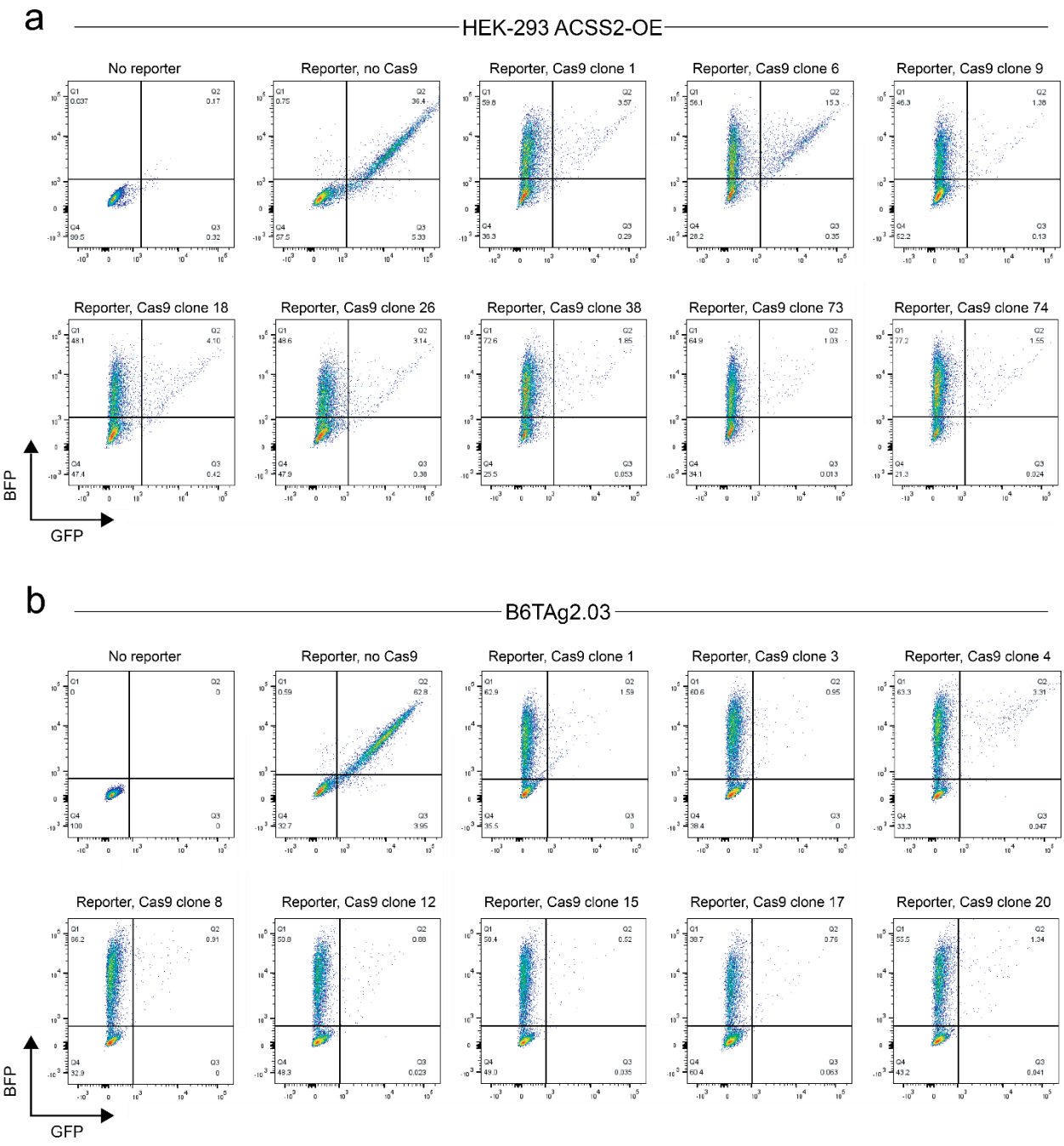


**Figure 5.20: Active Cas9 clones for HEK-293 ACSS2-OE and B6TAg2.03 cell lines.** **(a-b)** Pseudocolor dot plot of HEK-293 ACSS2-OE **(a)** and B6TAg2.03 **(b)** cells transduced with Cas9 and tested with the activity reporter. Cell events gated for BFP+ and GFP+. Representative examples for 10 clones out of 96 **(a)** or 21 **(b)** analyzed, 10,000 events recorded for each.

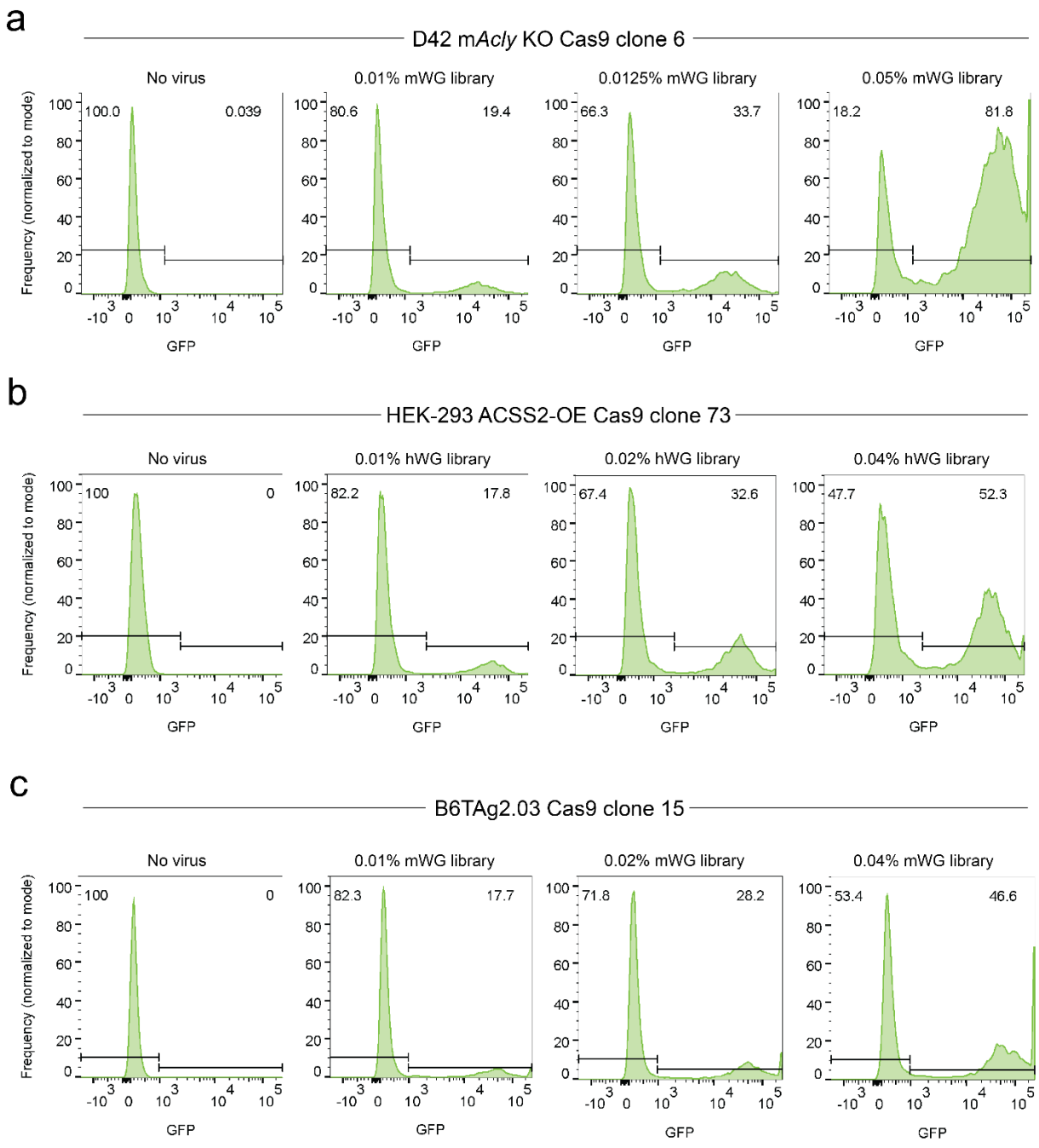


**Figure 5.21: CRISPR whole-genome dual gRNA library titration. (a-c)** Normalized frequency and population percentage of D42 m*Acly* KO Cas9 clone 6 **(a)**, HEK-293 ACSS2-OE Cas9 clone 73 **(b)**, and B6TAg2.03 Cas9 clone 15 **(c)** gated for GFP+ from infection of murine **(a,c)** or human **(b)** gRNA library at different percentages of viral

medium. mWG: mouse whole-genome gRNA library; hWG: human whole-genome gRNA library.

### *SLC16A13 is identified by a CRISPR KO screen for dependencies on acetate metabolism in murine hepatocellular carcinoma cells*

In this work we present the results of the acetate-based CRISPR KO screen performed with the first of the three cell lines selected, namely the murine hepatocellular carcinoma D42 m*Acly* KO cell line. The experiment was designed with a control condition in lipid replete medium with 10% dFBS and three experimental conditions in lipid-depleted medium with 10% LD-dFBS and supplementation of either 5 mM acetate, 5 mM pyruvate or 2 mM triacetin (**Fig. 5.22a**). This cell line was chosen because it would provide an orthogonal control to screens performed using ACLY chemical inhibition and because, among the cell lines used in this work, it is among the fastest proliferating ones, as are HEK-293 and B6TAg2.03 (**Fig.5.22b**). Upon infection with the murine whole-genome dual gRNA library (**Fig.5.22c**), cells were cultured in complete medium and selected for puromycin resistance during the first 21 days of culture. Throughout this period, cell morphology was assessed, and it was observed that from day 10 onwards, many cells started to present an enlarged morphology (**Fig.5.22d**). Additionally, we recorded widespread cell death not related to puromycin, which we ascribed to the dropout of essential housekeeping genes and to additional synthetic lethality due to the *Acly* KO background of these cells. After culturing cells in separate replicates for an additional 15 days in the respective experimental conditions, extracting the genomic DNA, amplifying and sequencing the gRNA regions, we find that on average each condition presents ~100 genes that are either underrepresented or overrepresented in the experimental conditions compared to control (**Fig.5.23a**). We find that *Fasn* is always significantly underrepresented in all three experimental conditions, due to the dependency on *de novo* fatty biosynthesis enforced by the supplementation with LD-dFBS and KO of *Acly*. We also find that acetate and triacetin conditions present several genes that are differentially regulated in the same way, including Cyp2b9 and, intriguingly, the gene Slc16a13 encoding for the monocarboxylate transporter MCT13 (**Fig.5.23b,c**). Following up on this finding, we performed net acetate consumption flux analysis on a human cell line

instead, HEK-293 ACSS1-OE, modified with knockdown (KD) constructs for SLC16A13, and we find that all MCT13 KD cell lines have some level of significant reduction in net acetate consumption (**Fig.5.23d**). Overall, these data suggest that MCT13 is a transporter involved in acetate utilization and that this is likely the case between different cancer types and species.

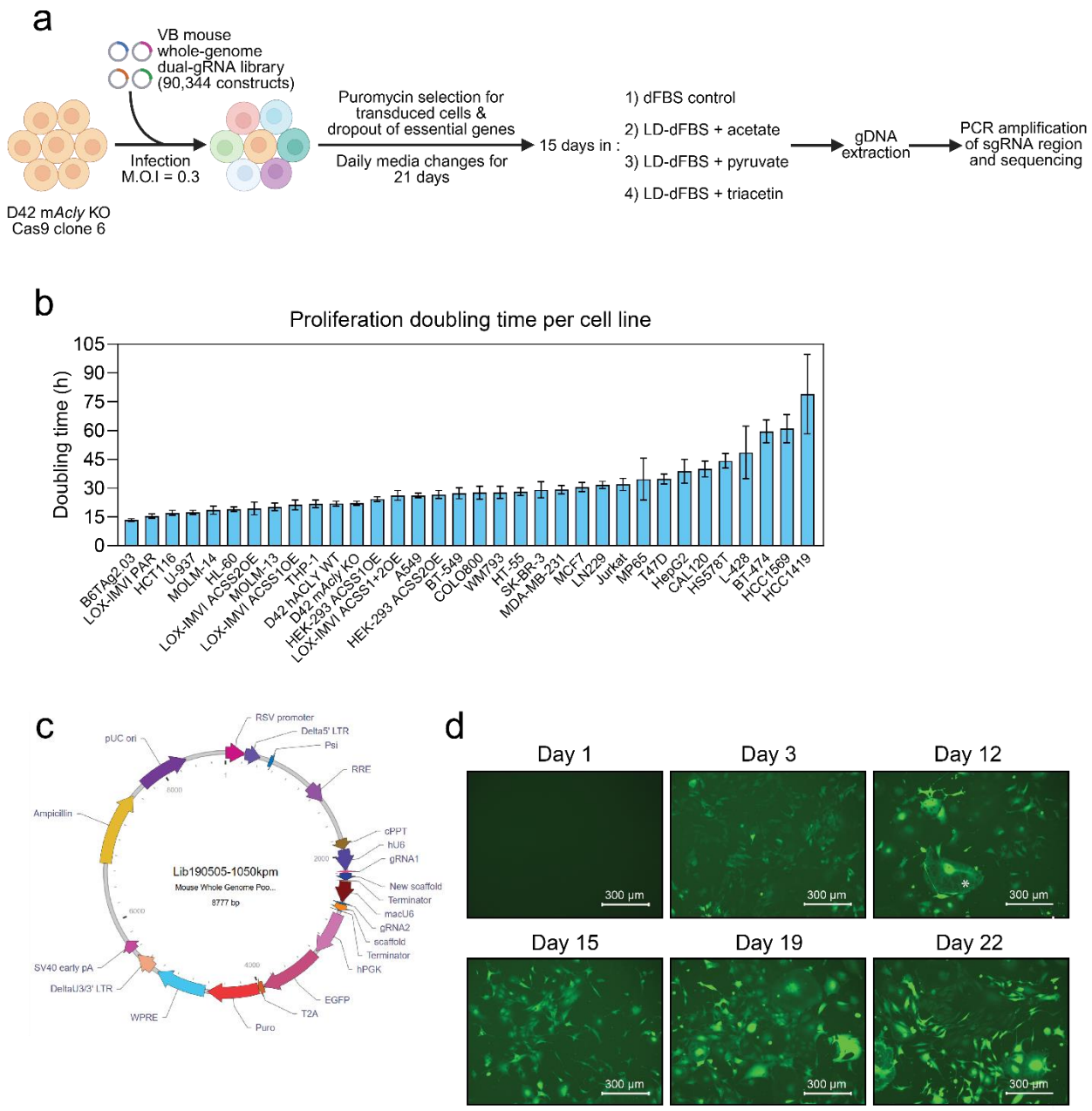


**Figure 5.22: D42 m*Acly* KO CRISPR KO screen. (a)** Schematic of the procedure for the CRISPR KO screen performed with D42 m*Acly* KO Cas9 clone 6 cells. **(b)** Doubling time of most of the cell lines employed for this work. Bar heights represent

means, error bars represent standard deviations (*n* = *3*). **(c)** Schematic map of the murine whole-genome dual gRNA CRISPR library. **(d)** Representative epifluorescence micrographs of cells taken throughout the duration of the screen. On the third panel on top, a cell with enlarged cell morphology is indicated with a white asterisk.

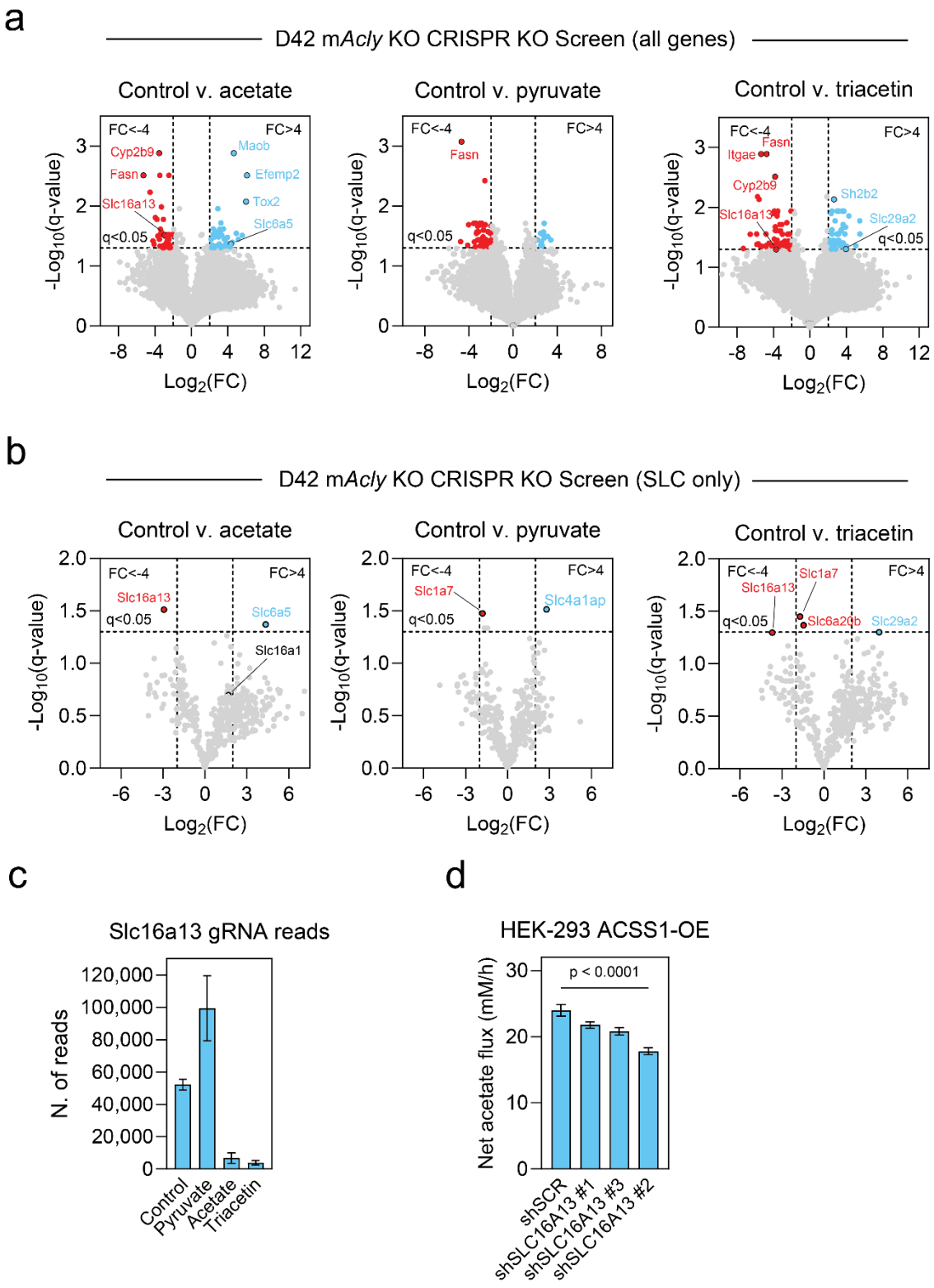
a
D42 mAcly KO CRISPR KO Screen (all genes)
Control v. acetate
Control v. pyruvate
Control v. triacetin
FC<-4
FC>4
q<0.05
Cyp2b9
Fasn
Slc16a13
Maob
Efemp2
Tox2
Slc6a5
Itgae
Sh2b2
Slc29a2
-Log10(q-value)
Log2(FC)
b
D42 mAcly KO CRISPR KO Screen (SLC only)
Slc1a7
Slc4a1ap
Slc16a1
Slc6a20b
c
Slc16a13 gRNA reads
N. of reads
Control
Pyruvate
Acetate
Triacetin
d
HEK-293 ACSS1-OE
p < 0.0001
Net acetate flux (mM/h)
shSCR
shSLC16A13 #1
shSLC16A13 #3
shSLC16A13 #2

**Figure 5.23: MCT13 is functionally involved in acetate utilization. (a,b)** All genes **(a)** or only SLC genes **(b)** underrepresented (red) or overrepresented (blue) in experimental conditions compared to control in the CRISPR KO screen of D42 m*Acly* KO cells. Data points represent means of $\log_2$(fold-change) for each gRNA pair. Q-value for Benjamini-Hochberg multiple comparisons correction of unpaired two-tailed Student's t test are reported. **(c)** Number of reads per Slc16a13 gRNA only. Bar heights represent means, error bars represent standard deviations. **(d)** Net acetate consumption flux (mM/h) of HEK-293 ACSS1-OE cells modified with either shSCR, shSLC16A13 #1-3 or SLC16A13-OE constructs. Bar heights represent means, error bars represent standard deviations (*n = 3*). P-value for Šídák's multiple comparisons test following one-way ANOVA is reported.

# CHAPTER 6: DISCUSSION

The research work presented in this thesis sought to quantitatively characterize acetate utilization in a variety of cancer cell models, and to combine available transporter gene expression data with a genomic screen for acetate essentiality in order to identify novel transporters involved in acetate import. We report that acetate consumption is variable between and within cancer types (**Fig.3.4**) and correlated with acetate metabolism-associated gene expression levels (**Fig.3.6**), that its magnitude is primarily dictated by the need to fuel the TCA cycle (**Fig.3.7**), and that inhibitors of the monocarboxylate transporters MCT1 and MCT4 only partially affect acetate consumption (**Fig.3.8**). We find that MCT1, MCT4 and MCT13 are ubiquitously expressed in the large majority of cancer cell line models available for research, although some cell lines with high acetate consumption capabilities do not express high levels of MCT1 (**Fig.4.1**). We describe how MCT13 gene expression is linked to acetate metabolism by its correlation with acetyl-CoA synthetase (ACSS2) expression, which is unique among the three MCTs considered hitherto (**Fig.4.2**). We present a CRISPR knockout (KO) screen which we developed in order to render cancer cells dependent for their biosynthetic needs on acetate metabolism. We find that this can be achieved by inhibition of the enzyme ATP citrate lyase (ACLY) and that the magnitude of dependence on acetate is increased by removing lipids from the culture medium (**Fig.5.11, 5.12, 5.13**). We also report on how inhibition of Complex I can achieve the same role for acetate (**Fig.5.16**), while substitution of glucose for galactose in the medium allows acetate to partially spare glutamine utilization (**Fig.5.3, 5.4**), but not to become essential for cell proliferation. Lastly, we report how CRISPR KO screen conditions including acetate or the metabolically equivalent molecule triacetin highlight MCT13 as a gene essential for acetate-dependent cell proliferation, contrary to the condition supplemented with pyruvate (**Fig.5.23**).

The main novelty of our approach has been the combination of a metabolomics platform capable of quantitatively detecting acetate and of a genetic screening system. Indeed, a similar approach performed on a larger scale by the RESOLUTE Consortium, measuring metabolic changes on a panel of cell lines for which each SLC had been individually deleted,

did not report anything on acetate transport, because acetate itself was not included in the list of metabolites detected, nor was it present in the culture conditions in the first place (210). In regards to our metabolomics platform, we specifically validated its capability to provide us with accurate and consistent readouts throughout the course of this work (**Fig.3.2**), as it is known that some level of enzymatic activity can remain present even in samples processed for metabolomics analysis (300), which can, in time, reduce the content of certain metabolite, thus compromising the quantitative measurements on which this work is based. As an additional layer of validation, we measured the consumption flux of other essential metabolites used in cell culture, thanks to which we were able to find correspondence between our results and previous measurements available in the literature. For instance, in the case of glucose consumption flux, both our data (**Fig.3.5a**) and previous calculations for glycolysis rate flux show comparable results centered around 100 mM/h for different cancer types (301).

With regards to our investigation of net acetate consumption flux in cancer cells (**Fig.3.4c**), it is notable how for many cell lines acetate and glutamine consumption are within a comparable range of 5 – 40 mM/h. We did not expect, and indeed do not observe except for BT-474 cells, that acetate consumption flux would be comparable to that of glucose, but it is still notable to confirm that acetate ranks among the three main sources of carbons for cancer cells. Consumption fluxes were also calculated but not reported for all amino acids present in RPMI 1640, and while some like serine are readily consumed by cancer cells, it is uncommon for them to approach the magnitude of flux that glucose, glutamine or acetate have for most cell lines. In terms of secretion of acetate, we did not systematically investigate this, and thus we can report data only for a limited number of cell lines (**Fig.3.4d**). In relation to this, we confirmed previous observations on the fact that pyruvate can be converted to acetate in the presence of reactive oxygen species (ROS) (113), though the data has not been reproduced here. The original article which presented this phenomenon and the related enzymatic conversion of pyruvate to acetate also used one of the same cell lines from which we observe significant acetate secretion, HCT116. Assuming that these cells secrete excess intracellular acetate due to this pyruvate-to-acetate conversion (since their

expression of ACSS1 is low and thus they can scarcely metabolize it) (**Fig.3.6**), it is interesting to speculate on whether we could further increase acetate secretion by triggering oxidative stress in these cells, possibly by treating them with galactose or palmitate, which are known methods to increase ROS production (302). If this were possible, and we could effectively target acetate transport to block its export, we could drive cells to metabolize acetate through ACSS2 and force an increase in the synthesis of lipids. This in turn would deplete the cytosolic pool of NADPH and produce an imbalance of acetyl-CoA, which may be toxic for cancer cells. Under the same logic, cells expressing ACSS1 would instead be forced to metabolize acetate to drive OXPHOS, potentially increasing the production of ROS. Ultimately it may be possible to induce the generation of ROS in *in vivo* cancer models by low level irradiation and trap acetate inside cells by targeting transport. Additional treatment with an ACSS2 inhibitor would force all intracellular acetate to be metabolized by ACSS1, further increasing the production of ROS, and likely resulting in anti-tumor effects. In this way it may be possible to potentiate the effect of radiotherapy without excessive radiation exposure.

In relation to our analysis of transporter gene expression in all the cancer cell lines for which mRNA expression data is available in CCLE (**Fig.4.1**), it must be noted that the conclusions that we drew from transporter expression levels are valid in so far as we don't consider how the exposure to acetate or other environmental factors may influence them. Indeed, it has been reported that MCT1 expression can be upregulated by the presence of acetate in low glucose conditions (131), while MCT4 expression is upregulated in hypoxia (239). We did not test this, and this could be relevant for low MCT1 cell lines like BT-474. On the other hand, our exposure to acetate in metabolic net flux experiments was always in conditions of high acetate availability (except when we tested the effect of galactose), and exposure to acetate did not exceed the 24 hours of the experiment.

The results for net acetate consumption flux following inhibition of MCT1 and MCT4 (**Fig.4.3**) point to the fact that this type of experiment is of difficult interpretation when blocking lactate export in highly glycolytic cell lines leads to a metabolic rearrangement potentially affecting acetate consumption indirectly. It may be useful to find ways to allow cells to still

secrete lactate freely while blocking the two MCTs. One possibility may be overexpressing aquaporins with lactate permeability in the cancer cells tested (303), or otherwise sodium-coupled MCTs (SMCTs), which should not be targeted by the inhibitors (304).

Similarly, the influence of pH on acetate secretion (**Fig.4.4**) points at the involvement of proton symport, the mechanism of transport typical of MCTs, in acetate import, such that the higher concentration of extracellular protons drives acetate according to the proton gradient while impeding the secretion of lactate. Unfortunately, with this experimental set up it is not possible to gain additional information about which MCT would be involved, or if other proton coupled transporters could influence the result.

As for the results of our first CRISPR KO screen (**Fig.5.23**), it is important to note that we plan to repeat it with other cell lines, the human HEK-293 ACSS2-OE and murine B6TAg2.03, to understand whether our finding that MCT13 is involved in acetate-mediated cell proliferative advantage is cell type- and species-agnostic or if changing the cancer type will provide us with additional findings. On a technical note, it is also important to repeat the screen in a cell line whose genetic background does not already harbor a genetic deletion, like the D42 m*Acly* KO cell line. This is because synthetic lethality effects that were in place as the screen started with the gRNA library transduction, before the actual experimental conditions were introduced, have likely reduced our coverage of sequenced gRNAs. Indeed, for each condition we recovered reads for around 20,000 gRNA pairs, which even considering essential housekeeping genes that we expected to disappear from the population, is still lower than our predictions. Lastly, another notable characteristic of this genetic screening setup is that, by being reliant on metabolism of acetate in the cytosol by ACSS2, it did not allow us to identify mitochondrial acetate transporters.

In terms of future directions on MCT13's role in acetate import, a variety of approaches should be considered. Given that knockdown shows some effect on acetate consumption, stable KO cell lines should be developed and tested, also in combination with MCT1 and MCT4 inhibitors, to assess their residual acetate consumption capabilities. The galactose- and ACLYi-assays can also be used to assess whether MCT13 ablation reduces acetate's

ability to confer a proliferative advantage. Another approach would be to employ cell-free systems based on proteoliposomes to assess the affinity of MCT13 for acetate. A method for combining this and LC-MS metabolomics has recently been proposed (305). MCT13 should also be investigated on a structural level to better understand its similarities with MCT1. Since the mechanism of transport of lactate in MCT1 has been described (306), this knowledge combined with dynamic modeling would be a starting point to understand if acetate can be a substrate for transport by MCT13.

It is interesting to note that MCT13 is among one of the so-called neglected SLC transporters in terms of publications available (175). A query for "SLC16A13" on Google Scholar performed on October 2025 returns only a handful of papers in which SLC16A13 is the main topic (182,307–314), as well as one undergraduate thesis (315). Among these, two studies based on GWAS analyses point to an association between MCT13 and type 2 diabetes (312,313). Further, it has been shown that genetic deletion of SLC16A13 in mice leads to reduced hepatic lipid accumulation and consequently to an increase in hepatic insulin sensitivity compared to control when the animals are fed with a high fat diet (182). In the same study it was also confirmed that, while MCT13 had been previously assumed to be localized in the Golgi membrane, it can also be found on the plasma membrane. Several transport substrates have been proposed for MCT13, such as lactate (182) or oligopeptides (307), but direct evidence remains limited and the transporter is still classified as orphan (174). It is interesting to speculate over whether high MCT13 expression, rather than being directly causally linked to diabetes, may instead be responsible for facilitating the entry of acetate in hepatocytes to increase lipid biosynthesis, accelerate liver steatosis, and thus drive insulin resistance. Intriguingly, a study from 2004 also reported that inhibition of the $Na^+/H^+$ exchanger 1 (NHE1), which in conditions of low intracellular pH exchanges intracellular $H^+$ with extracellular $Na^+$, leads to downregulation of SLC16A13 expression in murine *in vivo* brain tissue and primary neuronal cells (314). It can be speculated that the inability to correctly regulate intracellular pH may lead to a downregulation of MCT13 in order to stop further intracellular acidification from the symport of $H^+$ and the transporter's substrate, be it acetate, lactate, or both. On this note, while it is reasonable to assume that

there is a degree of similarity in the mechanistic functions of MCT1 and MCT13, no information is available on whether MCT13 interacts with a chaperone protein and if it acts as a proton symporter, though our own data appears to suggest that acetate transport is influenced by changes in extracellular pH (**Fig.4.4**). Indeed, while amino acid sequence identity between human MCT1 and MCT13 is only 32.5%, the likelihood of structural alignment between the PDB structure 7CKR of MCT1 and the Alphafold 3 predicted structure of MCT13 is statistically significant (E-value = $9.47*10^{-20}$).

A number of limitations of this present study need to be mentioned. Firstly, the panel of cancer cell lines that we experimentally investigated for their ability to metabolize acetate (**Fig.3.4c**), while larger and more diverse in scope than many comparable studies, is still considerably small when compared to the 1020 cell lines in CCLE for which SLC expression data is available. As such, our statistical power when making inferences using our acetate consumption flux data remains limited. For example, our currently available data does not suggest any statistically significant correlation between acetate consumption flux measurements and any MCT expression data for the cell lines considered, which may be due to the fact that we possess flux data for only 26 cell lines present in CCLE at the moment. Moreover, it is important to note that our measurements of net metabolite consumption or secretion are not equivalent to measuring transport rate through the plasma membrane, as many transporters can function as both importers and exporters (209) and the net change of a metabolite in the medium may be limited by either transport or downstream catabolic reactions. These measurements, which can be conducted with heavy-labelled species over short periods of time between seconds and minutes will become particularly relevant when validating the magnitude of the contribution of MCT13 to acetate transport, in order to de-convolute the effect of the transporters from that of the downstream catabolism inside the cell. A number of additional validation experiments have not yet been conducted, including confirming the plasma membrane localization of MCT13 suggested in the literature, quantitatively determining the protein expression reduction achieved by shRNA knockdown (**Fig.5.23d**), producing and validating SLC16A13 KO cell lines, and testing if SLC16A13 ablation in the liver leads to changes in the concentration of circulating and hepatic acetate

in an *in vivo* setting. Lastly, it is necessary to remark that due to the redundant and substrate-promiscuous nature of SLC-mediated transport, the results of our study are strictly dependent on the context of the cell lines and cancer types that we chose to investigate, meaning that additional work will be required to fully elucidate the landscape of acetate import and export in different pathophysiological contexts.

# BIBLIOGRAPHY


1. Finley LWS. What is cancer metabolism? Cell. 2023 Apr;186(8):1670–88.

2. Hanahan D, Weinberg RA. Hallmarks of Cancer: The Next Generation. Cell. 2011 Mar;144(5):646–74.

3. Warburg O, Minami S. Versuche an Überlebendem Carcinom-gewebe. Klinische Wochenschrift. 1923 Apr 1;2(17):776–7.

4. Thompson CB, Vousden KH, Johnson RS, Koppenol WH, Sies H, Lu Z, et al. A century of the Warburg effect. Nat Metab. 2023 Nov 21;5(11):1840–3.

5. Warburg O. On the Origin of Cancer Cells. 1956;123.

6. Blanco A, Blanco G. Chapter 19 - Integration and Regulation of Metabolism. In: Blanco A, Blanco G, editors. Medical Biochemistry [Internet]. Academic Press; 2017. p. 425–45. Available from: https://www.sciencedirect.com/science/article/pii/B9780128035504000197

7. Warburg O. On Respiratory Impairment in Cancer Cells. Science. 1956 Aug 10;124(3215):269–70.

8. DeBerardinis RJ, Chandel NS. We need to talk about the Warburg effect. Nat Metab. 2020 Feb 3;2(2):127–9.

9. Pedersen PL. Tumor mitochondria and the bioenergetics of cancer cells. Progress in experimental tumor research Fortschritte der experimentellen Tumorforschung Progres de la recherche experimentale des tumeurs. 1978;22:190–274.

10. Moreno-Sánchez R, Rodríguez-Enríquez S, Marín-Hernández A, Saavedra E. Energy metabolism in tumor cells. The FEBS Journal. 2007 Mar;274(6):1393–418.

11. Bartman CR, Weilandt DR, Shen Y, Lee WD, Han Y, TeSlaa T, et al. Slow TCA flux and ATP production in primary solid tumours but not metastases. Nature. 2023 Feb 9;614(7947):349–57.

12. Wang Y, Stancliffe E, Fowle-Grider R, Wang R, Wang C, Schwaiger-Haber M, et al. Saturation of the mitochondrial NADH shuttles drives aerobic glycolysis in proliferating cells. Molecular Cell. 2022 Sep;82(17):3270-3283.e9.

13. Luengo A, Li Z, Gui DY, Sullivan LB, Zagorulya M, Do BT, et al. Increased demand for NAD+ relative to ATP drives aerobic glycolysis. Molecular Cell. 2021 Feb;81(4):691-707.e6.

14. Gatenby RA, Gillies RJ. Why do cancers have high aerobic glycolysis? Nat Rev Cancer. 2004 Nov 1;4(11):891–9.

15. Crabtree HG. Observations on the carbohydrate metabolism of tumours. Biochemical Journal. 1929 Jan 1;23(3):536–45.

16. Diaz-Ruiz R, Uribe-Carvajal S, Devin A, Rigoulet M. Tumor cell energy metabolism and its common features with yeast metabolism. Biochimica et Biophysica Acta (BBA) - Reviews on Cancer. 2009 Dec;1796(2):252–65.

17. Schlisio S. Neuronal apoptosis by prolyl hydroxylation: implication in nervous system tumours and the Warburg conundrum. J Cellular Molecular Medi. 2009 Oct;13(10):4104–12.

18. Tomiyama A, Serizawa S, Tachibana K, Sakurada K, Samejima H, Kuchino Y, et al. Critical Role for Mitochondrial Oxidative Phosphorylation in the Activation of Tumor Suppressors Bax and Bak. JNCI: Journal of the National Cancer Institute. 2006 Oct 18;98(20):1462–73.

19. Gogvadze V, Zhivotovsky B, Orrenius S. The Warburg effect and mitochondrial stability in cancer cells. Molecular Aspects of Medicine. 2010 Feb;31(1):60–74.

20. Xiao C, Tian H, Zheng Y, Yang Z, Li S, Fan T, et al. Glycolysis in tumor microenvironment as a target to improve cancer immunotherapy. Front Cell Dev Biol. 2022 Sep 19;10:1013885.

21. Busk M, Horsman MR, Kristjansen PEG, Van Der Kogel AJ, Bussink J, Overgaard J. Aerobic glycolysis in cancers: Implications for the usability of oxygen-responsive genes and fluorodeoxyglucose-PET as markers of tissue hypoxia. Intl Journal of Cancer. 2008 Jun 15;122(12):2726–34.

22. Ma EH, Verway MJ, Johnson RM, Roy DG, Steadman M, Hayes S, et al. Metabolic Profiling Using Stable Isotope Tracing Reveals Distinct Patterns of Glucose Utilization by Physiologically Activated CD8+ T Cells. Immunity. 2019 Nov;51(5):856-870.e5.

23. Ansó E, Weinberg SE, Diebold LP, Thompson BJ, Malinge S, Schumacker PT, et al. The mitochondrial respiratory chain is essential for haematopoietic stem cell function. Nat Cell Biol. 2017 Jun 1;19(6):614–25.

24. Sena LA, Li S, Jairaman A, Prakriya M, Ezponda T, Hildeman DA, et al. Mitochondria Are Required for Antigen-Specific T Cell Activation through Reactive Oxygen Species Signaling. Immunity. 2013 Feb;38(2):225–36.

25. Eagle H. THE SPECIFIC AMINO ACID REQUIREMENTS OF A HUMAN CARCINOMA CELL (STRAIN HELA) IN TISSUE CULTURE. Journal of Experimental Medicine. 1955 Jul 1;102(1):37–48.

26. Jain M, Nilsson R, Sharma S, Madhusudhan N, Kitami T, Souza AL, et al. Metabolite Profiling Identifies a Key Role for Glycine in Rapid Cancer Cell Proliferation. Science. 2012 May 25;336(6084):1040–4.

27. DeBerardinis RJ, Cheng T. Q's next: the diverse functions of glutamine in metabolism, cell biology and cancer. Oncogene. 2010 Jan 21;29(3):313–24.

28. Hosios AM, Hecht VC, Danai LV, Johnson MO, Rathmell JC, Steinhauser ML, et al. Amino Acids Rather than Glucose Account for the Majority of Cell Mass in Proliferating Mammalian Cells. Developmental Cell. 2016 Mar;36(5):540–9.

29. Altman BJ, Stine ZE, Dang CV. From Krebs to clinic: glutamine metabolism to cancer therapy. Nat Rev Cancer. 2016 Oct;16(10):619–34.

30. Weinberg F, Hamanaka R, Wheaton WW, Weinberg S, Joseph J, Lopez M, et al. Mitochondrial metabolism and ROS generation are essential for Kras-mediated tumorigenicity. Proc Natl Acad Sci USA. 2010 May 11;107(19):8788–93.

31. Yuneva M, Zamboni N, Oefner P, Sachidanandam R, Lazebnik Y. Deficiency in glutamine but not glucose induces MYC-dependent apoptosis in human cells. The Journal of Cell Biology. 2007 Jul 2;178(1):93–105.

32. Snell K, Natsumeda Y, Eble J, Glover J, Weber G. Enzymic imbalance in serine metabolism in human colon carcinoma and rat sarcoma. British Journal of Cancer. 1988 Jan 1;57(1):87–90.

33. Snell K. Enzymes of serine metabolism in normal, developing and neoplastic rat tissues. Advances in Enzyme Regulation. 1984 Jan;22:325–400.

34. Beroukhim R, Mermel CH, Porter D, Wei G, Raychaudhuri S, Donovan J, et al. The landscape of somatic copy-number alteration across human cancers. Nature. 2010 Feb;463(7283):899–905.

35. Possemato R, Marks KM, Shaul YD, Pacold ME, Kim D, Birsoy K, et al. Functional genomics reveal that the serine synthesis pathway is essential in breast cancer. Nature. 2011 Aug;476(7360):346–50.

36. Locasale JW, Grassian AR, Melman T, Lyssiotis CA, Mattaini KR, Bass AJ, et al. Phosphoglycerate dehydrogenase diverts glycolytic flux and contributes to oncogenesis. Nat Genet. 2011 Sep;43(9):869–74.

37. DeNicola GM, Chen PH, Mullarky E, Sudderth JA, Hu Z, Wu D, et al. NRF2 regulates serine biosynthesis in non–small cell lung cancer. Nat Genet. 2015 Dec;47(12):1475–81.

38. Snell K, Natsumeda Y, Weber G. The modulation of serine metabolism in hepatoma 3924A during different phases of cellular proliferation in culture. Biochemical Journal. 1987 Jul 15;245(2):609–12.

39. Fan J, Ye J, Kamphorst JJ, Shlomi T, Thompson CB, Rabinowitz JD. Quantitative flux analysis reveals folate-dependent NADPH production. Nature. 2014 Jun 12;510(7504):298–302.

40. Lewis CA, Parker SJ, Fiske BP, McCloskey D, Gui DY, Green CR, et al. Tracing Compartmentalized NADPH Metabolism in the Cytosol and Mitochondria of Mammalian Cells. Molecular Cell. 2014 Jul;55(2):253–63.

41. Ye J, Fan J, Venneti S, Wan YW, Pawel BR, Zhang J, et al. Serine Catabolism Regulates Mitochondrial Redox Control during Hypoxia. Cancer Discovery. 2014 Dec 3;4(12):1406–17.

42. Medes G, Thomas A, Weinhouse S. Metabolism of Neoplastic Tissue. IV. A Study of Lipid Synthesis in Neoplastic Tissue Slices in Vitro*. Cancer Research. 1953 Jan 1;13(1):27–9.

43. Ookhtens M, Kannan R, Lyon I, Baker N. Liver and adipose tissue contributions to newly formed fatty acids in an ascites tumor. American Journal of Physiology-Regulatory, Integrative and Comparative Physiology. 1984 Jul 1;247(1):R146–53.

44. Luengo A, Gui DY, Vander Heiden MG. Targeting Metabolism for Cancer Therapy. Cell Chemical Biology. 2017 Sep;24(9):1161–80.

45. Comerford SA, Huang Z, Du X, Wang Y, Cai L, Witkiewicz AK, et al. Acetate Dependence of Tumors. Cell. 2014 Dec 18;159(7):1591–602.

46. Gao M, Tashiro Y, Wang Q, Sakai K, Sonomoto K. High acetone–butanol–ethanol production in pH-stat co-feeding of acetate and glucose. Journal of Bioscience and Bioengineering. 2016 Aug 1;122(2):176–82.

47. Kamphorst JJ, Chung MK, Fan J, Rabinowitz JD. Quantitative analysis of acetyl-CoA production in hypoxic cancer cells reveals substantial contribution from acetate. Cancer Metab. 2014 Dec;2(1):23.

48. Mashimo T, Pichumani K, Vemireddy V, Hatanpaa KJ, Singh DK, Sirasanagandla S, et al. Acetate Is a Bioenergetic Substrate for Human Glioblastoma and Brain Metastases. Cell. 2014 Dec 18;159(7):1603–14.

49. Schug ZT, Peck B, Jones DT, Zhang Q, Grosskurth S, Alam IS, et al. Acetyl-CoA Synthetase 2 Promotes Acetate Utilization and Maintains Cancer Cell Growth under Metabolic Stress. Cancer Cell. 2015 Jan 12;27(1):57–71.

50. Wishart DS. Is Cancer a Genetic Disease or a Metabolic Disease? EBioMedicine. 2015 Jun;2(6):478–9.

51. Kontomanolis EN, Koutras A, Syllaios A, Schizas D, Mastoraki A, Garmpis N, et al. Role of Oncogenes and Tumor-suppressor Genes in Carcinogenesis: A Review. Anticancer Res. 2020 Nov;40(11):6009–15.

52. Dakal TC, Dhabhai B, Pant A, Moar K, Chaudhary K, Yadav V, et al. Oncogenes and tumor suppressor genes: functions and roles in cancers. MedComm. 2024 Jun;5(6):e582.

53. Shen L, Shi Q, Wang W. Double agents: genes with both oncogenic and tumor-suppressor functions. Oncogenesis. 2018 Mar 13;7(3):25.

54. Semenza GL. A return to cancer metabolism. J Mol Med. 2011 Mar;89(3):203–4.

55. Lanzetti L. Oncometabolites at the crossroads of genetic, epigenetic and ecological alterations in cancer. Cell Death Differ. 2024 Dec;31(12):1582–94.

56. Ward PS, Patel J, Wise DR, Abdel-Wahab O, Bennett BD, Coller HA, et al. The Common Feature of Leukemia-Associated IDH1 and IDH2 Mutations Is a Neomorphic Enzyme Activity Converting α-Ketoglutarate to 2-Hydroxyglutarate. Cancer Cell. 2010 Mar;17(3):225–34.

57. Dang L, White DW, Gross S, Bennett BD, Bittinger MA, Driggers EM, et al. Cancer-associated IDH1 mutations produce 2-hydroxyglutarate. Nature. 2009 Dec 10;462(7274):739–44.

58. Christensen BC, Smith AA, Zheng S, Koestler DC, Houseman EA, Marsit CJ, et al. DNA Methylation, Isocitrate Dehydrogenase Mutation, and Survival in Glioma. JNCI: Journal of the National Cancer Institute. 2011 Jan 19;103(2):143–53.

59. Noushmehr H, Weisenberger DJ, Diefes K, Phillips HS, Pujara K, Berman BP, et al. Identification of a CpG Island Methylator Phenotype that Defines a Distinct Subgroup of Glioma. Cancer Cell. 2010 May;17(5):510–22.

60. Unruh D, Zewde M, Buss A, Drumm MR, Tran AN, Scholtens DM, et al. Methylation and transcription patterns are distinct in IDH mutant gliomas compared to other IDH mutant cancers. Sci Rep. 2019 Jun 20;9(1):8946.

61. Ceccarelli M, Barthel FP, Malta TM, Sabedot TS, Salama SR, Murray BA, et al. Molecular Profiling Reveals Biologically Discrete Subsets and Pathways of Progression in Diffuse Glioma. Cell. 2016 Jan;164(3):550–63.

62. Lu C, Ward PS, Kapoor GS, Rohle D, Turcan S, Abdel-Wahab O, et al. IDH mutation impairs histone demethylation and results in a block to cell differentiation. Nature. 2012 Mar;483(7390):474–8.

63. Chowdhury R, Yeoh KK, Tian Y, Hillringhaus L, Bagg EA, Rose NR, et al. The oncometabolite 2-hydroxyglutarate inhibits histone lysine demethylases. EMBO Reports. 2011 May;12(5):463–9.

64. Turcan S, Makarov V, Taranda J, Wang Y, Fabius AWM, Wu W, et al. Mutant-IDH1-dependent chromatin state reprogramming, reversibility, and persistence. Nat Genet. 2018 Jan;50(1):62–72.

65. Turcan S, Rohle D, Goenka A, Walsh LA, Fang F, Yilmaz E, et al. IDH1 mutation is sufficient to establish the glioma hypermethylator phenotype. Nature. 2012 Mar;483(7390):479–83.

66. Kohli RM, Zhang Y. TET enzymes, TDG and the dynamics of DNA demethylation. Nature. 2013 Oct 24;502(7472):472–9.

67. Xu W, Yang H, Liu Y, Yang Y, Wang P, Kim SH, et al. Oncometabolite 2-Hydroxyglutarate Is a Competitive Inhibitor of α-Ketoglutarate-Dependent Dioxygenases. Cancer Cell. 2011 Jan;19(1):17–30.

68. Losman JA, Kaelin WG. What a difference a hydroxyl makes: mutant IDH, ( *R* )-2-hydroxyglutarate, and cancer. Genes Dev. 2013 Apr 15;27(8):836–52.

69. Frezza C, Pollard PJ, Gottlieb E. Inborn and acquired metabolic defects in cancer. J Mol Med. 2011 Mar;89(3):213–20.

70. Giallongo S, Costa F, Longhitano L, Giallongo C, Ferrigno J, Tropea E, et al. The Pleiotropic Effects of Fumarate: From Mitochondrial Respiration to Epigenetic Rewiring and DNA Repair Mechanisms. Metabolites. 2023 Jul 24;13(7):880.

71. Dalla Pozza E, Dando I, Pacchiana R, Liboi E, Scupoli MT, Donadelli M, et al. Regulation of succinate dehydrogenase and role of succinate in cancer. Seminars in Cell & Developmental Biology. 2020 Feb;98:4–14.

72. Selak MA, Armour SM, MacKenzie ED, Boulahbel H, Watson DG, Mansfield KD, et al. Succinate links TCA cycle dysfunction to oncogenesis by inhibiting HIF-α prolyl hydroxylase. Cancer Cell. 2005 Jan;7(1):77–85.

73. Stine ZE, Schug ZT, Salvino JM, Dang CV. Targeting cancer metabolism in the era of precision oncology. Nat Rev Drug Discov. 2022 Feb;21(2):141–62.

74. Farber Sidney, Diamond Louis K., Mercer Robert D., Sylvester Robert F., Wolff James A. Temporary Remissions in Acute Leukemia in Children Produced by Folic Acid

Antagonist, 4-Aminopteroyl-Glutamic Acid (Aminopterin). New England Journal of Medicine. 1948 Jun 3;238(23):787–93.

75. Walling J. From methotrexate to pemetrexed and beyond. A review of the pharmacodynamic and clinical properties of antifolates. Invest New Drugs. 2006 Jan;24(1):37–77.

76. Elion GB. The Purine Path to Chemotherapy. 244.

77. Wagner AD, Grothe W, Haerting J, Kleber G, Grothey A, Fleig WE. Chemotherapy in Advanced Gastric Cancer: A Systematic Review and Meta-Analysis Based on Aggregate Data. JCO. 2006 Jun 20;24(18):2903–9.

78. Heidelberger C, Chaudhuri NK, Danneberg P, Mooren D, Griesbach L, Duschinsky R, et al. Fluorinated Pyrimidines, A New Class of Tumour-Inhibitory Compounds. Nature. 1957 Mar;179(4561):663–6.

79. Parker WB. Enzymology of Purine and Pyrimidine Antimetabolites Used in the Treatment of Cancer. Chem Rev. 2009 Jul 8;109(7):2880–93.

80. Vander Heiden MG, DeBerardinis RJ. Understanding the Intersections between Metabolism and Cancer Biology. Cell. 2017 Feb;168(4):657–69.

81. Hsu PP, Sabatini DM. Cancer Cell Metabolism: Warburg and Beyond. Cell. 2008 Sep;134(5):703–7.

82. Lunt SY, Vander Heiden MG. Aerobic Glycolysis: Meeting the Metabolic Requirements of Cell Proliferation. Annu Rev Cell Dev Biol. 2011 Nov 10;27(1):441–64.

83. Pavlova NN, Thompson CB. The Emerging Hallmarks of Cancer Metabolism. Cell Metabolism. 2016 Jan;23(1):27–47.

84. Stein M, Lin H, Jeyamohan C, Dvorzhinski D, Gounder M, Bray K, et al. Targeting tumor metabolism with 2-deoxyglucose in patients with castrate-resistant prostate cancer and advanced malignancies. The Prostate. 2010 Sep 15;70(13):1388–94.

85. Raez LE, Papadopoulos K, Ricart AD, Chiorean EG, DiPaola RS, Stein MN, et al. A phase I dose-escalation trial of 2-deoxy-d-glucose alone or combined with docetaxel in patients with advanced solid tumors. Cancer Chemother Pharmacol. 2013 Feb;71(2):523–30.

86. Zhang D, Li J, Wang F, Hu J, Wang S, Sun Y. 2-Deoxy-D-glucose targeting of glucose metabolism in cancer cells as a potential therapy. Cancer Letters. 2014 Dec;355(2):176–83.

87. Wick AN, Drury DR, Nakada HI, Wolfe JB, Britton B, Grabowski R. LOCALIZATION OF THE PRIMARY METABOLIC BLOCK PRODUCED BY 2-DEOXYGLUCOSE. Journal of Biological Chemistry. 1957 Feb;224(2):963–9.

88. LANDAU BR, LASZLO J, STENGLE J, BURK D. Certain metabolic and pharmacologic effects in cancer patients given infusions of 2-deoxy-D-glucose. J Natl Cancer Inst. 1958 Sep;21(3):485–94.

89. Turcan S, Fabius AWM, Borodovsky A, Pedraza A, Brennan C, Huse J, et al. Efficient induction of differentiation and growth inhibition in IDH1 mutant glioma cells by the DNMT Inhibitor Decitabine. Oncotarget. 2013 Oct 31;4(10):1729–36.

90. Tateishi K, Wakimoto H, Iafrate AJ, Tanaka S, Loebel F, Lelic N, et al. Extreme Vulnerability of IDH1 Mutant Cancers to NAD+ Depletion. Cancer Cell. 2015 Dec;28(6):773–84.

91. DiNardo CD, Ravandi F, Agresta S, Konopleva M, Takahashi K, Kadia T, et al. Characteristics, clinical outcome, and prognostic significance of IDH mutations in AML. American J Hematol. 2015 Aug;90(8):732–6.

92. Quivoron C, David M, Straley K, Travins J, Kim H, Chen Y, et al. AG-221, an Oral, Selective, First-in-Class, Potent IDH2-R140Q Mutant Inhibitor, Induces Differentiation in a Xenotransplant Model. Blood. 2014 Dec 6;124(21):3735–3735.

93. Yen K, Travins J, Wang F, David MD, Artin E, Straley K, et al. AG-221, a First-in-Class Therapy Targeting Acute Myeloid Leukemia Harboring Oncogenic *IDH2* Mutations. Cancer Discovery. 2017 May 1;7(5):478–93.

94. Dang L, Yen K, Attar EC. IDH mutations in cancer and progress toward development of targeted therapeutics. Annals of Oncology. 2016 Apr;27(4):599–608.

95. Livingston RB, Venditti JM, Cooney DA, Carter SK. Glutamine Antagonists in Chemotherapy. In: Advances in Pharmacology [Internet]. Elsevier; 1971 [cited 2025 Oct 29]. p. 57–120. Available from: https://linkinghub.elsevier.com/retrieve/pii/S1054358908605943

96. O'Dwyer PJ, Alonso MT, Leyland-Jones B. Acivicin: a new glutamine antagonist in clinical trials. JCO. 1984 Sep;2(9):1064–71.

97. Halama A, Kulinski M, Dib SS, Zaghlool SB, Siveen KS, Iskandarani A, et al. Accelerated lipid catabolism and autophagy are cancer survival mechanisms under inhibited glutaminolysis. Cancer Letters. 2018 Aug;430:133–47.

98. Reis LMD, Adamoski D, Ornitz Oliveira Souza R, Rodrigues Ascenção CF, Sousa De Oliveira KR, Corrêa-da-Silva F, et al. Dual inhibition of glutaminase and carnitine palmitoyltransferase decreases growth and migration of glutaminase inhibition–

resistant triple-negative breast cancer cells. Journal of Biological Chemistry. 2019 Jun;294(24):9342–57.

99. Hennequart M, Labuschagne CF, Tajan M, Pilley SE, Cheung EC, Legrave NM, et al. The impact of physiological metabolite levels on serine uptake, synthesis and utilization in cancer cells. Nat Commun. 2021 Oct 26;12(1):6176.

100. Tajan M, Hennequart M, Cheung EC, Zani F, Hock AK, Legrave N, et al. Serine synthesis pathway inhibition cooperates with dietary serine and glycine limitation for cancer therapy. Nat Commun. 2021 Jan 14;12(1):366.

101. Tsegaye K, Tsehai BA, Getie B. Desirable L-asparaginases for treating cancer and current research trends. Front Microbiol. 2024 Mar 13;15:1269282.

102. Taylor SR, Falcone JN, Cantley LC, Goncalves MD. Developing dietary interventions as therapy for cancer. Nat Rev Cancer. 2022 Aug;22(8):452–66.

103. McCracken AN, Edinger AL. Nutrient transporters: the Achilles' heel of anabolism. Trends in Endocrinology & Metabolism. 2013 Apr;24(4):200–8.

104. Nuutinen H, Lindros K, Hekali P, Salaspuro M. Elevated blood acetate as indicator of fast ethanol elimination in chronic alcoholics. Alcohol. 1985 Aug;2(4):623–6.

105. Hosmer J, McEwan AG, Kappler U. Bacterial acetate metabolism and its influence on human epithelia. Emerg Top Life Sci. 2024 Feb 22;8(1):1–13.

106. Cheng Z, Meng Z, Tan D, Datsomor O, Zhan K, Lin M, et al. Effects of supplementation of sodium acetate on rumen fermentation and microbiota in postpartum dairy cows. Front Microbiol. 2022;13:1053503.

107. Salcido KN. Short Chain Fatty Acid Metabolism in Physiology and Disease [Internet]. [Philadelphia, USA]: University of Pennsylvania; 2025. Available from: https://repository.upenn.edu/handle/20.500.14332/61685

108. Schug ZT, Vande Voorde J, Gottlieb E. The metabolic fate of acetate in cancer. Nature Reviews Cancer. 2016 Nov 1;16(11):708–17.

109. Scheppach W, Pomare EW, Elia M, Cummings JH. The contribution of the large intestine to blood acetate in man. Clinical Science. 1991 Feb 1;80(2):177–82.

110. Suematsu N, Isohashi F. Molecular cloning and functional expression of human cytosolic acetyl-CoA hydrolase. Acta Biochim Pol. 2006;53(3):553–61.

111. Horibata Y, Ando H, Itoh M, Sugimoto H. Enzymatic and transcriptional regulation of the cytoplasmic acetyl-CoA hydrolase ACOT12. J Lipid Res. 2013 Aug;54(8):2049–59.

112. Maroni G, Cabrera San Millan E, Mercatelli R, Chiodi A, Campanella B, Onor M, et al. Reprogramming of Osimertinib-Resistant EGFR-mutant NSCLC: The Pyruvate-Acetaldehyde-Acetate Pathway As a Key Driver of Resistance. bioRxiv. 2025 Jan 1;2025.06.27.661913.

113. Liu X, Cooper DE, Cluntun AA, Warmoes MO, Zhao S, Reid MA, et al. Acetate Production from Glucose and Coupling to Mitochondrial Metabolism in Mammals. Cell. 2018 Oct;175(2):502-513.e13.

114. Cummings JH, Pomare EW, Branch WJ, Naylor CP, Macfarlane GT. Short chain fatty acids in human large intestine, portal, hepatic and venous blood. Gut. 1987 Oct;28(10):1221–7.

115. Rey FE, Faith JJ, Bain J, Muehlbauer MJ, Stevens RD, Newgard CB, et al. Dissecting the in vivo metabolic potential of two human gut acetogens. J Biol Chem. 2010 Jul 16;285(29):22082–90.

116. Schuchmann K, Müller V. Autotrophy at the thermodynamic limit of life: a model for energy conservation in acetogenic bacteria. Nat Rev Microbiol. 2014 Dec;12(12):809–21.

117. Nogal A, Valdes AM, Menni C. The role of short-chain fatty acids in the interplay between gut microbiota and diet in cardio-metabolic health. Gut Microbes. 2021 Dec;13(1):1–24.

118. Martino C, Zaramela LS, Gao B, Embree M, Tarasova J, Parker SJ, et al. Acetate reprograms gut microbiota during alcohol consumption. Nat Commun. 2022 Aug 8;13(1):4630.

119. Perry RJ, Peng L, Barry NA, Cline GW, Zhang D, Cardone RL, et al. Acetate mediates a microbiome–brain–β-cell axis to promote metabolic syndrome. Nature. 2016 Jun 1;534(7606):213–7.

120. MEDES G, FRIEDMANN B, WEINHOUSE S. Fatty acid metabolism. VIII. Acetate metabolism in vitro during hepatocarcinogenesis by p-dimethylaminoazobenzene. Cancer Res. 1956 Jan;16(1):57–62.

121. MEDES G, WEINHOUSE S. Metabolism of neoplastic tissue. XIII. Substrate competition in fatty acid oxidation in ascites tumor cells. Cancer Res. 1958 Apr;18(3):352–9.

122. MEDES G, PADEN G, WEINHOUSE S. Metabolism of neoplastic tissues. XI. Absorption and oxidation of dietary fatty acids by implanted tumors. Cancer Res. 1957 Feb;17(2):127–33.

123. Watkins PA, Maiguel D, Jia Z, Pevsner J. Evidence for 26 distinct acyl-coenzyme A synthetase genes in the human genome. J Lipid Res. 2007 Dec;48(12):2736–50.

124. Miller KD, Pniewski K, Perry CE, Papp SB, Shaffer JD, Velasco-Silva JN, et al. Targeting ACSS2 with a Transition-State Mimetic Inhibits Triple-Negative Breast Cancer Growth. Cancer Research. 2021 Mar 1;81(5):1252–64.

125. Guertin DA, Wellen KE. Acetyl-CoA metabolism in cancer. Nat Rev Cancer. 2023 Mar;23(3):156–72.

126. Salem N, Kuang Y, Corn D, Erokwu B, Kolthammer JA, Tian H, et al. [(Methyl)1-(11)c]-acetate metabolism in hepatocellular carcinoma. Mol Imaging Biol. 2011 Feb;13(1):140–51.

127. Miller KD, O'Connor S, Pniewski KA, Kannan T, Acosta R, Mirji G, et al. Acetate acts as a metabolic immunomodulator by bolstering T-cell effector function and potentiating antitumor immunity in breast cancer. Nat Cancer. 2023 Oct;4(10):1491–507.

128. Lakhter AJ, Hamilton J, Konger RL, Brustovetsky N, Broxmeyer HE, Naidu SR. Glucose-independent Acetate Metabolism Promotes Melanoma Cell Survival and Tumor Growth. J Biol Chem. 2016 Oct 14;291(42):21869–79.

129. Li X, Yu W, Qian X, Xia Y, Zheng Y, Lee JH, et al. Nucleus-Translocated ACSS2 Promotes Gene Transcription for Lysosomal Biogenesis and Autophagy. Mol Cell. 2017 Jun 1;66(5):684-697.e9.

130. Zhang S, He J, Jia Z, Yan Z, Yang J. Acetyl-CoA synthetase 2 enhances tumorigenesis and is indicative of a poor prognosis for patients with renal cell carcinoma. Urol Oncol. 2018 May;36(5):243.e9-243.e20.

131. Wang J, Yang Y, Shao F, Meng Y, Guo D, He J, et al. Acetate reprogrammes tumour metabolism and promotes PD-L1 expression and immune evasion by upregulating c-Myc. Nature Metabolism. 2024 May;6(5):914–32.

132. Li CJ, Chiu YH, Chang C, Chang YCI, Sheu JJC, Chiang AJ. Acetyl Coenzyme A Synthase 2 Acts as a Prognostic Biomarker Associated with Immune Infiltration in Cervical Squamous Cell Carcinoma. Cancers (Basel). 2021 Jun 22;13(13).

133. Zhou Z, Ren Y, Yang J, Liu M, Shi X, Luo W, et al. Acetyl-Coenzyme A Synthetase 2 Potentiates Macropinocytosis and Muscle Wasting Through Metabolic Reprogramming in Pancreatic Cancer. Gastroenterology. 2022 Nov;163(5):1281-1293.e1.

134. Yang J, Wang H, Li B, Liu J, Zhang X, Wang Y, et al. Inhibition of ACSS2 triggers glycolysis inhibition and nuclear translocation to activate SIRT1/ATG5/ATG2B

deacetylation axis, promoting autophagy and reducing malignancy and chemoresistance in ovarian cancer. Metabolism. 2025 Jan;162:156041.

135. Li Z, Liu H, He J, Wang Z, Yin Z, You G, et al. Acetyl-CoA Synthetase 2: A Critical Linkage in Obesity-Induced Tumorigenesis in Myeloma. Cell Metab. 2021 Jan 5;33(1):78-93.e7.

136. Qiu J, Villa M, Sanin DE, Buck MD, O'Sullivan D, Ching R, et al. Acetate Promotes T Cell Effector Function during Glucose Restriction. Cell Rep. 2019 May 14;27(7):2063-2074.e5.

137. Balmer ML, Ma EH, Bantug GR, Grählert J, Pfister S, Glatter T, et al. Memory CD8(+) T Cells Require Increased Concentrations of Acetate Induced by Stress for Optimal Function. Immunity. 2016 Jun 21;44(6):1312–24.

138. Balmer ML, Ma EH, Thompson AJ, Epple R, Unterstab G, Lötscher J, et al. Memory CD8(+) T Cells Balance Pro- and Anti-inflammatory Activity by Reprogramming Cellular Acetate Handling at Sites of Infection. Cell Metab. 2020 Sep 1;32(3):457-467.e5.

139. Shen L, Wang S, Gao C, Li Q, Feng S, Sun W, et al. Tumour-associated macrophages serve as an acetate reservoir to drive hepatocellular carcinoma metastasis. Nature Metabolism [Internet]. 2025 Oct 20; Available from: https://doi.org/10.1038/s42255-025-01393-9

140. Luong A, Hannah VC, Brown MS, Goldstein JL. Molecular characterization of human acetyl-CoA synthetase, an enzyme regulated by sterol regulatory element-binding proteins. J Biol Chem. 2000 Aug 25;275(34):26458–66.

141. Bacigalupa ZA, Arner EN, Vlach LM, Wolf MM, Brown WA, Krystofiak ES, et al. HIF-2α expression and metabolic signaling require ACSS2 in clear cell renal cell carcinoma. J Clin Invest. 2024 Jun 17;134(12).

142. Mews P, Donahue G, Drake AM, Luczak V, Abel T, Berger SL. Acetyl-CoA synthetase regulates histone acetylation and hippocampal memory. Nature. 2017 Jun 1;546(7658):381–6.

143. Huang Z, Zhang M, Plec AA, Estill SJ, Cai L, Repa JJ, et al. ACSS2 promotes systemic fat storage and utilization through selective regulation of genes involved in lipid metabolism. Proceedings of the National Academy of Sciences. 2018 Oct 2;115(40):E9499–506.

144. Ma S, Dahabieh MS, Mann TH, Zhao S, McDonald B, Song WS, et al. Nutrient-driven histone code determines exhausted CD8(+) T cell fates. Science. 2025 Feb 7;387(6734):eadj3020.

145. Wang S, Niu Z, Zhang Y, Liu R, Zhu R, Sun Y, et al. ACSS2 coupled with KAT7 regulates histone β-hydroxybutyrylation to enhance transcription. Science AdvAnceS. 2025;

146. Zhu R, Ye X, Lu X, Xiao L, Yuan M, Zhao H, et al. ACSS2 acts as a lactyl-CoA synthetase and couples KAT2A to function as a lactyltransferase for histone lactylation and tumor immune evasion. Cell Metabolism. 2025 Feb;37(2):361-376.e7.

147. De Leo A, Ugolini A, Yu X, Scirocchi F, Scocozza D, Peixoto B, et al. Glucose-driven histone lactylation promotes the immunosuppressive activity of monocyte-derived macrophages in glioblastoma. Immunity. 2024 May;57(5):1105-1123.e8.

148. Ugolini A, De Leo A, Yu X, Scirocchi F, Liu X, Peixoto B, et al. Functional Reprogramming of Neutrophils within the Brain Tumor Microenvironment by Hypoxia-Driven Histone Lactylation. Cancer Discovery. 2025 Jun 3;15(6):1270–96.

149. Fujino T, Kondo J, Ishikawa M, Morikawa K, Yamamoto TT. Acetyl-CoA synthetase 2, a mitochondrial matrix enzyme involved in the oxidation of acetate. J Biol Chem. 2001 Apr 6;276(14):11420–6.

150. Björnson E, Mukhopadhyay B, Asplund A, Pristovsek N, Cinar R, Romeo S, et al. Stratification of Hepatocellular Carcinoma Patients Based on Acetate Utilization. Cell Rep. 2015 Dec 1;13(9):2014–26.

151. Hlavaty SI, Salcido KN, Pniewski KA, Mukha D, Ma W, Kannan T, et al. ACSS1-dependent acetate utilization rewires mitochondrial metabolism to support AML and melanoma tumor growth and metastasis. Cell Reports. 2024 Dec;43(12):114988.

152. He Q, Ji L, Wang Y, Zhang Y, Wang H, Wang J, et al. Acetate enables metabolic fitness and cognitive performance during sleep disruption. Cell Metabolism. 2024 Sep 3;36(9):1998-2014.e15.

153. Khan A, Liu Y, Gad M, Kenny TC, Birsoy K. Solute carriers: The gatekeepers of metabolism. Cell. 2025 Feb;188(4):869–84.

154. Okada Y. Ion channels and transporters involved in cell volume regulation and sensor mechanisms. Cell Biochemistry and Biophysics. 2004 Oct 1;41(2):233–58.

155. Pizzagalli MD, Bensimon A, Superti-Furga G. A guide to plasma membrane solute carrier proteins. FEBS J. 2021 May;288(9):2784–835.

156. Kleinzeller A. Chapter 1 Charles Ernest Overton's Concept of a Cell Membrane. In: Deamer DW, Kleinzeller A, Fambrough DM, editors. Current Topics in Membranes [Internet]. Academic Press; 1999. p. 1–22. Available from: https://www.sciencedirect.com/science/article/pii/S0070216108610394

157. Stein W, Litman T. Channels, Carriers, and Pumps: An Introduction to Membrane Transport [Internet]. 2nd ed. Cambridge, MA: Academic Press; 2014. Available from: https://books.google.com/books?hl=en&lr=&id=TvaxAwAAQBAJ&oi=fnd&pg=PP1&ots=jSBZoeX7jV&sig=Gwu4vY9lUPvRscQS4jKspXLheFE#v=onepage&q&f=false

158. Yang NJ, Hinner MJ. Getting Across the Cell Membrane: An Overview for Small Molecules, Peptides, and Proteins. In: Gautier A, Hinner MJ, editors. Site-Specific Protein Labeling: Methods and Protocols [Internet]. New York, NY: Springer New York; 2015. p. 29–53. Available from: https://doi.org/10.1007/978-1-4939-2272-7_3

159. Liu X. ABC Family Transporters. In: Liu X, Pan G, editors. Drug Transporters in Drug Disposition, Effects and Toxicity [Internet]. Singapore: Springer Singapore; 2019. p. 13–100. Available from: https://doi.org/10.1007/978-981-13-7647-4_2

160. Robey RW, Pluchino KM, Hall MD, Fojo AT, Bates SE, Gottesman MM. Revisiting the role of ABC transporters in multidrug-resistant cancer. Nature Reviews Cancer. 2018 Jul 1;18(7):452–64.

161. Rose AE, Brown RSH, Schlieker C. Torsins: not your typical AAA+ ATPases. Crit Rev Biochem Mol Biol. 2015;50(6):532–49.

162. Stewart AG, Laming EM, Sobti M, Stock D. Rotary ATPases—dynamic molecular machines. Current Opinion in Structural Biology. 2014 Apr 1;25:40–8.

163. Palmgren MG, Nissen P. P-Type ATPases. Vol. 40, Annual Review of Biophysics. Annual Reviews; 2011. p. 243–66.

164. Roux B. Ion channels and ion selectivity. Lippard SJ, Berg JM, editors. Essays in Biochemistry. 2017 May 9;61(2):201–9.

165. Bates E. Ion Channels in Development and Cancer. Vol. 31, Annual Review of Cell and Developmental Biology. Annual Reviews; 2015. p. 231–47.

166. Höglund PJ, Nordström KJV, Schiöth HB, Fredriksson R. The solute carrier families have a remarkably long evolutionary history with the majority of the human families present before divergence of Bilaterian species. Mol Biol Evol. 2011 Apr;28(4):1531–41.

167. Colas C, Ung PMU, Schlessinger A. SLC transporters: structure, function, and drug discovery. Med Chem Commun. 2016;7(6):1069–81.

168. Forrest LR, Zhang YW, Jacobs MT, Gesmonde J, Xie L, Honig BH, et al. Mechanism for alternating access in neurotransmitter transporters. Proceedings of the National Academy of Sciences. 2008 Jul 29;105(30):10338–43.

169. Perland E, Fredriksson R. Classification Systems of Secondary Active Transporters. Trends in Pharmacological Sciences. 2017 Mar;38(3):305–15.

170. Povey S, Lovering R, Bruford E, Wright M, Lush M, Wain H. The HUGO Gene Nomenclature Committee (HGNC). Human Genetics. 2001 Dec 1;109(6):678–80.

171. Hediger MA, Clémençon B, Burrier RE, Bruford EA. The ABCs of membrane transporters in health and disease (SLC series): Introduction. Molecular Aspects of Medicine. 2013 Apr 1;34(2):95–107.

172. He L, Vasiliou K, Nebert DW. Analysis and update of the human solute carrier (SLC) gene superfamily. Human Genomics. 2009 Jan 1;3(2):195.

173. Ferrada E, Superti-Furga G. A structure and evolutionary-based classification of solute carriers. iScience. 2022 Oct 21;25(10):105096.

174. Goldmann U, Wiedmer T, Garofoli A, Sedlyarov V, Bichler M, Wolf G, et al. Data- and knowledge-derived functional landscape of human solute carriers. Mol Syst Biol. 2025 May 12;21(6):599–631.

175. César-Razquin A, Snijder B, Frappier-Brinton T, Isserlin R, Gyimesi G, Bai X, et al. A Call for Systematic Research on Solute Carriers. Cell. 2015 Jul 30;162(3):478–87.

176. Superti-Furga G, Lackner D, Wiedmer T, Ingles-Prieto A, Barbosa B, Girardi E, et al. The RESOLUTE consortium: unlocking SLC transporters for drug discovery. Nat Rev Drug Discov. 2020 Jul;19(7):429–30.

177. Hundal HS, Taylor PM. Amino acid transceptors: gate keepers of nutrient exchange and regulators of nutrient signaling. American Journal of Physiology-Endocrinology and Metabolism. 2009 Apr 1;296(4):E603–13.

178. Williams AJ, Harland L, Groth P, Pettifer S, Chichester C, Willighagen EL, et al. Open PHACTS: semantic interoperability for drug discovery. Drug Discov Today. 2012 Nov;17(21–22):1188–98.

179. Williams AL, Jacobs SBR, Moreno-Macías H, Huerta-Chagoya A, Churchhouse C, Márquez-Luna C, et al. Sequence variants in SLC16A11 are a common risk factor for type 2 diabetes in Mexico. Nature. 2014 Feb 6;506(7486):97–101.

180. Williams AL, Jacobs SBR, Moreno-Macías H, Huerta-Chagoya A, Churchhouse C, Márquez-Luna C, et al. Sequence variants in SLC16A11 are a common risk factor for type 2 diabetes in Mexico. Nature. 2014 Feb 1;506(7486):97–101.

181. Zhao Y, Feng Z, Zhang Y, Sun Y, Chen Y, Liu X, et al. Gain-of-Function Mutations of SLC16A11 Contribute to the Pathogenesis of Type 2 Diabetes. Cell Rep. 2019 Jan 22;26(4):884-892.e4.

182. Schumann T, König J, von Loeffelholz C, Vatner DF, Zhang D, Perry RJ, et al. Deletion of the diabetes candidate gene Slc16a13 in mice attenuates diet-induced ectopic lipid accumulation and insulin resistance. Communications Biology. 2021 Jul 1;4(1):826.

183. César-Razquin A, Girardi E, Yang M, Brehme M, Saez-Rodriguez J, Superti-Furga G. In silico Prioritization of Transporter–Drug Relationships From Drug Sensitivity Screens. Front Pharmacol. 2018 Sep 7;9:1011.

184. Nyquist MD, Prasad B, Mostaghel EA. Harnessing Solute Carrier Transporters for Precision Oncology. Molecules. 2017;22(4).

185. Sato H, Tamba M, Ishii T, Bannai S. Cloning and Expression of a Plasma Membrane Cystine/Glutamate Exchange Transporter Composed of Two Distinct Proteins *. Journal of Biological Chemistry. 1999 Apr 23;274(17):11455–8.

186. Lewerenz J, Hewett SJ, Huang Y, Lambros M, Gout PW, Kalivas PW, et al. The Cystine/Glutamate Antiporter System xc− in Health and Disease: From Molecular Mechanisms to Novel Therapeutic Opportunities. Antioxidants & Redox Signaling. 2013 Feb 10;18(5):522–55.

187. Yan Y, Teng H, Hang Q, Kondiparthi L, Lei G, Horbath A, et al. SLC7A11 expression level dictates differential responses to oxidative stress in cancer cells. Nature Communications. 2023 Jun 21;14(1):3673.

188. Schulte ML, Fu A, Zhao P, Li J, Geng L, Smith ST, et al. Pharmacological blockade of ASCT2-dependent glutamine transport leads to antitumor efficacy in preclinical models. Nat Med. 2018 Feb;24(2):194–202.

189. Jin J, Byun JK, Choi YK, Park KG. Targeting glutamine metabolism as a therapeutic strategy for cancer. Experimental & Molecular Medicine. 2023 Apr 1;55(4):706–15.

190. Conger KO, Chidley C, Ozgurses ME, Zhao H, Kim Y, Semina SE, et al. ASCT2 is a major contributor to serine uptake in cancer cells. Cell Reports. 2024 Aug 27;43(8):114552.

191. Jones R, Morris M. Monocarboxylate Transporters: Therapeutic Targets and Prognostic Factors in Disease. Clinical Pharmacology & Therapeutics. 2016 Nov 1;100(5):454–63.

192. Pérez-Escuredo J, Van Hée VF, Sboarina M, Falces J, Payen VL, Pellerin L, et al. Monocarboxylate transporters in the brain and in cancer. Biochimica et Biophysica Acta (BBA) - Molecular Cell Research. 2016 Oct 1;1863(10):2481–97.

193. Halestrap AP. The SLC16 gene family – Structure, role and regulation in health and disease. Molecular Aspects of Medicine. 2013 Apr 1;34(2):337–49.

194. Poole RC, Halestrap AP. Interaction of the Erythrocyte Lactate Transporter (Monocarboxylate Transporter 1) with an Integral 70-kDa Membrane Glycoprotein of the Immunoglobulin Superfamily *. Journal of Biological Chemistry. 1997 Jun 6;272(23):14624–8.

195. Muramatsu T. Basigin (CD147), a multifunctional transmembrane glycoprotein with various binding partners. The Journal of Biochemistry. 2016 May 1;159(5):481–90.

196. Wilson MC, Meredith D, Fox JEM, Manoharan C, Davies AJ, Halestrap AP. Basigin (CD147) Is the Target for Organomercurial Inhibition of Monocarboxylate Transporter Isoforms 1 and 4: THE ANCILLARY PROTEIN FOR THE INSENSITIVE MCT2 IS EMBIGIN (gp70) *. Journal of Biological Chemistry. 2005 Jul 22;280(29):27213–21.

197. Seka DJ, Schulz AK, Thaker TM, Tomasiak TM. The N-terminal signature motif on the transporter MCT1 is critical for CD147-mediated trafficking. Journal of Biological Chemistry. 2024 Jun;300(6):107333.

198. Marchiq I, Pouysségur J. Hypoxia, cancer metabolism and the therapeutic benefit of targeting lactate/H+ symporters. Journal of Molecular Medicine. 2016 Feb 1;94(2):155–71.

199. Park SJ, Smith CP, Wilbur RR, Cain CP, Kallu SR, Valasapalli S, et al. An overview of MCT1 and MCT4 in GBM: small molecule transporters with large implications. Am J Cancer Res. 2018;8(10):1967–76.

200. Marchiq I, Pouysségur J. Hypoxia, cancer metabolism and the therapeutic benefit of targeting lactate/H+ symporters. Journal of Molecular Medicine. 2016 Feb 1;94(2):155–71.

201. Affinito A, Quintavalle C, Chianese RV, Roscigno G, Fiore D, D'Argenio V, et al. MCT4-driven CAF-mediated metabolic reprogramming in breast cancer microenvironment is a vulnerability targetable by miR-425-5p. Cell Death Discovery. 2024 Mar 14;10(1):140.

202. Benny S, Mishra R, Manojkumar MK, Aneesh TP. From Warburg effect to Reverse Warburg effect; the new horizons of anti-cancer therapy. Medical Hypotheses. 2020 Nov 1;144:110216.

203. Dvorak V, Casiraghi A, Colas C, Koren A, Tomek T, Offensperger F, et al. Paralog-dependent isogenic cell assay cascade generates highly selective SLC16A3 inhibitors. Cell Chemical Biology. 2023 Aug 17;30(8):953-964.e9.

204. Goldberg FW, Kettle JG, Lamont GM, Buttar D, Ting AKT, McGuire TM, et al. Discovery of Clinical Candidate AZD0095, a Selective Inhibitor of Monocarboxylate Transporter 4 (MCT4) for Oncology. J Med Chem. 2023 Jan 12;66(1):384–97.

205. A Cancer Research UK Phase I Trial of AZD3965, a Monocarboxylate Transporter 1 Inhibitor (MCT1) in Patients With Advanced Cancer [Internet]. 2013 [cited 2013 Apr 23]. Available from: https://clinicaltrials.gov/study/NCT01791595

206. Cluntun AA, Visker JR, Velasco-Silva JN, Lang MJ, Cedeño-Rosario L, Shankar TS, et al. Direct mitochondrial import of lactate supports resilient carbohydrate oxidation. bioRxiv. 2024 Jan 1;2024.10.07.617073.

207. Kory N, Wyant GA, Prakash G, Uit De Bos J, Bottanelli F, Pacold ME, et al. SFXN1 is a mitochondrial serine transporter required for one-carbon metabolism. Science. 2018 Nov 16;362(6416):eaat9528.

208. Mathiowetz AJ, Meymand ES, Deol KK, Parlakgül G, Lange M, Pang SP, et al. CLCC1 promotes hepatic neutral lipid flux and nuclear pore complex assembly [Internet]. Cell Biology; 2024 [cited 2025 Oct 28]. Available from: http://biorxiv.org/lookup/doi/10.1101/2024.06.07.597858

209. Chidley C, Darnell AM, Gaudio BL, Lien EC, Barbeau AM, Vander Heiden MG, et al. A CRISPRi/a screening platform to study cellular nutrient transport in diverse microenvironments. Nat Cell Biol. 2024 May;26(5):825–38.

210. Wiedmer T, Teoh ST, Christodoulaki E, Wolf G, Tian C, Sedlyarov V, et al. Metabolic mapping of the human solute carrier superfamily [Internet]. Systems Biology; 2024 [cited 2025 Oct 28]. Available from: http://biorxiv.org/lookup/doi/10.1101/2024.09.23.614124

211. Middleton SJ, Markússon S, Åkerlund M, Deme JC, Tseng M, Li W, et al. SLC45A4 is a pain gene encoding a neuronal polyamine transporter. Nature. 2025 Oct 1;646(8084):404–12.

212. Shi X, Reinstadler B, Shah H, To TL, Byrne K, Summer L, et al. Combinatorial GxGxE CRISPR screen identifies SLC25A39 in mitochondrial glutathione transport linking iron homeostasis to OXPHOS. Nat Commun. 2022 May 5;13(1):2483.

213. Ri K, Weng TH, Claveras Cabezudo A, Jösting W, Zhang Y, Bazzone A, et al. Molecular mechanism of choline and ethanolamine transport in humans. Nature. 2024 Jun 1;630(8016):501–8.

214. Verkerke ARP, Shi X, Li M, Higuchi Y, Yamamuro T, Katoh D, et al. SLC25A48 controls mitochondrial choline import and metabolism. Cell Metabolism. 2024 Sep 3;36(9):2156-2166.e9.

215. Khan A, Unlu G, Lin P, Liu Y, Kilic E, Kenny TC, et al. Metabolic gene function discovery platform GeneMAP identifies SLC25A48 as necessary for mitochondrial choline import. Nature Genetics. 2024 Aug 1;56(8):1614–23.

216. Bisbach CM, Hass DT, Thomas ED, Cherry TJ, Hurley JB. Monocarboxylate Transporter 1 (MCT1) Mediates Succinate Export in the Retina. Invest Ophthalmol Vis Sci. 2022 Apr 1;63(4):1.

217. Luongo TS, Eller JM, Lu MJ, Niere M, Raith F, Perry C, et al. SLC25A51 is a mammalian mitochondrial NAD+ transporter. Nature. 2020 Dec 1;588(7836):174–9.

218. Liu S, Gad M, Li C, Cho K, Liu Y, Millet A, et al. SLC33A1 exports oxidized glutathione to maintain endoplasmic reticulum redox homeostasis. 2026 Feb 3;

219. Li L, You J, Chai ZQ, Li X, Cai X, Wang L, et al. SLC6A6 imports taurine into mitochondria to sustain mitochondrial translation and tumour growth. Nat Metab [Internet]. 2026 Feb 6 [cited 2026 Feb 12]; Available from: https://www.nature.com/articles/s42255-026-01455-6

220. Dias MM, King MS, Shokry E, Lilla S, Paul N, Thomason P, et al. SLC25A45 is required for mitochondrial uptake of methylated amino acids and de novo carnitine biosynthesis. Molecular Cell. 2025 Nov;85(21):4093-4104.e8.

221. Khan A, Yen FS, Unlu G, DelGaudio NL, Erdal R, Xiao M, et al. Machine-learning-guided discovery of SLC25A45 as a mediator of mitochondrial methylated amino acid import and carnitine synthesis. Cell Metabolism. 2025 Nov;37(11):2220-2232.e8.

222. Bose S, Ramesh V, Locasale JW. Acetate Metabolism in Physiology, Cancer, and Beyond. Trends Cell Biol. 2019 Sep;29(9):695–703.

223. Aschenbach JR, Bilk S, Tadesse G, Stumpff F, Gäbel G. Bicarbonate-dependent and bicarbonate-independent mechanisms contribute to nondiffusive uptake of acetate in the ruminal epithelium of sheep. Am J Physiol Gastrointest Liver Physiol. 2009;296:1098–107.

224. Fleming SE, Choi SY, Fitch MD. Absorption of short-chain fatty acids from the rat cecum in vivo. J Nutr. 1991 Nov;121(11):1787–97.

225. Ferro S, Azevedo-Silva J, Casal M, Côrte-Real M, Baltazar F, Preto A. Characterization of acetate transport in colorectal cancer cells and potential therapeutic implications. Oncotarget. 2016 Oct;7(43):70639–53.

226. Chu S, Montrose MH. Extracellular pH regulation in microdomains of colonic crypts: effects of short-chain fatty acids. Proc Natl Acad Sci U S A. 1995 Apr 11;92(8):3303–7.

227. Reynolds DA, Rajendran VM, Binder HJ. Bicarbonate-stimulated [14C]butyrate uptake in basolateral membrane vesicles of rat distal colon. Gastroenterology. 1993 Sep;105(3):725–32.

228. Babu E, Ramachandran S, Coothankandaswamy V, Elangovan S, Prasad PD, Ganapathy V, et al. Role of SLC5A8, a plasma membrane transporter and a tumor suppressor, in the antitumor activity of dichloroacetate. Oncogene. 2011 Sep;30(38):4026–37.

229. Coady MJ, Chang M, Charron FM, Plata C, Wallendorff B, Sah JF, et al. The human tumour suppressor gene SLC5A8 expresses a Na+ monocarboxylate cotransporter. The Journal of Physiology. 2004 Jun;557(3):719–31.

230. Miyauchi S, Gopal E, Fei YJ, Ganapathy V. Functional Identification of SLC5A8, a Tumor Suppressor Down-regulated in Colon Cancer, as a Na+-coupled Transporter for Short-chain Fatty Acids. Journal of Biological Chemistry. 2004 Apr;279(14):13293–6.

231. Moschen I, Bröer A, Galić S, Lang F, Bröer S. Significance of short chain fatty acid transport by members of the monocarboxylate transporter family (MCT). Neurochemical Research. 2012;37(11):2562–8.

232. Rae C, Fekete AD, Kashem MA, Nasrallah FA, Bröer S. Metabolism, compartmentation, transport and production of acetate in the cortical brain tissue slice. Neurochemical Research. 2012 Nov;37(11):2541–53.

233. Tamai I, Takanaga H, Ogihara T, Higashida H, Maeda H, Sai Y, et al. Participation of a Proton-Cotransporter, MCT1, in the Intestinal Transport of Monocarboxylic Acids. Biochemical and Biophysical Research Communications. 1995 Sep;214(2):482–9.

234. Park JY, Kim D, Yang M, Park HY, Lee SH, Rincon M, et al. Gene silencing of SLC5A8 identified by genome-wide methylation profiling in lung cancer. Lung Cancer. 2013 Mar 1;79(3):198–204.

235. Li M, Long X, Wan H, Yin M, Yang B, Zhang F, et al. Monocarboxylate transporter 1 promotes proliferation and invasion of renal cancer cells by mediating acetate transport. Cell Biology International. 2021 Jun;45(6):1278–87.

236. Jackson VN, Halestrap AP. The Kinetics, Substrate, and Inhibitor Specificity of the Monocarboxylate (Lactate) Transporter of Rat Liver Cells Determined Using the Fluorescent Intracellular pH Indicator, 2',7'-Bis(carboxyethyl)-5(6)-carboxyfluorescein. Journal of Biological Chemistry. 1996 Jan;271(2):861–8.

237. Jeon JY, Lee M, Whang SH, Kim JW, Cho A, Yun M. Regulation of acetate utilization by Monocarboxylate Transporter 1 (MCT1) in Hepatocellular Carcinoma (HCC). Oncology Research. 2018;26(1):71–81.

238. Kim D, Ko HY, Chung JI, Park YM, Lee S, Kim SY, et al. Visualizing cancer-originating acetate uptake through monocarboxylate transporter 1 in reactive astrocytes in the glioblastoma tumor microenvironment. Neuro-Oncology. 2024 May;26(5):843–57.

239. Ullah MS, Davies AJ, Halestrap AP. The plasma membrane lactate transporter MCT4, but not MCT1, is up-regulated by hypoxia through a HIF-1alpha-dependent mechanism. J Biol Chem. 2006 Apr 7;281(14):9030–7.

240. Cuff MA, Lambert DW, Shirazi-Beechey SP. Substrate-induced regulation of the human colonic monocarboxylate transporter, MCT1. The Journal of Physiology. 2002 Mar;539(2):361–71.

241. Illek B, Tam AWK, Fischer H, Machen TE. Anion selectivity of apical membrane conductance of Calu 3 human airway epithelium. Pfl□gers Archiv European Journal of Physiology. 1999 Apr;437(6):812–22.

242. Foltz M, Boll M, Raschka L, Kottra G, Daniel H. A novel bifunctionality: PAT1 and PAT2 mediate electrogenic proton/amino acid and electroneutral proton/fatty acid symport. The FASEB Journal. 2004 Nov;18(14):1758–60.

243. Hosios A, Li Z, Lien E, Vander Heiden M. Preparation of Lipid-Stripped Serum for the Study of Lipid Metabolism in Cell Culture. BIO-PROTOCOL [Internet]. 2018 [cited 2025 Oct 16];8(11). Available from: https://bio-protocol.org/e2876

244. Folch J, Lees M, Stanley GHS. A SIMPLE METHOD FOR THE ISOLATION AND PURIFICATION OF TOTAL LIPIDES FROM ANIMAL TISSUES. Journal of Biological Chemistry. 1957 May;226(1):497–509.

245. Lu W, McBride MJ, Lee WD, Xing X, Xu X, Li X, et al. Selected Ion Monitoring for Orbitrap-Based Metabolomics. Metabolites. 2024 Mar 25;14(4):184.

246. Perez De Souza L, Alseekh S, Scossa F, Fernie AR. Ultra-high-performance liquid chromatography high-resolution mass spectrometry variants for metabolomics research. Nat Methods. 2021 Jul;18(7):733–46.

247. Plumb RS, Gethings LA, Rainville PD, Isaac G, Trengove R, King AM, et al. Advances in high throughput LC/MS based metabolomics: A review. TrAC Trends in Analytical Chemistry. 2023 Mar;160:116954.

248. Sarvin B, Lagziel S, Sarvin N, Mukha D, Kumar P, Aizenshtein E, et al. Fast and sensitive flow-injection mass spectrometry metabolomics by analyzing sample-specific ion distributions. Nat Commun. 2020 Jun 24;11(1):3186.

249. Song HE, Lee HY, Kim SJ, Back SH, Yoo HJ. A Facile Profiling Method of Short Chain Fatty Acids Using Liquid Chromatography-Mass Spectrometry. Metabolites. 2019 Aug 28;9(9):173.

250. Van Eijk HMH, Bloemen JG, Dejong CHC. Application of liquid chromatography–mass spectrometry to measure short chain fatty acids in blood. Journal of Chromatography B. 2009 Mar;877(8–9):719–24.

251. Trivedi N, Erickson HE, Bala V, Chhonker YS, Murry DJ. A Concise Review of Liquid Chromatography-Mass Spectrometry-Based Quantification Methods for Short Chain Fatty Acids as Endogenous Biomarkers. IJMS. 2022 Nov 3;23(21):13486.

252. Zhao S, Li L. Chemical derivatization in LC-MS-based metabolomics study. TrAC Trends in Analytical Chemistry. 2020 Oct;131:115988.

253. Gertsman I, Barshop BA. Promises and pitfalls of untargeted metabolomics. J of Inher Metab Disea. 2018 May;41(3):355–66.

254. Alberts B, Johnson A, Lewis J. Molecular Biology of the Cell. 4th ed. New York: Garland Science; 2002.

255. Mukha D, Dessain J, O'Connor S, Pniewski K, Bertolazzi F, Patel J, et al. Identification of Fasnall as a therapeutically effective Complex I inhibitor [Internet]. bioRxiv; 2024 [cited 2025 Oct 25]. Available from: http://biorxiv.org/lookup/doi/10.1101/2024.05.03.592013

256. Cluntun AA, Badolia R, Lettlova S, Parnell KM, Shankar TS, Diakos NA, et al. The pyruvate-lactate axis modulates cardiac hypertrophy and heart failure. Cell Metabolism. 2021 Mar;33(3):629-648.e10.

257. Critchlow SE, Hopcroft L, Mooney L, Curtis N, Whalley N, Zhong H, et al. Abstract 3224: Pre-clinical targeting of the metabolic phenotype of lymphoma by AZD3965, a selective inhibitor of monocarboxylate transporter 1 (MCT1). Cancer Research. 2012 Apr 15;72(8_Supplement):3224–3224.

258. Heinrich T, Sala-Hojman A, Ferretti R, Petersson C, Minguzzi S, Gondela A, et al. Discovery of 5-{2-[5-Chloro-2-(5-ethoxyquinoline-8-sulfonamido)phenyl]ethynyl}-4-methoxypyridine-2-carboxylic Acid, a Highly Selective in Vivo Useable Chemical Probe to Dissect MCT4 Biology. J Med Chem. 2021 Aug 26;64(16):11904–33.

259. Ovens MJ, Davies AJ, Wilson MC, Murray CM, Halestrap AP. AR-C155858 is a potent inhibitor of monocarboxylate transporters MCT1 and MCT2 that binds to an intracellular site involving transmembrane helices 7–10. Biochemical Journal. 2010 Feb 1;425(3):523–30.

260. Quanz M, Bender E, Kopitz C, Grünewald S, Schlicker A, Schwede W, et al. Preclinical Efficacy of the Novel Monocarboxylate Transporter 1 Inhibitor BAY-8002 and Associated Markers of Resistance. Molecular Cancer Therapeutics. 2018 Nov 1;17(11):2285–96.

261. Jost M, Chen Y, Gilbert LA, Horlbeck MA, Krenning L, Menchon G, et al. Combined CRISPRi/a-Based Chemical Genetic Screens Reveal that Rigosertib Is a Microtubule-Destabilizing Agent. Molecular Cell. 2017 Oct;68(1):210-223.e6.

262. Kampmann M. CRISPRi and CRISPRa Screens in Mammalian Cells for Precision Biology and Medicine. ACS Chem Biol. 2018 Feb 16;13(2):406–16.

263. Palmer AC, Chidley C, Sorger PK. A curative combination cancer therapy achieves high fractional cell killing through low cross-resistance and drug additivity. eLife. 2019 Nov 19;8:e50036.

264. Tian R, Abarientos A, Hong J, Hashemi SH, Yan R, Dräger N, et al. Genome-wide CRISPRi/a screens in human neurons link lysosomal failure to ferroptosis. Nat Neurosci. 2021 Jul;24(7):1020–34.

265. Rebsamen M, Girardi E, Sedlyarov V, Scorzoni S, Papakostas K, Vollert M, et al. Gain-of-function genetic screens in human cells identify SLC transporters overcoming environmental nutrient restrictions. Life Sci Alliance. 2022 Nov;5(11):e202201404.

266. Wolf G, Leippe P, Onstein S, Goldmann U, Frommelt F, Teoh ST, et al. The genetic interaction map of the human solute carrier superfamily [Internet]. Systems Biology; 2024 [cited 2025 Oct 28]. Available from: http://biorxiv.org/lookup/doi/10.1101/2024.10.07.616442

267. Lavogina D, Lust H, Tahk MJ, Laasfeld T, Vellama H, Nasirova N, et al. Revisiting the Resazurin-Based Sensing of Cellular Viability: Widening the Application Horizon. Biosensors. 2022 Mar 25;12(4):196.

268. Vieira-da-Silva B, Castanho MARB. Resazurin Reduction-Based Assays Revisited: Guidelines for Accurate Reporting of Relative Differences on Metabolic Status. Molecules. 2023 Mar 1;28(5):2283.

269. Holden HM, Rayment I, Thoden JB. Structure and Function of Enzymes of the Leloir Pathway for Galactose Metabolism. Journal of Biological Chemistry. 2003 Nov;278(45):43885–8.

270. Mathupala SP, Griffin A, Hawkins AL, Pedersen PL. Glucose Catabolism in Cancer Cells: Amplification of the Gene Encoding Type II Hexokinase.

271. Wilson JE. Isozymes of mammalian hexokinase: structure, subcellular localization and metabolic function. Journal of Experimental Biology. 2003 Jun 15;206(12):2049–57.

272. Timson DJ, Reece RJ. Functional analysis of disease-causing mutations in human galactokinase. European Journal of Biochemistry. 2003 Apr;270(8):1767–74.

273. Jain IH, Calvo SE, Markhard AL, Skinner OS, To TL, Ast T, et al. Genetic Screen for Cell Fitness in High or Low Oxygen Highlights Mitochondrial and Lipid Metabolism. Cell. 2020 Apr;181(3):716-727.e11.

274. Gohil VM, Sheth SA, Nilsson R, Wojtovich AP, Lee JH, Perocchi F, et al. Nutrient-sensitized screening for drugs that shift energy metabolism from mitochondrial respiration to glycolysis. Nat Biotechnol. 2010 Mar;28(3):249–55.

275. Mallick R, Bhowmik P, Duttaroy AK. Targeting fatty acid uptake and metabolism in cancer cells: A promising strategy for cancer treatment. Biomedicine & Pharmacotherapy. 2023 Nov;167:115591.

276. Lee H, Woo SM, Jang H, Kang M, Kim SY. Cancer depends on fatty acids for ATP production: A possible link between cancer and obesity. Seminars in Cancer Biology. 2022 Nov;86:347–57.

277. Röhrig F, Schulze A. The multifaceted roles of fatty acid synthesis in cancer. Nat Rev Cancer. 2016 Nov;16(11):732–49.

278. Izzo LT, Trefely S, Demetriadou C, Drummond JM, Mizukami T, Kuprasertkul N, et al. Acetylcarnitine shuttling links mitochondrial metabolism to histone acetylation and lipogenesis. Sci Adv. 2023 May 5;9(18):eadf0115.

279. Bose S, Ramesh V, Locasale JW. Acetate Metabolism in Physiology, Cancer, and Beyond. Trends in Cell Biology. 2019 Sep;29(9):695–703.

280. Zhao S, Torres A, Henry RA, Trefely S, Wallace M, Lee JV, et al. ATP-Citrate Lyase Controls a Glucose-to-Acetate Metabolic Switch. Cell Reports. 2016 Oct;17(4):1037–52.

281. Zhao S, Jang C, Liu J, Uehara K, Gilbert M, Izzo L, et al. Dietary fructose feeds hepatic lipogenesis via microbiota-derived acetate. Nature. 2020 Mar 26;579(7800):586–91.

282. Yao T, Asayama Y. Animal-cell culture media: History, characteristics, and current issues. Reprod Medicine & Biology. 2017 Apr;16(2):99–117.

283. Newsom OJ, Zheng E, Sullivan LB. Defined media reveal the essential role of lipid scavenging in supporting cancer cell proliferation. Journal of Biological Chemistry. 2025 Oct;301(10):110693.

284. Else PL. The highly unnatural fatty acid profile of cells in culture. Progress in Lipid Research. 2020 Jan;77:101017.

285. Schultz K, Costa-Pinheiro P, Gardner L, Pinheiro LV, Ramirez-Solis J, Gardner SM, et al. Snapshots of acyl carrier protein shuttling in human fatty acid synthase. Nature. 2025 May 8;641(8062):520–8.

286. Wang P, Peng X, Hou T, Xu F, Zhou H, Yu Y, et al. Discovery and characterization of novel ATP citrate lyase inhibitors from natural products by a luminescence-based assay. Chemico-Biological Interactions. 2022 Nov;367:110199.

287. Liu P, Wang Y, Li X, Liu Z, Sun Y, Liu H, et al. Enhanced lipid biosynthesis in oral squamous cell carcinoma cancer-associated fibroblasts contributes to tumor progression: Role of IL8 / AKT / P-ACLY axis. Cancer Science. 2024 May;115(5):1433–45.

288. Altea-Manzano P, Doglioni G, Liu Y, Cuadros AM, Nolan E, Fernández-García J, et al. A palmitate-rich metastatic niche enables metastasis growth via p65 acetylation resulting in pro-metastatic NF-κB signaling. Nat Cancer. 2023 Feb 2;4(3):344–64.

289. Li JJ, Wang H, Tino JA, Robl JA, Herpin TF, Lawrence RM, et al. 2-Hydroxy-N-arylbenzenesulfonamides as ATP-citrate lyase inhibitors. Bioorganic & Medicinal Chemistry Letters. 2007 Jun;17(11):3208–11.

290. Carson MS, Rädler PD, Albright J, VerHague M, Rezeli ET, Roth D, et al. Development and Characterization of Syngeneic Orthotopic Transplant Models of Obesity-Responsive Triple-Negative Breast Cancer in C57BL/6J Mice. Cancers. 2024 Aug 9;16(16):2803.

291. Martino C, Zaramela LS, Gao B, Embree M, Tarasova J, Parker SJ, et al. Acetate reprograms gut microbiota during alcohol consumption. Nat Commun. 2022 Aug 8;13(1):4630.

292. Yamasaki E. THE SUCCESSIVE STAGES OF THE HYDROLYSIS OF TRIACETIN. J Am Chem Soc. 1920 Jul;42(7):1455–68.

293. Hernandez K, Garcia-Verdugo E, Porcar R, Fernandez-Lafuente R. Hydrolysis of triacetin catalyzed by immobilized lipases: Effect of the immobilization protocol and experimental conditions on diacetin yield. Enzyme and Microbial Technology. 2011 May;48(6–7):510–7.

294. Li Z, Ji BW, Dixit PD, Tchourine K, Lien EC, Hosios AM, et al. Cancer cells depend on environmental lipids for proliferation when electron acceptors are limited. Nat Metab. 2022 Jun 23;4(6):711–23.

295. Bock C, Datlinger P, Chardon F, Coelho MA, Dong MB, Lawson KA, et al. High-content CRISPR screening. Nature Reviews Methods Primers. 2022 Feb 10;2(1):8.

296. Olivieri M, Durocher D. Genome-scale chemogenomic CRISPR screens in human cells using the TKOv3 library. STAR Protocols. 2021 Mar;2(1):100321.

297. Tzelepis K, Koike-Yusa H, De Braekeleer E, Li Y, Metzakopian E, Dovey OM, et al. A CRISPR Dropout Screen Identifies Genetic Vulnerabilities and Therapeutic Targets in Acute Myeloid Leukemia. Cell Reports. 2016 Oct;17(4):1193–205.

298. Katsafadou AI, Nebert DW, Krupenko SA, Thompson DC, Vasiliou V. Update of the sideroflexin (SLC56) gene family. Hum Genomics. 2025 Jun 20;19(1):69.

299. Park SB, Uchida T, Tilson S, Hu Z, Ma CD, Leek M, et al. A dual conditional CRISPR-Cas9 system to activate gene editing and reduce off-target effects in human stem cells. Molecular Therapy - Nucleic Acids. 2022 Jun;28:656–69.

300. House R (Rae) J, Soper-Hopper MT, Vincent MP, Ellis AE, Capan CD, Madaj ZB, et al. A diverse proteome is present and enzymatically active in metabolite extracts. Nature Communications. 2024 Jul 10;15(1):5796.

301. Shestov AA, Liu X, Ser Z, Cluntun AA, Hung YP, Huang L, et al. Quantitative determinants of aerobic glycolysis identify flux through the enzyme GAPDH as a limiting step. eLife. 2014 Jul 9;3:e03342.

302. DiGiovanni LF, Khroud PK, Carmichael RE, Schrader TA, Gill SK, Germain K, et al. ROS transfer at peroxisome-mitochondria contact regulates mitochondrial redox. Science. 2025 Jul 10;389(6756):157–62.

303. Schmidt JDR, Walloch P, Höger B, Beitz E. Aquaporins with lactate/lactic acid permeability at physiological pH conditions. Biochimie. 2021 Sep 1;188:7–11.

304. Jha MK, Morrison BM. Lactate Transporters Mediate Glia-Neuron Metabolic Crosstalk in Homeostasis and Disease. Front Cell Neurosci. 2020 Sep 29;14:589582.

305. Kory N, Fitzpatrick F, Bhatnagar A, Aguirre H. Abstract 1550 TRANSIT – a new approach to identifying mitochondrial transporters. Journal of Biological Chemistry [Internet]. 2025 May 1 [cited 2025 Oct 30];301(5). Available from: https://doi.org/10.1016/j.jbc.2025.109477

306. Shi S, Li J chen, Zhou X yu, Li Z lu, Wang Y xin, Xu B hong, et al. Transport mechanism and drug discovery of human monocarboxylate transporter 1. Acta Pharmacologica Sinica. 2025 Aug 1;46(8):2323–33.

307. Higuchi K, Kunieda M, Sugiyama K, Tomabechi R, Kishimoto H, Inoue K. Monocarboxylate Transporter 13 (MCT13/SLC16A13) Functions as a Novel Plasma Membrane Oligopeptide Transporter. Nutrients. 2023;15(16).

308. Zeinolabedini A, Zarredar H, Zafari V, Soleimani Z, Sabbagh-Jadid H, Raeisi M. SLC16A13 Downregulation Contributes to Apoptosis Induction in A549 Lung Cancer Cell Line. Asian Pac J Cancer Prev. 2025 Feb 1;26(2):525–32.

309. Zheng H, Pu S, Zhang Y, Fan Y, Yang J. The Association between the rs312457 Genotype of the SLC16a13 Gene and Diabetes Mellitus in a Chinese Population. Computational and Mathematical Methods in Medicine. 2021 Jan 1;2021(1):9918055.

310. Sun F, He Y, Yang Z, Xu G, Wang R, Juan Z, et al. Propofol pretreatment inhibits ferroptosis and alleviates myocardial ischemia-reperfusion injury through the SLC16A13-AMPK-GPX4 pathway. Biomedicine & Pharmacotherapy. 2024 Oct 1;179:117345.

311. Zavarpour S, Zarredar H, Pedram N, Asvadi Kermani T, Soleimani Z, Hashemzadeh S, et al. Decreased SLC16A13 Expression Level Can Increase Apoptosis in KATO2 Cell Line, A Promising Biomarker. Asian Pac J Cancer Prev. 2024 Jun 1;25(6):1953–8.

312. Hara K, Fujita H, Johnson TA, Yamauchi T, Yasuda K, Horikoshi M, et al. Genome-wide association study identifies three novel loci for type 2 diabetes. Human Molecular Genetics. 2014 Jan 1;23(1):239–46.

313. The SIGMA Type 2 Diabetes Consortium. Sequence variants in SLC16A11 are a common risk factor for type 2 diabetes in Mexico. Nature. 2014 Feb;506(7486):97–101.

314. Zhou D, Xue J, Gavrialov O, Haddad GG. $Na^+$ /$H^+$ exchanger 1 deficiency alters gene expression in mouse brain. Physiological Genomics. 2004 Aug 11;18(3):331–9.

315. Ålund J. Functional characterization of central transport mechanisms by novel genes [Internet]. Uppsala University; 2012. Available from: https://www.diva-portal.org/smash/get/diva2:641530/FULLTEXT01.pdf